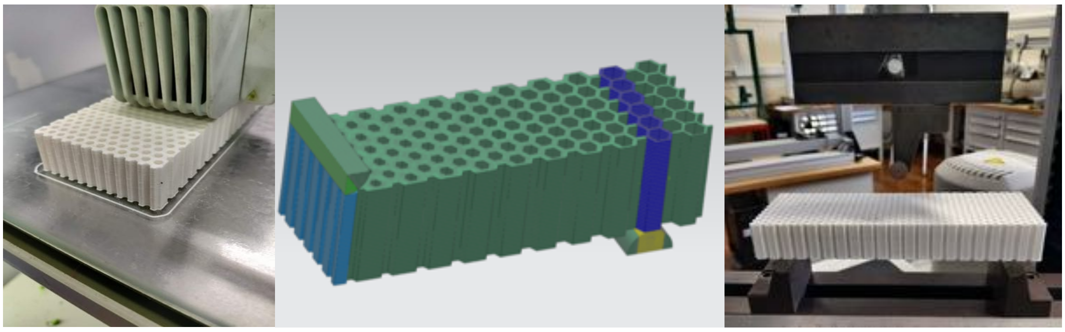

Cellular structures for use in composite panels with a mass distribution gradient produced by additive manufacturing

Bernardo Garrido Marques da Silva

Thesis to obtain the Master of Science Degree in

Mechanical Engineering

Supervisors: Prof. Maria de Fátima Reis Vaz
Prof. Augusto Manuel Moura Moita de Deus

Examination Committee

Chairman: Prof. Luís Filipe Galrão dos Reis
Supervisor: Prof. Maria de Fátima Reis Vaz
Member of the Committee: Prof. Alexandre José da Costa Velhinho

January 2021

To my family and friends.

Acknowledgements

Firstly, I would like to thank my mentors, Professor Maria Fátima Vaz and Professor Augusto Moita de Deus, for their kindness and availability, and for all the advice and knowledge throughout this project. They have certainly made me a better person, and I will keep and remember their teachings both on my personal and professional paths.

I will also wish to thank: Frederico Alves for tirelessly helping me with all sorts of problems in finite element analysis, as well as for the long hours of clarifying doubts.

Eng. Manuel Sardinha and Nuno Frutuoso for helping me produce the specimens in the laboratory Lab2Prod and for teaching me more about additive manufacturing.

Professor Etienne Copin from IMT Mines Albi, for his availability to manufacture the specimens in aluminum through SLM.

My friend since childhood, Joaquim Borba, and my friends since college, Miguel Simões, Bruno Abrantes, João Arrais, Henrique Pereira and Diogo Mendes, who have helped me grow as a person and who will certainly remain with me in the future.

And finally, I thank my family, especially my parents, my siblings and my grandparents who have always accompanied me, for all the support, presence, and all the advice they have given me to overcome the obstacles I have encountered along the way.

Resumo

O presente trabalho tem como objetivo avaliar as propriedades à flexão de materiais celulares com gradiente funcional (FGCM) e compará-los com estruturas honeycomb homogéneas mais tradicionais.

Para esse efeito, foram analisadas três configurações celulares, nomeadamente Hexagonal, Lotus e Plateau, como inicialmente proposto por Ronan et al. [1]. Foram também estudadas estruturas celulares com diferentes gradientes de densidade (parâmetro G). O efeito do ângulo de rotação foi também avaliado. Os materiais utilizados para as estruturas foram PLA (Ácido Poliláctico) e uma liga de alumínio. As estruturas foram concebidas em software CAD Solidworks e foram fabricadas por FFF (Fused Filament Fabrication). As propriedades de flexão dos FGCM foram analisadas através da realização de testes de flexão de três pontos, tanto experimentalmente como recorrendo a análise FEA (Análise de Elementos Finitos).

Os resultados mostram que as estruturas FGCM têm um melhor desempenho do que as estruturas honeycomb tradicionais, tanto em resistência como em rigidez. As estruturas Lotus tiveram melhor desempenho do que as estruturas honeycomb tradicionais para geometrias com rotação de 0 graus, enquanto que as estruturas Plateau mostram um melhor desempenho com uma rotação de 90 graus da geometria. Foi também demonstrado que quanto maior for o valor do parâmetro G, melhor será o desempenho mecânico das estruturas, tanto em rigidez inicial como em energia absorvida.

Consequentemente, as estruturas FGCM demonstraram ser uma alternativa às tradicionais estruturas honeycomb utilizadas nos painéis compósitos em sanduíche numa gama variada de aplicações, onde o baixo peso e a elevada rigidez das estruturas são prioritários.

Palavras-chave: FGCM, Parâmetro G, FEA, FFF, SLM, Ensaio de flexão em 3 pontos

Abstract

The present work aims to evaluate the flexural properties of functionally graded cellular materials (FGCM) and compare them to more traditional homogeneous honeycomb structures, used as sandwich panels.

For that purpose, three cellular configurations were analyzed, namely Hexagonal, Lotus and Hexagonal with Plateau borders, as initially proposed by Ronan et al. [1]. Graded structures with different density gradients (G parameter) were also studied. The effect of the angle of rotation was also evaluated. The materials used for the structures were PLA (Polylactic Acid) and an aluminum alloy. The structures were designed using CAD software Solidworks and were manufactured by FFF (Fused Filament Fabrication). The flexural properties of the FGCM were analyzed by performing three-point bending tests, both experimentally and also by means of FEA (Finite Element Analysis).

Results show that FGCM structures perform better than regular honeycomb structures, both in strength and stiffness. Lotus structures performed better than regular honeycomb structures for 0-degree rotation geometries, whereas Plateau structures show a better performance with a 90-degree rotation of the geometry. It was also shown that the higher the G-parameter value, the better the mechanical performance of the structures is, both in initial stiffness and absorbed energy.

Consequently, FGCM structures have shown to be an alternative to the traditional honeycomb structures used in sandwich composite panels in a varied range of applications, where low weight and high stiffness of structures are requirements.

Key-words: FGCM, G parameter, FEA, FFF, SLM, Three-point bending test

Table of contents

List of tables

List of figures

Nomenclature

L	Length until mid-section of the specimen.
$\mathbf{L_1}$	Length of the specimen.
$\mathbf{L_2}$	Support span length.
P	Applied Load.
H	Height of the specimen.
W	Width of the specimen.
$\mathbf{M_s}$	Volume mass.
$\mathbf{M_t}$	Total mass.
l	Core design length.
x	Distance between core design end and beginning of the specimen.
d	Core design wall thickness.
$\bar{\rho}$	Relative density.
ρ^*	Density of the cellular material.
ρ_s	Density of the solid that forms the walls.
σ	Stress.
$\mathbf{E_a}$	Absorbed energy.
E	Young’s Modulus.
G	G parameter.
K	Initial Stiffness.

Glossary

2D	Two-Dimensional.
3D	Three-Dimensional.
3PB	Three-Point Bending Test.
ABS	Acrylonitrile Butadiene Styrene.
AM	Additive Manufacturing.
ASTM	American Society for Testing and Materials.
CAD	Computer-Aided Design.
FDM	Fused Deposition Modelling.
FEA	Finite Element Analysis.
FEM	Finite Element Method.
FFF	Fused Filament Fabrication.
FGCM	Functionally Graded Cellular Material.
FGCS	Functionally Graded Cellular Structure.
HOBE	Honeycomb Before Expanded.
Lab2Prod	Product Development Laboratory at IST-UL.
PEEK	Polyether Ether Ketone.
PEI	Polyethylenimine.
PETG	Polyethylene Terephthalate Glycol.
PLA	Poly-lactic Acid.
SLM	Selective Laser Melting.
STL	Stereolithography.
TPU	Thermoplastic Polyurethane.

Chapter 1
Introduction

The main goal of this work is to study the mechanical properties of functionally graded cellular materials with different designs – Hexagonal, Plateau and Lotus – and for two different orientations. The aim is to search for arrangements with better mechanical properties, maintaining the lightness and strength which are characteristic of honeycomb structures, to be used as core of sandwich panels.

1.1 Motivation

In some industries where the weight of the components is a key aspect, as well as the mechanical properties associated with lightness, such as aerospace, automotive and marine, the continuous pursuit of this goal leads to new structures of the core of sandwich panels.

For many years, this pursuit was limited by technological manufacturing processes. With the introduction of Additive Manufacturing (AM), this limitation became less and less an obstacle. Because of that, new structures with much more complex designs could be developed. This development, has opened the way to the possibility of studying new and more complex structures, by being able to manufacture and experimentally test them, while at same time comparing such results with finite elements analysis (FEA).

One possibility of the functionally graded cellular structures is to have a density gradient, allowing, for example, structures with better bending stiffness while being lighter than similarly stiff honeycomb structures.

1.2 Objectives

The present thesis objective is to design, produce and analyze the stiffness, strength and energy absorption, using 3-point bending tests, of different functionally graded cellular materials, with different core designs (geometry and rotation), both experimentally and by finite element analysis (FEA). In total, twenty-three different arrangements were developed using Computer Aided Design (CAD) and Finite Element Analysis (FEA). As a comparison, regular honeycomb structures will also be used.

Since density gradient is one of the features of this study, a comparison parameter had to be used to specify each case. In total, five gradients were considered. Also, two orientations were evaluated.

The procedures to accomplish this study were the following:

1. Design the structures using CAD software;

2. Create the simulations on FEA software;
3. Produce the structures using a FFF process in a commercial 3D printing machine;
4. Experimentally test 5 structures, subjecting them to 3PB test;
5. Compare the FEA results with the experimental data.

1.3 Thesis Outline

The document is divided in five chapters.. Apart from this first chapter, in which a short description of the contents is given, the outline is:

- chapter 2: State of the Art;
- chapter 3: Experimental Method;
- chapter 4: Results and Discussion;
- chapter 5: Conclusions.

Chapter 2

State of the Art

In this chapter, it will be explained what functionally graded cellular materials (FGCM) are, since this work is based on these structures, it's applications and the categories it can be insert. Some considerations will be made about composite materials as well, as FGCM will be used as the core of sandwich structures (Figure 2.1 and Figure 2.2).

The production of these structures will be explained, namely some types of additive manufacturing and the advantages of this process.

The information below will be based on reviewed literature on previous studies about FGCM.

2.1 Composite materials

A composite material can be defined as a combination of two or more materials that results in better properties than those of the individual components used by themselves. Two well-known composite materials are the carbon fiber and glass fiber reinforced polymers [2]. The two constituents are the reinforcement and the matrix.

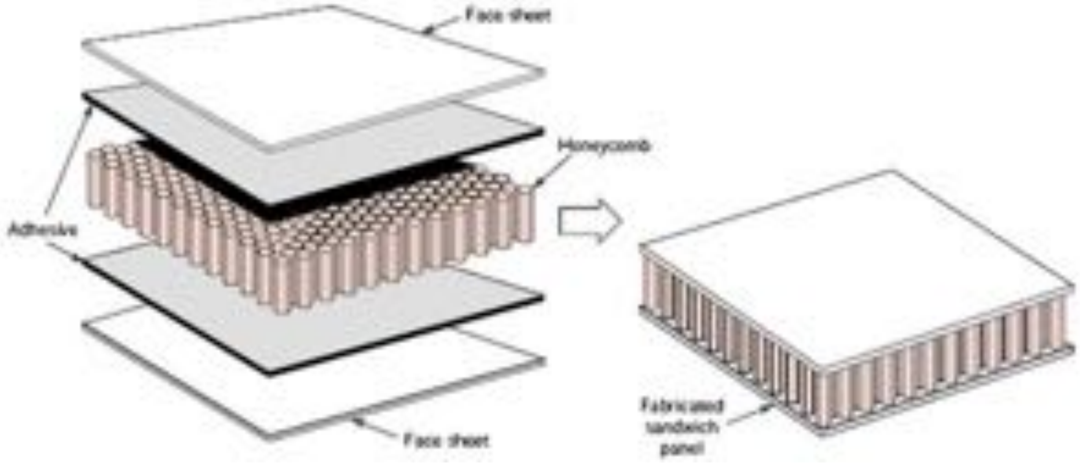

Figure 2.1 - Components of a sandwich structure [3].

The main advantages of composite materials are their high strength and stiffness combined with low density, when compared with bulk materials, allowing for a weight reduction in the finished part [2].

The reinforcing phase provides the strength and stiffness. In most cases, the reinforcement is harder, stronger, and stiffer than the matrix. The reinforcement is usually a fiber or a particulate.

A particular case of composite materials are the sandwich panels, which consist of two skin faces separated by thicker core (Figure 2.2 and 2.3). The skins protect the core. The core contributes to increase the flexural stiffness and to reduce the stress in the panel. Cores may consist of two-dimensional or three-dimensional cellular material, respectively designated by honeycomb or foam [4].

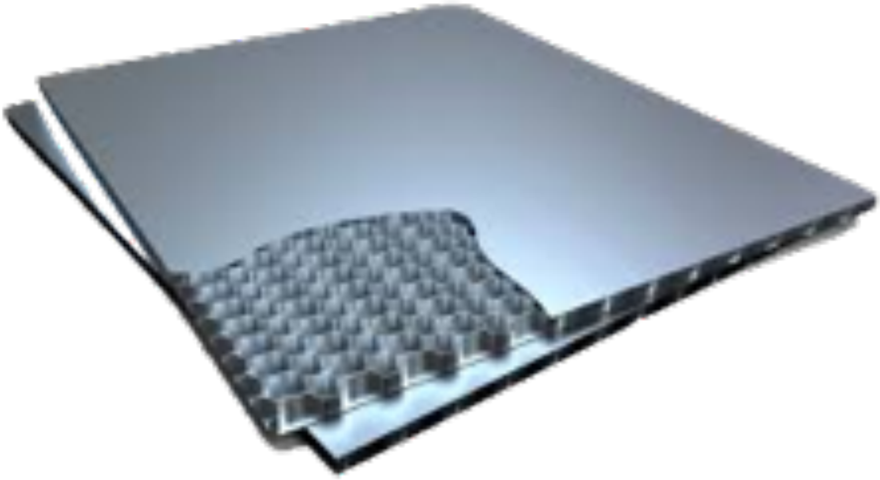

Figure 2.2 - Honeycomb sandwich structure [5].

Composite cellular panels have great potential in the fields of transportation, automotive and aerospace industries, among others [6]. The face materials can be fiber reinforced composites, while the core can be metal, polymer or wood [7].

2.2 Functionally graded cellular materials

In recent years, some new types of structures have been studied in pursuit of better structural elements. One of the major goals of structural design is to achieve load-carrying structures as light as possible, with high stiffness and strength.

Functionally graded cellular materials (FGCM) are materials in which its characteristics spatially change with composition and structure. FGCM are a blend of functionally graded materials with cellular materials [8]. They are an emerging class of advanced materials, extremely attractive for an extensive range of engineering applications because they enable the design of different functional performances within a part. These materials have captured the interest of the scientific community, resulting in ample research and technology applications [9].

Cellular materials, such as open or closed foams, honeycombs (Figure 2.1), and metal hollow spheres, are a new class of ultra-light multi-functional materials that can withstand large deformation at a nearly constant plateau stress. These materials can absorb a large amount of energy before collapsing. They are attached as sacrificial layers to protect structures, machines, and infrastructures against dynamic events. The core is expected to sustain damage during impact or blast loading, thereby mitigating the extent of destruction of the main structures. The properties of cellular materials enable energy dispersion, transmitting the impulse into the structure and consequently protecting objects located behind them [10].

The gradient can be made by several methods. It can occur by changing the distribution of the cell size, the thickness of the cell walls, the density or even the properties of the material along a certain direction [4].

Some literature has reported that many improved properties were imparted by graded cellular structures which could not have been achieved by uniform cellular structures (Figure 2.3) [11]. An example of a FGCM is given in Figure 2.4, which was obtained by Zhang et al. [12].

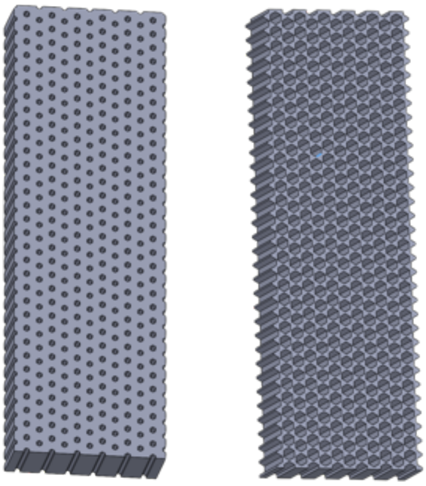

Figure 2.3 - Regular honeycomb structures without density gradient.

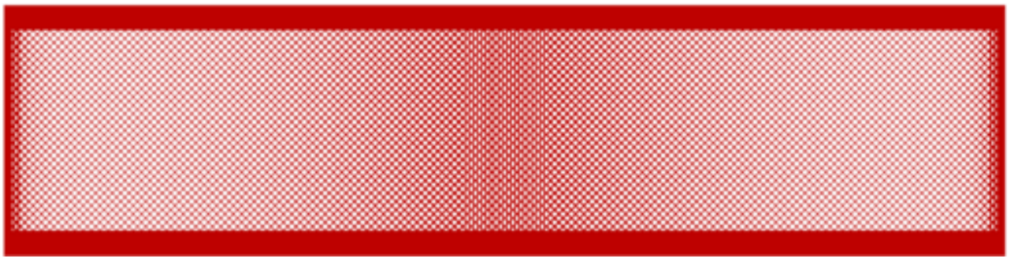

Figure 2.4 - Example of a FGCM obtained by Zhang [12]

These structures have a wide range of application in the aerospace and automotive industries that require low weight, high bending strength, and high energy absorption and low heat absorption [4].

In recent years, there has been an increase in the number of studies on cellular materials and also on functionally graded cellular materials. Designing, optimizing and testing the new structures are the main goal of the aforementioned papers.

FGCM are a recent kind of structures, that were limited until recent times due to technological manufacturing limitations. FGCM are a mixture of functionally graded materials and cellular materials [13].

Some studies, such as the one conducted by *Brothers* et al. [14] prove that for a foam with density gradient, the *Plateau* region in the Load vs Displacement curve grows smoothly instead of being constant as in the case of homogeneous foam.

Ajdari et al. [15] performed a study on 2D graded cellular structures and concluded that structures with steeper density gradient have better Young's modulus and yield stress than the uniform structures. *Zeng et al.* [16], on the other hand, concluded that density gradient structures have a positive effect on absorption capacity at low impact speeds. Sandwich beam tests with aluminum graded cores could also reduce weight while maintaining and respecting project specifications.

Li et al. [17] *and Jin* et al. [18] concluded that graded cellular materials had a greater capacity to absorb more energy in the non-linear region of the Load vs Displacement curve (plastic region) than the equivalent homogeneous cellular materials. This was more evident when comparing the results with those obtained with a smoother gradient.

Lijun et al. [19] concluded that functionally graded Ti-6Al-4V lattice structures had high strength under static and dynamic loading and the mechanical characteristics as well as the energy absorption capacity of porous materials increased with the introduction of the gradient concept. As far as the manufacture of this type of structures is concerned, additive manufacturing has gained particular relevance in recent times, since this type of manufacture has several advantages over more conventional processes. These advantages are covered in section 2.4.

S. Limmahakhun et al. [20] evaluated the stiffness and strength of cobalt chromium graded cellular structures for stress-shielding reduction. According to the study four types of graded cellular structures, based on graded orientations along radial and longitudinal planes, were manufactured using selective laser melting techniques. It was observed by performing mechanical tests that when the density gradient is along the radial plane (and not along the longitudinal plane) there is a significant improvement in yield and maximum stresses. Also, according to the same study, after normalizing the parameters, it was concluded that the functional structures were within the limits, based on the lower and upper limits of the results obtained for cellular materials with different structures and consequently different densities. Authors concluded that the graded materials do not significantly increase the mechanical properties, both stiffness and absorbed energy, when compared to cellular materials in the longitudinal plane. However, if the density gradient is designed according to the radial plane and not the longitudinal plane, it is possible to improve the mechanical resistance. In this specific case, the material with axial gradient proved to be the one with the most balanced mechanical characteristics. This makes it the most suitable for applications such as femoral prosthesis.

Another study by Mirzaali et al [21] was conducted comparing step gradient materials (5,10 and 15 steps) with continuous gradient materials (linear distribution). Authors concluded that the mechanical characteristics of materials with linear gradients are better than those with non-linear step gradients, which are due ro reduction in stress concentrations due to abrupt property changes. Some variations can cause the mechanical characteristics to change, such as, gradient having a linear variation or not, size of the functional unit, among others. The stress distribution was smoother in cases where the gradient was linear when compared to the other cases. When comparing the cases where the gradient is linear with the control FGM, those with linear gradient despite having higher Young's modulus and yield stress, have a lower elongation. It was also concluded that the mechanical characteristics vary greatly with the number of steps that the material presents.

M. Liang et al. [10], made a theoretical and numerical investigation of blast responses of continuous density graded cellular materials. The impact energy absorption of cellular materials is very high. On the other hand, impulse transmission capacity is quite low. These are two contradictory indicators for cellular materials with different gradients and distributions. In this study, the waves were modeled as a uniform pressure that is attenuated over time. The material has a positive density gradient (the gradient is positive if the initial density increases from the proximal end to the distal end), which increases in the direction of the shock waves. The shock waves were modeled using the *Jones-Wilkins-Lee* equation which is used to model the detonation of explosives. There was a good correlation between the numerical results obtained with finite elements analysis and the theoretical predictions. The capacity to absorb energy and transfer a small amount of charge, makes cellular materials very appealing to be used in protection against explosives.

The study concluded that for structures with a positive gradient, the absorption and consequent transmission were maximum while for negative gradient, the absorption and consequent transmission were minimal.

Recent works combined new structures of cellular materials with the new technological processes of additive manufacturing [4,6,22,23].

H. Araujo et al. [4] studied the effect of geometry on the flexural properties of cellular core structures. Three different types of core design were studied, namely structures with Hexagonal core design, Lotus and Plateau (Hexagonal with chamfered vertices). 3-point bending tests were performed for four different densities for each core design. For the higher density cases, the design that performed better was the Lotus and for the lower density cases, the structure that performed better was the Hexagonal.

The zone of maximum stress is independent of the geometry and relative density. From the numerical analysis, one can observe that in any of the cases studied, the central region was the one subjected to the most stress. As such, these structures are cellular but not functionally graded structures, as they don’t have density gradient. Structures with the same core design, but with density gradient should be studied.

H. Araújo et al. [6] investigated the contribution of geometry on the failure of cellular core structures obtained by additive manufacturing. Load direction angles were found to have a strong influence in the failure mode. Among the three structures, and for the same relative density, the Lotus geometry exhibited the highest stiffness and strength. However, the absorbed energy was found to be higher for honeycomb, at two loading directions. The effect of the geometry in the properties obtained in compression can be state as follows: the Lotus arrangement (which is considered to be a prismatic solid), gives rise to higher values of strength and stiffness in comparison with the Plateau configuration (that possesses an accumulation of material at vertices) and the conventional Hexagonal honeycomb. The failure modes differ with the loading direction but are similar for the three geometries. Failure zones present at the same localization in both the experimental and numerical data.

J. Bru et al. [22] studied bioinspired structures for core sandwich composites produced by fused filament fabrication. The authors concluded that the mechanical properties showed a strong dependence on the relative density and on the cell thickness distribution. Under compression, a bioinspired arrangement provides good responses, exhibiting values of loads of the same order of magnitude than the ones achieved by the honeycomb configuration. However, under flexural loading, this configuration showed low load-bearing capacity, even for the highest relative density. It was also concluded that the properties of cellular solids may be changed through controlling and manipulating their topology.

C.M.S. Vicente et al [23] and *J. Fernandes et al.* [24] studied the mechanical properties of additively manufactured PLA and several parameters at the printing process [23,24]. These PLA properties were the ones utilized in this study.

2.3 Relative Density

One of the most relevant properties of cellular solids is the relative density. It is an important indicator to compare the performance of regular honeycomb structures with functionally graded cellular structures. The relative density $\bar{\rho}$ is obtained by the division of the density of the cellular material, (ρ^*), by the density of the solid from which the cell wall is made from. The relative density is a fraction of the total volume, according to Gibson [7,25]. Also, this fraction of volume is unit complementary of porosity.

There is a distinction between cellular structures, depending on the relative density value. Cellular structures that have a relative density less than 0.3 are considered cellular solids. For those cellular structures that have a relative density higher than 0.8 (Figure 2.5), it is said that there are isolated pores in solid [7,25].

Figure 2.5 - Examples of cellular solid and isolated pores in solid [7,25].

The formula to compute the relative density is the following:

$$\frac{\rho *}{\rho_s} = \frac{\mathrm{Ms}}{V_T} \times \frac{\mathrm{Vs}}{\mathrm{Ms}} = \frac{\mathrm{Vs}}{V_T} = volume\ fraction\ of\ solid\ (= 1 - porosity\ )$$

where M stands for mass and V stands for volume, with S standing for solid and T standing for total. As ($\frac{\rho *}{\rho s}$) increases, cell edges (and faces) thicken and pore volume decreases. The typical values for the relative density of some cellular materials are given in Table 2.1.

Table 2.1 - Typical values for relative density [7,25].

Type of Structure	Relative Density Value
Typical Polymer Foam	[0.02; 0.2]
Soft Woods	[0.15; 0.4]

2.4 Production methods

The cores of the sandwich panels are made using different methods. The technologies used for functionally graded materials are very expensive and time consuming, limiting the use of such materials to very selective engineering applications [2]. Functionally graded materials, as well as cellular materials, can be divided in two categories: honeycombs and foams [7]. In this section, a description of honeycomb manufacturing processes will be made due to its uniqueness in comparison to more traditional manufacturing processes. Then, some characteristics of additive manufacturing processes will be explained.

2.4.1 Honeycomb traditional manufacturing processes

There are five basic ways of manufacturing honeycomb structures, namely: adhesive bonding, resistance welding, brazing, diffusion bonding and thermal fusion. All these processes are based on how the joining between sheets is made to form a *node.* Among these methods, the most common manufacturing method is adhesive bonding (more than 90% of traditional manufactured honeycombs). Resistance welding, brazing and diffusion bonding are only used for cores at very high temperatures.

There are two basic methods of manufacturing honeycomb core by adhesive bonding. The first is the expansion method and the second is the corrugation method.

2.4.1.1 Expansion method

Of the two methods mentioned, the expansion method is the most common process of the two. Almost all honeycombs produced by adhesive bonding use this manufacturing technique. For metallic honeycombs a corrosion protective layer is applied.

This process consists in cutting sheets and applying an adhesive bonding in specific areas. Figure 2.6 illustrates the process and Figure 2.7 explains the method step-by-step.

First, a metal sheet roll is rolled out, and then adhesive is applied, in specific areas as seen in the second stage of the process. This adhesive after being applied is submitted to a cure in high pressures and temperatures. After that, the sheets are piled on top of each other, in step 3 (Honeycomb Before Expanded (HOBE) Block). The 4th step consists in slicing the HOBE Block after which, it is expanded into its final shape [26].

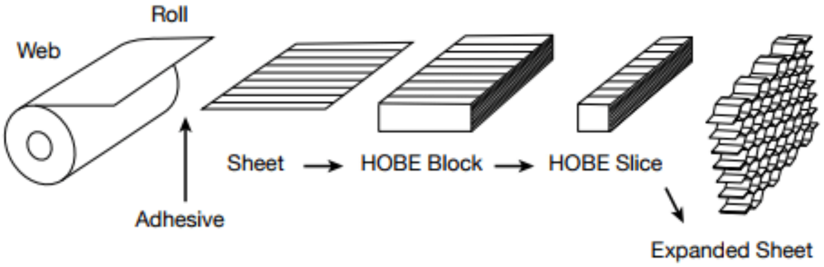

Figure 2.6 - Expansion method illustration [27].

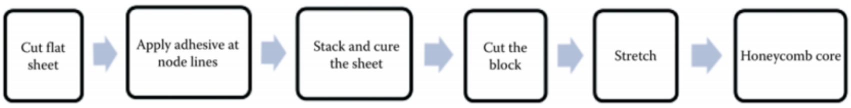

Figure 2.7 - Expansion method step-by-step [27].

Once it is compact, the HOBE Block is frequently the finished product that can be supplied directly to the costumer, occupying minimum space and costing less for shipping with lower risk of damage compared to the expanded version [28].

In non-metallic honeycombs, some structures cannot hold their geometry after the expansion, and it is necessary to use supports and to cure them in an oven. Afterwards, most of paper honeycombs (namely Nomex) can maintain their shape and geometry.

Nevertheless, some larger structures cannot maintain their geometries. Because of that, they are submerged in a liquid resin, usually phenolic or polyamide, and cured repeatedly until the wanted density is achieved.

2.4.1.2 Corrugation method

This process was the original honeycomb manufacturing method. This procedure is more labor intensive compared to the expansion method presented before, and it is used with high-density materials and nonmetallic cores.

Contrary to the expansion process, the corrugation process introduces pre-formed corrugated sheets prior to applying the adhesive, and therefore eliminates the need for expansion.

It consists in the use of a roll of material and corrugated rolls as showed in Figure 2.9.

The foil substrate first passes through a pair of corrugated rollers that are specially designed to manufacture the honeycomb, becoming a corrugated sheet. The sheets are pressed into half-hexagonal shapes, the profile with adhesive is applied to the corrugated points. The sheets are then cut into the desired dimension (length) and the adhesive is applied to the node lines. The corrugated sheets are then stacked into blocks and cured. Figure 2.8 illustrates the corrugation method and Figure 2.9 presents the method step-by-step.

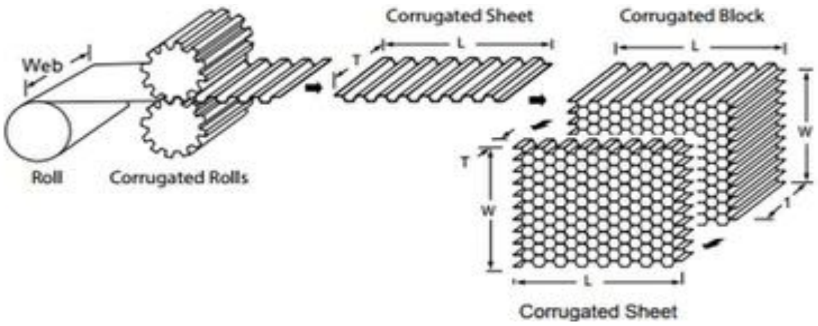

Figure 2.8 - Corrugation method scheme [27].

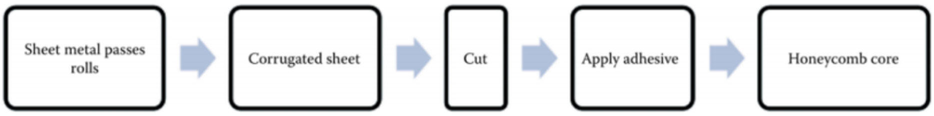

Figure 2.9 - Corrugation method step-by-step [27].

Both manufacturing methods offer a range of cell configurations for different requirements such as formability, curving, energy absorption, and strength. The corrugation process is more complex and time consuming compared to the expansion process. Hence, the corrugated honeycomb core is usually more expensive.

2.4.2 Additive manufacturing

With the development of technology, some new manufacturing processes were created. Additive manufacturing, AM, is most commonly known as 3D printing.

Highly advanced geometries, like FGCM are only made possible with new manufacturing processes.

Additive manufacturing represents a new era in the industry. AM is a name that is used by the ASTM International F42 committee on additive manufacturing standard to describe the group of technologies that build three-dimensional objects by adding materials layer by layer from a computer aided design (CAD) model for the object. It consists of a set of technologies for the manufacture of three-dimensional objects by material overlapping layer upon layer [29].

Appropriate materials are critical to the selection requirements for AM. Materials requirements for AM include the ability to produce the feedstock in a form amenable to the specific AM process with suitable processing of the material by AM, enabling the creation of parts with the required shaped. There is a wide range of materials that can be used, from polymers and ceramics to metals and glass [30].

There are several AM categories (Figure 2.10). Processes are often sub-divided according to the energy source used and/or the raw material delivery method.

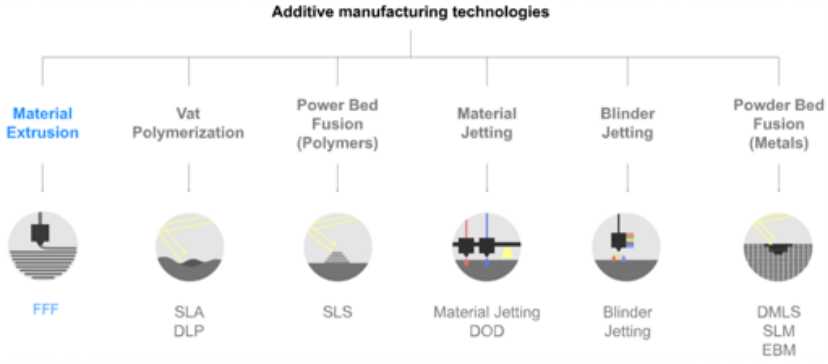

Figure 2.10 - Additive manufacturing processes [31].

For metals, there are two energy sources widely used in industry: lasers and electron beam. There are also two material-delivery methods: 'powder bed' and 'blown powder' [28]. Due to the vast range of processes, there are seven different categories according to ASTM F42, and those categories are the following: Material Extrusion, Material Jetting, Sheet Lamination, Vat Photo Polymerization, Directed Energy Deposition and Powder Bed Fusion.

2.4.2.1 Fused filament fabrication

Fused deposition method (FDM), recently renamed of fused filament fabrication (FFF) is one of the most used additive manufacturing processes today.

FFF, or FDM, is an additive manufacturing process that belongs to the material extrusion family. In FFF, an object is built by selectively depositing melted material in a pre-determined path layer-by-layer (Figure 2.11). The materials used are thermoplastic polymers and come in a filament form.

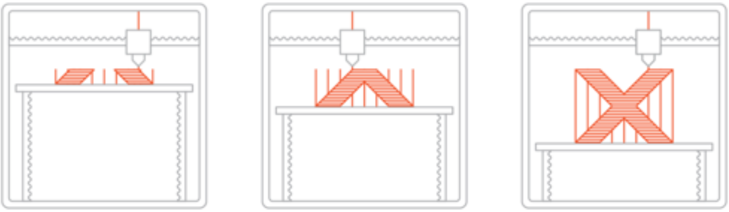

Figure 2.11 – Fused filament fabrication process [17].

The process consists in three steps:

1. A spool of thermoplastic filament is first loaded into the printer. Once the nozzle has reached the desired temperature, the filament is fed to the extrusion head and into the nozzle where it melts. **2**. The extrusion head is attached to a 3-axis system that allows it to move in the X, Y and Z directions. The melted material is extruded in thin strands and is deposited layer-by-layer in predetermined locations according to the CAD model, where it cools and solidifies. Sometimes the cooling of the material is accelerated using cooling fans attached to the extrusion head. **3**. To fill an area, multiple passes are required (like coloring a rectangle with a marker). When a layer is finished, the build platform moves down (or in other machine setups, the extrusion head moves up) and a new layer is deposited. This process is repeated until the part is complete. A schematic of this method is presented in Figure 2.12.

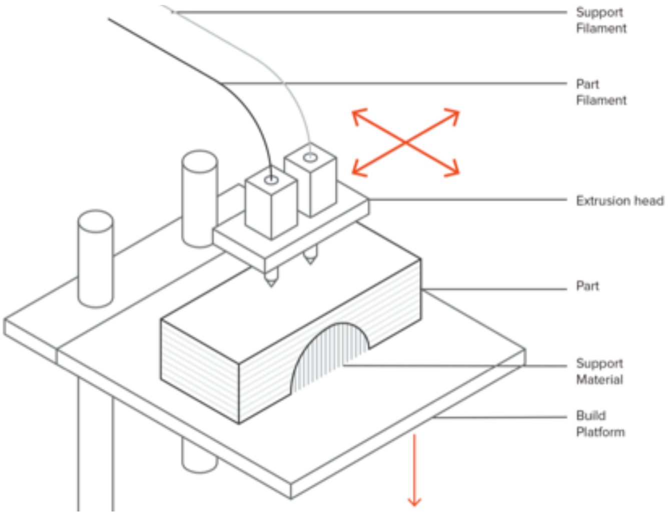

Figure 2.12 - Fused filament fabrication schematic [32].

Printer Parameters

The FFF manufacturing procedure has several process parameters, and they have a significant impact on production efficiency and part characteristics. Some of the most common process parameters are air gap, built orientation, extrusion temperature, infill density, infill pattern, layer thickness, print speed, raster orientation and raster width [32].

Air gap is the gap between two adjacent rasters on a deposited layer. It is called negative when two adjacent layers are overlapped. The built orientation is defined as the way to orient the part in the built platform with respect to corresponding axes. The extrusion temperature depends on various aspects, for example, the type of material or print speed. The outer layers of a three-dimensional (3D) printer object are compact. However, the internal structure, commonly known as the infill, is an inner part covered by the outer layer(s), and it has different shapes, sizes, and patterns. Infill density is the percentage of infill volume with filament material. The strength and mass of FFF build parts depend on the infill density [33].

From a designer's point of view, other aspects are as important, such as the built size and the layer height. Usually, the built size varies from 200 x 200 x 200 mm^3 for desktop 3D printers to 1000 x 1000 x 1000 mm^3 for industrial ones [34]. The layer thickness is usually between 50 and 400 microns, being 200 microns the most common height.

FFF Materials

The compatibility of the FFF manufacturing process with a wide range of materials is one of its main advantages. It has the capacity to use a considerable range of thermoplastic materials. The most used materials in FDM manufacturing are PLA (Poly-lactic Acid) and ABS (Acrylontrile Butadiene Styrene). However, high performance thermoplastics are also used. From these, the most relevant are the following: PEEK (Polyether Ether Ketone) and PEI (Polyethylenimine). Additionally, PETG (Polyethylene Terephthalate) and TPU (Thermoplastic Polyurethane) are used as well. Figure 2.13 shows the most common thermoplastics used in FFF as well as the distinction between the different types.

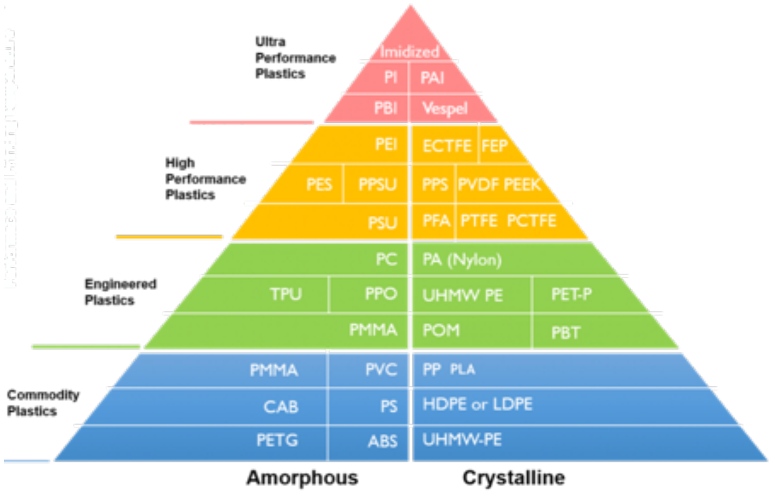

Figure 2.13 - Fused filament fabrication materials [35].

The material used has a direct impact on the mechanical properties of the part printed as well as the printing quality and the price. Table 2.2 presents the characteristics of some common materials [36].

Table 2.2 - Fused filament fabrication most common materials characteristics [36].

Material	***Characteristic 1***	***Characteristic 2***	***Characteristic 3***
ABS	Good strength	Good temperature resistance	Suitable to warping
PLA	Easy to print	Excellent visual quality	Low impact strength
TPU	Very flexible	Bad accuracy	-
PEEK	Radiation and chemical resistance	Superior weight/strength	Creep resistant
PETG	Food safe	Easy to print	Good strength
PEI	Excellent weight/strength	Fire and chemical resistance	High price

Layer Adhesion

As important as choosing the material to use and the printing parameters is to allow a good adhesion between the deposited layers. To achieve a good layer adhesion, it is important to consider the mechanism of FFF manufacturing. Once the filament exits the nozzle, the molten thermoplastic is pressed against the preceding layer. This mechanism allows the previous layer to partially re-melt and helps the bonding of the layers. The pressure applied over the precedent layers and the re-melting process deforms its shape to an oval. Because of that deformation, FFF parts will always have a nonlinear surface, even when the layer height is kept to a minimum (although the defect is reduced) [37].

The depositions layer by layer, and the layer bonding process makes the FFF parts anisotropic. Therefore, the strength between layers is always smaller than the strength in the same plane. The orientation, for that reason, has a very important role in the mechanical characteristics of the printed part. Because of that it is important to keep a part orientation perspective while designing the FFF parts. Figure 2.14 represents the deformation presented in FFF printed parts.

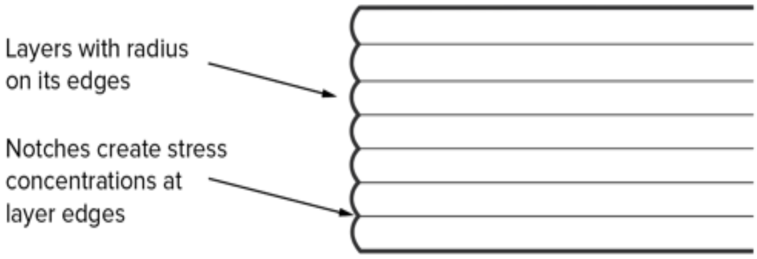

Figure 2.14 - Deformation present in FFF printed parts [38].

Most common FFF defects

It is very common to have defects in FFF printed parts. The most common defects are presented next as well as cause of these defects and possible solutions. The most common defects are warping, layer shifting, gaps in top layer and stringing.

Warping

The warping effect (Figure 2.15), as the name suggests, happens during the cooling of the material after being extruded. Warping is one of the most common defects in FFF. This defect changes the final dimensions of the extruded structure. The result is a decrease of the dimensions, which is different for different parts of the structure.

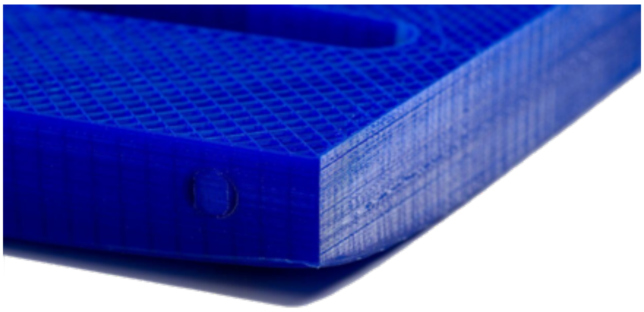

Figure 2.15 - FFF warping defect [39].

Differential cooling causes the buildup of internal stresses that pull the underlying layer upwards. There are ways to prevent this phenomenon from occurring, such as: monitoring the temperatures of both build platform and chamber; increasing the adhesion between the structure and the built platform; reducing large flat areas since these are keener to warp; decreasing the thickness of the structures as thin structures have less tendency to warp and avoiding sharp edges by adding fillets in the design.

Layer Shifting

Most commonly, 3D printers use an open-loop control system, and because of that, there is no feedback about the actual location of the tool head. The machine is simply programmed to move the tool head in a specific path (using G-code) but there is no feedback sent to the printer to detect eventual misplacement. Figure 2.16 illustrates the layer shifting.

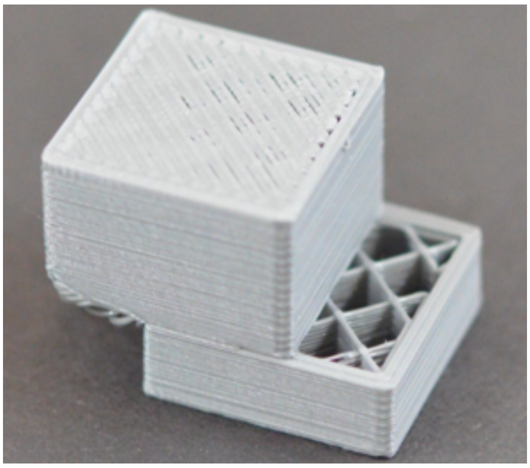

Figure 2.16 - FFF layer shifting defect [40].

With this lack of feedback, if there is some outer movement, or vibrations, that cause the tool head to shift to a new not intended position and not having feedback, the machine will continue printing causing layer shifting. There are some methods to prevent this phenomenon. The most common one is reducing the printing speed. Another solution could be fixing the electrical current, since low electrical current causes layer shifting, and having a good and strong continuous current during the printing process is key to achieving the best possible results [36].

Gaps in top layer

Most 3D printed models are created to have a solid shell that surrounds a porous, partially hollow interior. Due to that, and depending on the used setting, the top solid layer may not be completely closed, resulting in gaps and holes between the extrusions (Figure 2.17). To prevent this phenomenon, settings can be changed. A possible cause can be not having enough top slid layers, another possible cause is the infill percentage being too low. To solve the first problem, a reinforcement of the affected area with more layers will fill the original gaps. As for the second, the infill percentage must be increased [36].

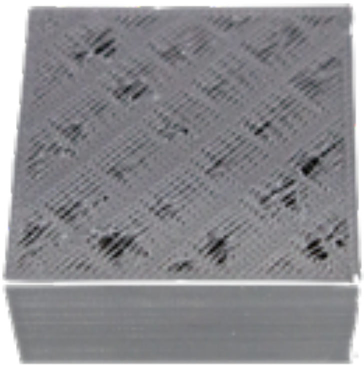

Figure 2.17 - FFF gaps in top layer defect [41].

Stringing

Stringing phenomenon, also called oozing, occurs when small strings of plastic are left behind on a 3D printed model. This phenomenon is mainly due to plastic oozing out of the nozzle while the extruder is moving to a new location (Figure 2.18). There are some ways to prevent it from happening. The most common setting used to eliminate excessive stringing is known as retraction. When retraction is enabled, the filament is pulled backwards into the nozzle, to act as a countermeasure against oozing. The retraction distance as well as the retraction speed can be adjusted to minimize oozing. The distance determines how much plastic is pulled out of the nozzle. The speed determines how fast the filament is retracted from the nozzle. Another way to prevent this defect is by controlling the temperature. If it is too high, the plastic will become less viscous and will leak out of the nozzle more easily. If the temperature is too low, the plastic will still be solid, and extrusion will be more difficult.

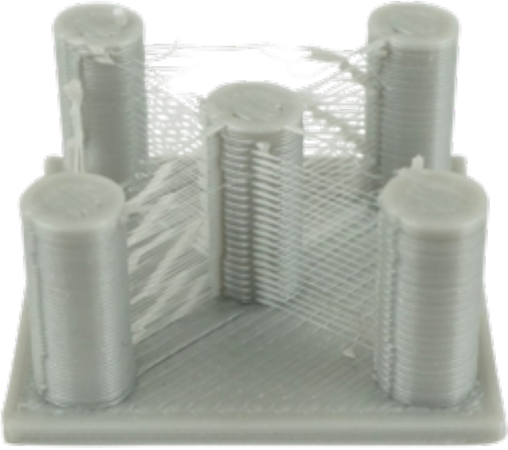

Figure 2.18 - FFF stringing defect [42].

2.4.2.2 Selective Laser Melting

Selective laser melting (SLM) is a laser powder bed fusion (LPBF) technique which uses a laser beam to melt a power bed selectively.

This AM process can use a wide range of materials such as metal, polymers, ceramic or composites. All materials should be in the form of fine powder. Powder can be generated from ingots using various techniques, such as gas atomization or plasma atomization. LPBF processes that use metallic powder are, nowadays, one of the most versatile and used AM processes, allowing the production of geometrically complex components in titanium or aluminum alloys or even materials such as stainless steel [43,44].

Selective laser melting enables the production of parts with complex geometries while maintaining the mechanical properties of parts conventionally manufactured in series as per example with casting manufacturing. SLM does not have the need of part-specific tools and so, the pre-production costs become inexistent for serial manufacturing from materials such as steels, aluminums, titanium and nickel-based alloys. Since standard metallic powders that melt completely are used in this process, it allows the parts have a density of approximately 100% which assures series identical properties and enables mechanical properties that match or even surpass those of conventionally manufactured parts (cutting and casting processes) [45]. A scheme of the SLM procedure is illustrated in Figure 2.19.

Figure 2.19 - Selective laser melting process [46].

SLM, as other manufacturing processes, has its advantages and disadvantages. The advantages are the following: wide range of compatible metals, reduced lead times due to no need for tooling, ability to produce complex shapes or internal features and part consolidation allowing the production of multiple parts at the same time. Disadvantages are related to the complexity of the process making it expensive. Also, the need arises for specialized design and manufacturing skills and knowledge. Production is currently limited to small parts due to available SLM machine sizes. Moreover parts exhibit rough surface finish and require intensive post-processing[47]. Figure 2.20 presents an example of a SLM printed part.

A SLM machine has a chamber filled with metal powder. The manufacturing process begins with the deposition of a very thin layer of powder over a built plate by a coater blade. The thickness of these layers can vary between 20 – 100 µm, depending on the pretended model's superficial quality and the process speed.

Figure 2.20 - SLM printed sample [48].

The used lasers have a very high power density. These lasers are guided, through a set of scanning mirrors, to the place where the material powder will be deposited, copying the information given by the .STL file used in the process. The laser being a high-power beam (usually an ytterbium fiber laser), has a high thermal energy, that fuses a 2D slice of the part by selectively melting the powdered material. After being melted, the powder slowly solidifies. The built plate then drops down by the height of one layer, and the coater spreads another layer of fresh powder finely across the surface. At this process moment, it must be noted that the laser exposure is set to melt a percentage of the previous layer, allowing the new layer to melt completely with the previous layer. The process is repeated until the last layer is concluded, the part then being removed from the machine chamber. The remaining powder, not used in the process, is also removed. The surface finish of the sintered parts is rough and post-processing is required.

The entire process is performed in a controlled atmosphere inside the machine. In SLM, inert gas flow, for example argon or nitrogen, is needed to maintain the atmosphere within the build chamber. The inert gas is needed to minimize contamination of the parts during high-temperature processing and to remove the condensate produced during the melting process. This condensate can result in reduction in the effective laser energy reaching the powder bed. Other parameters that should be controlled are temperature, pressure and flow rate and capacity [49].

SLM is used to manufacture functional prototypes and to build up final parts directly. The field of commercial applications is limited to single parts or small batches. Some industries in which SLM is utilized are the following: tool and mold making industries (small batches and almost infinite geometrical freedom), medical technology (individual implants, hip implants or surgical instruments out of titanium alloys as well as dental restorations out of cobalt chromium), aerospace, automotive and naval industries [45].

2.5 - Finite Element Method

One of the most important tasks engineers and scientists perform is to model physical phenomena. Virtually every phenomenon in nature, whether aerospace, biological, chemical, geological, or mechanical can be described with the aid of the laws of physics or other fields in terms of algebraic, differential, and/or integral equations relating various quantities of interest [50].

Analytical descriptions of physical phenomena and processes are called mathematical models. Mathematical models of a process are developed using assumptions concerning how the process works and by using appropriate axioms or laws governing the process, and they are often characterized by very complex differential and/or integral equations posed on geometrically complicated domains. However, a large amount of real-life practical problems do not allow for the development of analytical solutions, because they have complex loading and boundary conditions, as well as the above mentioned highly complex geometrical domains.

A numerical method, with the aid of a computer, can be used to investigate the effects of various parameters (per example geometry, material parameters, or loads) of the system response, to gain a better understanding of the process/system being analyzed. It is cost-effective and saves time and material resources compared to the multitude of physical experiments needed to gain the same level of understanding.

The finite element method (FEM) is a numerical method like the finite difference method but is more general and powerful in its application to real world problems that involve complicated physics, geometry, and/or boundary conditions. Nowadays, finite element analysis is an integral and major component in many fields of engineering design and manufacturing. Major established industries rely on the finite element method to simulate complex phenomenon at different scales for design and manufacture of high-technology products.

The method is composed by three distinct features that account for its superiority over other competing methods. The three features are the following [50]:

1. The domain of the problem is represented by a collection of simple subdomains, called finite elements. The collection of finite elements is called the finite element mesh;

2. Over each element, the physical process is approximated by functions of the desired type (polynomials or otherwise), and algebraic equations relating physical quantities at selective points of the element, called nodes, are developed;

3. The element equations are assembled using continuity and/or “balance” of physical quantities.

To determine the global solution of the problem, it is necessary the assembly of element equations, considering the numeration previously attributed to each finite element and its distribution over the global problem domain. In practice, the assembly of element equations consist in making compatible the values of the dependent variables in each finite element knots. After this step, the problem boundary conditions must be imposed and the resolution of the system global equation are done. Once the solution is obtained, a post-processing must be developed which consists in obtaining secondary variables (obtained from the primary variables) and the results can be observed and analyzed.

At last, it is important to perform a convergence study of the primary variable, to ensure a higher solution precision by increasing the mesh refinement (increasing the number of finite elements). Usually, it is better to use quadratic or higher order approximation functions in detriment to linear functions. However, this leads to a higher computational time and space consumed since the number of knots, and consequently, the number of finite elements is higher [50].

Chapter 3

Experimental methods

In the present study, several different functionally graded cellular structures were designed. In total, twenty-three structures were made. Five sets of three structures were designed to have the same density gradient (different gradients for each set of three structures), only differing in core design. There are three basic designs: Hexagonal, Lotus and Plateau (Figure 3.1). For each set of three structures, there is also a Lowerbound and an Upperbound structure, both structures having a homogeneous distribution and a Hexagonal core. They are intended to compare the FGC with standard honeycomb structures. The Upperbound represents the standard honeycomb structure with the smaller core size and presents the higher initial stiffness and absorbed energy values for the standard honeycomb. The Lowerbound, is the standard honeycomb with the larger core size and consequently presents the lower initial stiffness and absorbed energy values for the standard honeycomb. Both the size for the Upperbound and Lowerbound cores are in concordance with the correspondent functionally graded cellular structures.

These structures were subjected to 3-point bending (3PB) tests, both experimentally and through Finite Element Analysis (FEA).

Figure 3.1 - A- Hexagonal core, B- Lotus core, C- Plateau core.

3.1 – Design

3.1.1 – Material

The materials selected to conduct this experiment were poly-lactic acid (PLA) and Aluminum-A.

The PLA was selected since it is one of the most used materials in FFF manufacturing. It is a biodegradable (degrades into innocuous lactic acid) thermoplastic polymer (aliphatic polyester) derived from renewable resources such as cornstarch or cereals. It is one of the most popular bio plastic used, and it is very common in FFF additive manufacturing. Known for its good mechanical properties, as its high Young's modulus and high strength, this thermoplastic is used in a wide set of applications from food packaging, plastic cups to medical implants [22].

PLA was discovered in the 1920s by an American chemist and inventor Wallace Carothers (who also created nylon), and since then, it has been vastly studied. PLA has become a popular material because it is produced economically from renewable resources. Because of that, in the 2010s it had the second highest consumption in volume of any bio plastic [51]. Aluminum is also a very popular material for the core of sandwich panels.

Since the PLA properties can change from case to case, because of the manufacturing processes and specifications, the properties used in the present project are the following, as presented in Table 3.1. They were obtained by *Fernandes et al.* [24] in PLA compact specimens under linear tensile loading. Table 3.1 and 3.2 presents the properties of the PLA and Aluminum-A. The used PLA filament was the Filkemp print master pro (Figure 3.2).

Figure 3.2 - Filkemp PLA 3D printer filament used.

Table 3.1 - PLA properties.

Density (g/cm^3)	**1.252**
Young's Modulus (MPa)	1750
Poisson ratio	0.36
Tensile strength (MPa)	20
Elongation at break (%)	7

Table 3.2 - Aluminum-A properties.

Density (g/cm^3)	**2.680**
Young's Modulus (GPa)	59
Poisson ratio	0.33
Tensile strength (MPa)	211
Elongation at break (%)	8

3.1.2 – G parameter

A very important parameter when analyzing functionally graded cellular structures is the one designated by G parameter, developed in the present work, in which G stands for gradient. Its main purpose is to quantify the density gradient in a FGC structure. With it, one can compare different structures with different density gradients. This parameter is computed using different measurements in the FGC structure and it is illustrated in the scheme below (Figure 3.3). The first one is L (length of half the structure), l (length of the core including wall thickness), X (length from the start of the structure until the end of the cell wall thickness) and d (cell wall thickness).

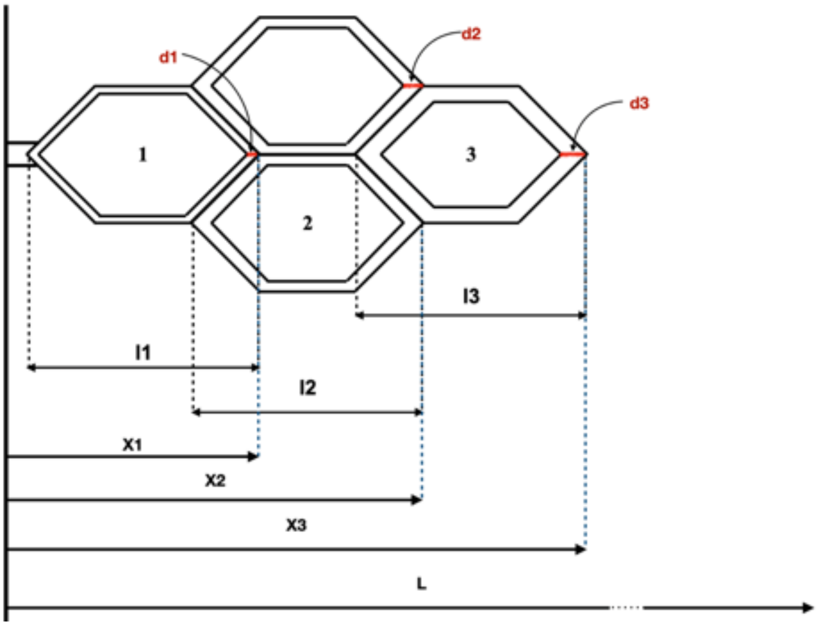

Figure 3.3 - Schematic of G parameters.

After obtaining the values for the different measurements, then a plot is made and the slope of the curve is the value of the G parameter (Figure 3.4). The bigger the G parameter value is, the steeper is the density gradient present in the structure.

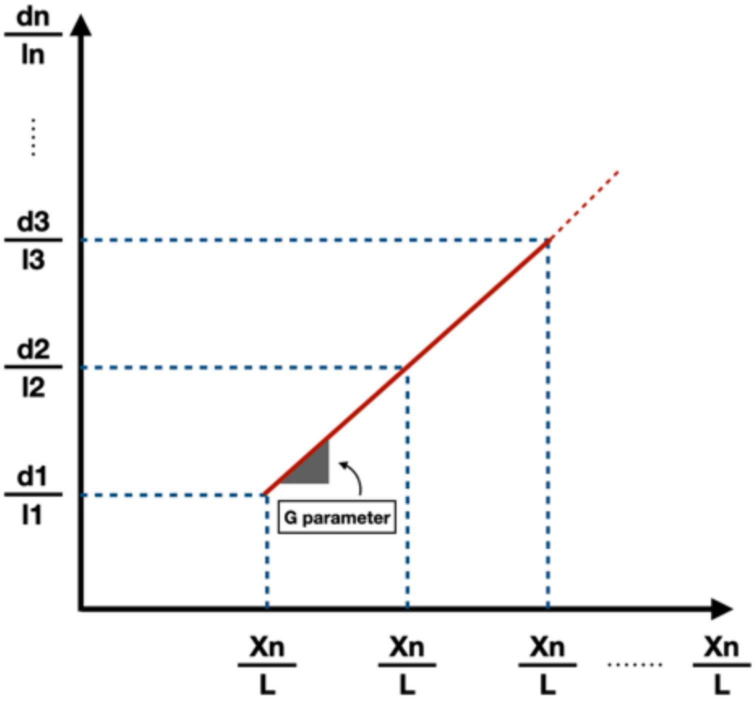

Figure 3.4 - G parameter, seen as a slope.

3.1.3 – Specimens design

As already mentioned in the beginning of this chapter, in total twenty-three structures were made in computer-aided design (CAD). The CAD software used was Solidworks 2018 Student Edition. The dimensions of the specimens are the same for all PLA specimens. They have the following dimensions: 163.8 mm in length, 54 mm in width and 22 mm in thickness (Figure 3.5).

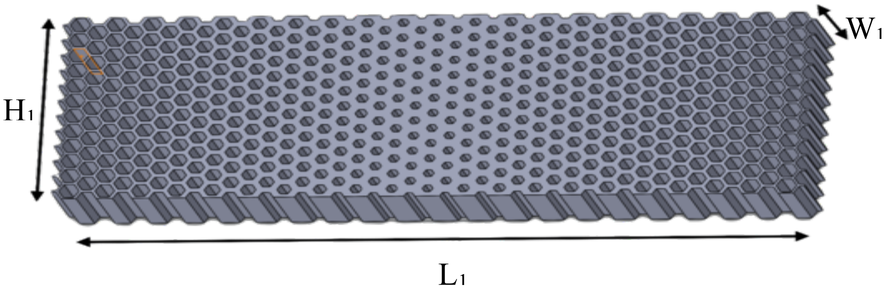

Figure 3.5 - PLA specimens dimensions: L_1 - length, H_1 - height, W_1 - width.

There are three different density gradients, characterized by the G parameter [54]. In graded structures (Figure 3.5) the cell wall thickness increases from the surface to the center of the specimen, decreasing until the opposite surface. In such a way, there is a minimum thickness d_{min} and a maximum thickness d_{max} of the cell walls.

Despite some small variations, it was considered the G parameter as being constant for each set of three geometries (Hexagonal, Lotus and Plateau). The value of the G parameter is zero when the gradient is null. The nomenclature used for the structures was the following: the first designation stands for the core design (Hexagonal, Plateau or Lotus), followed by d which stands, by definition, for cell wall thickness and then the corresponding value. Having the plots, by analyzing the slope of the curves, the G parameter is computed. Table 3.3 presents all the values of G parameter. The structures will be denoted by the minimum and the maximum thickness of the cell walls. The data needed to compute the G parameter values is presented in Appendix A.

Table 3.3 - List of G parameter values for different structures.

Structures	***d_{min} [mm]***	***d_{max} [mm]***	***G parameter***
d 0.25 – d 1.25	0.25	1.25	0.212
d 0.25 – d 0.75	0.25	0.75	0.105
d 0.80 – d 1.20	0.80	1.20	0.091
d 0.815 – d 1.165	0.815	1.165	0.080
d 0.74 – d 1.48	0.74	1.48	0.677

3.1.3.1 – PLA Hexagonal structures

There were three different Hexagonal structures, each of them with different G parameters. Two of them (d 0.25 – d 1.25 and d 0.5 – d 0.75) have the same starting wall thickness of 0.25 mm. The third (d 0.80 – d 1.20) has a starting wall thickness of 0.8 mm due to FFF machine nozzle specifications. Table 3.4 presents the G parameter and relative density for each of the Hexagonal structures. The relative density was obtained, for all specimens, using the Solidworks surface area command and using the external dimensions of the solid. The Figure 3.6 presents PLA Hexagonal structures.

Table 3.4 - List of G parameter values and relative density for PLA Hexagonal structures.

Structures	***G parameter***	***Relative density***
Hexagonal d 0.25 – d 1.25	0.212	0.552
Hexagonal d 0.25 – d 0.75	0.105	0.399
Hexagonal d 0.80 – d 1.20	0.091	0.684

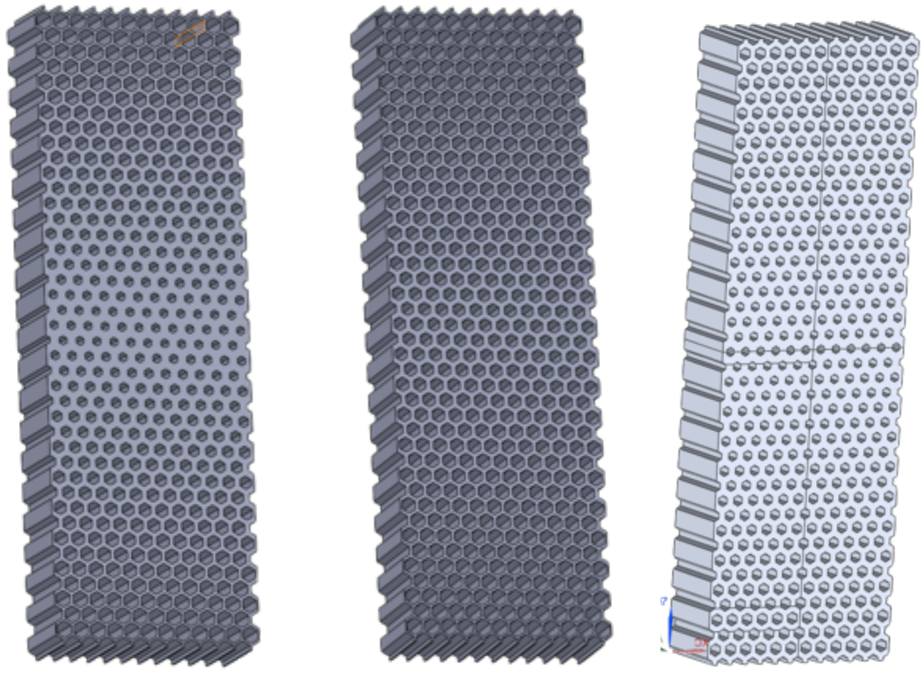
a) b) c)

Figure 3.6 - PLA Hexagonal structures, a) *Hexagonal d 0.25 – d 1.25, b) Hexagonal d 0.25 – d 0.75 and c) Hexagonal d0.80-d1.20.*

3.1.3.2 – PLA Plateau structures

Similarly, to the Hexagonal structures, Plateau graded structures were obtained. The table 3.5 shows the G parameter and relative density for each of the Plateau structures. The Figure 3.7 represents the PLA Plateau structures.

Table 3.5 - PLA Plateau structures G parameter and relative density values for different structures.

Structures	***G parameter***	***Relative density***
Plateau d 0.25 – d 1.25	0.212	0.554
Plateau d 0.25 – d 0.75	0.105	0.401
Plateau d 0.80 – d 1.20	0.091	0.685

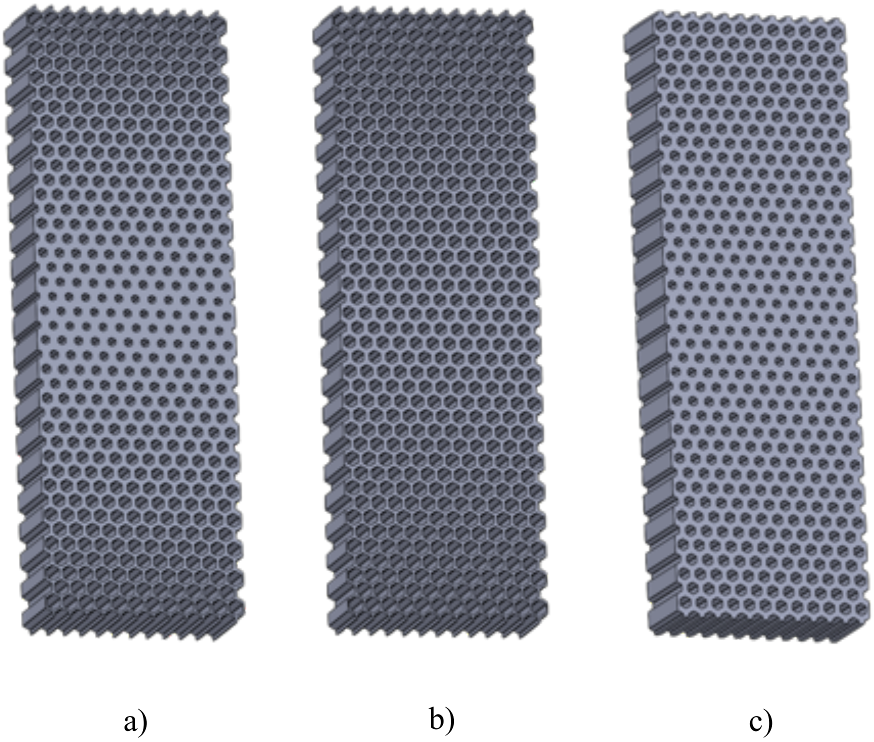

Figure 3.7 - PLA Plateau structures, a) Plateau d 0.25-1.25, b) Plateau d 0.25-0.75 and c) Plateau d 0.80–1.20.

3.1.3.3 – PLA Lotus structures

Once again, for the Lotus structures, the same specifications were applied. The Table 3.6 shows the G parameter and relative density for each of the Lotus structures. Figure 3.8 represents the PLA Lotus structures.

Table 3.6 - PLA Lotus structures G parameter and relative density values for different structures.

Structures	***G parameter***	***Relative density***
Lotus d 0.25 – d 1.25	0.212	0.589
Lotus d 0.25 – d 0.75	0.105	0.455
Lotus d 0.80 – d 1.20	0.091	0.713

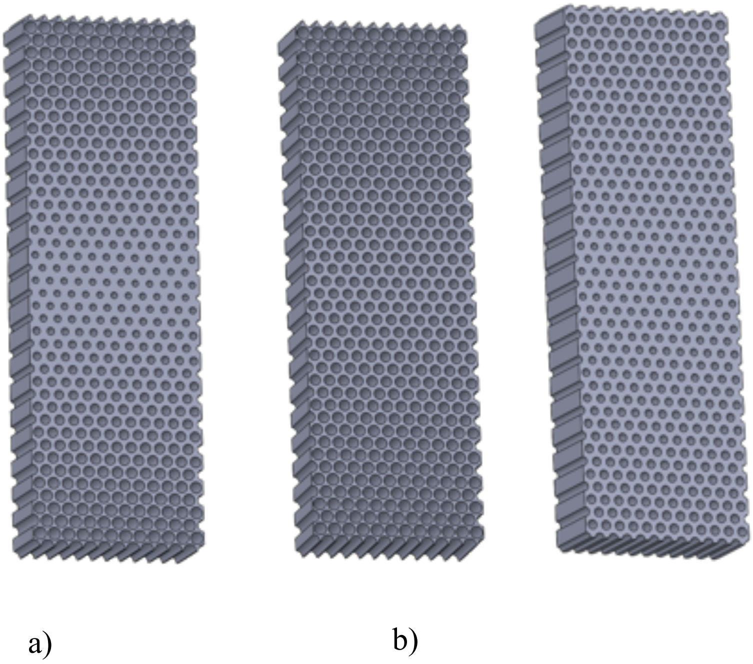

a) b) c)

Figure 3.8 - PLA Lotus structures, a) Lotus d 0.25-1.25, b) Lotus d 0.25-0.75 and c) Lotus d 0.80-1.20.

3.1.3.4 – 90-degree angle of rotation structures

These structures were made rotating the core arrangement in 90-degrees. They have the same dimensions of the other standard 0-degree rotation structures. The Table 3.7 presents the value for the G parameter and for the relative density. Figure 3.9 shows the 90-degree Hexagonal structure.

Table 3.7 - 90-degree rotation PLA structures G parameter and relative density values for different structure.

Structures	***G parameter***	***Relative density***
Hexagonal_90 d 0.74 – d 1.48	0.677	0.678
Plateau_90 d 0.74 – d 1.48	0.677	0.679
Lotus_90 d 0.74 – d 1.48	0.677	0.687

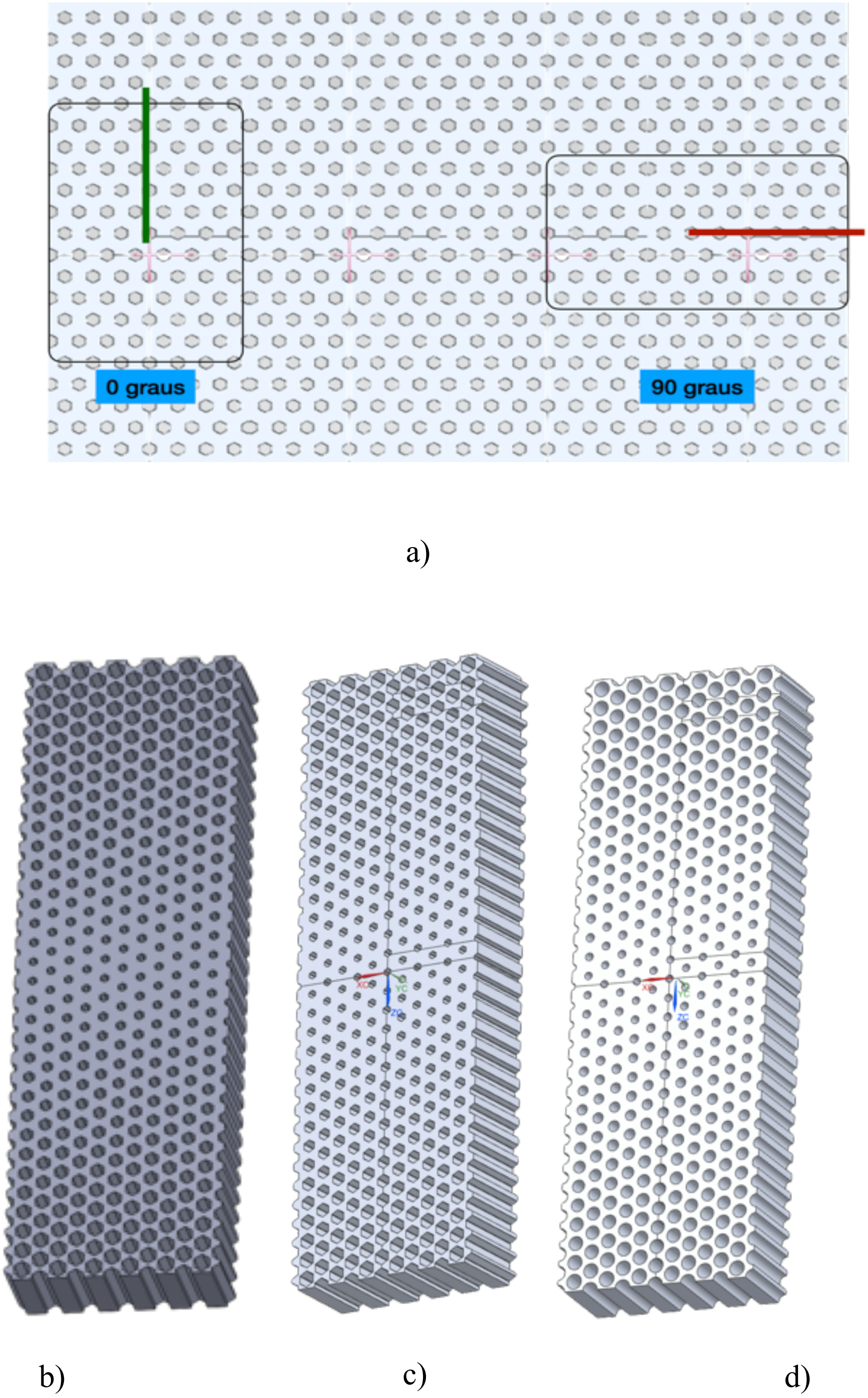

a)

b) c) d)

Figure 3.9 - 90-degree rotation PLA structures: a) Illustration of the rotation, b) Hexagonal_90 d 0.74-1.48, c) Plateau_90 d 0.74-1.48 and d) Lotus_90 d 0.74-1.48.

The Upperbound represents the standard honeycomb structure with the smaller core size and presents the higher values for the standard honeycomb. The Lowerbound, is the standard honeycomb with the larger core size and consequently presents the lower values for the standard honeycomb. Both the size for the Upperbound and Lowerbound cores are in concordance with the correspondent functionally graded cellular structures.

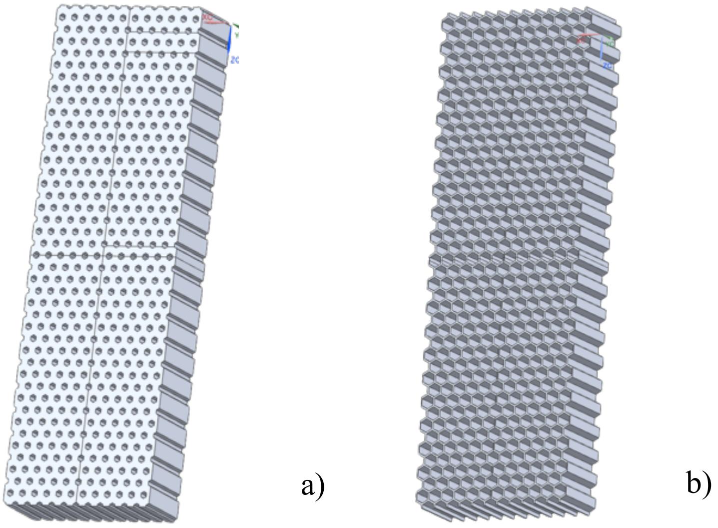
a)
b)

Figure 3.10- Homogeneous structures, a) Upperbound d1.25 and b) Lowerbound d0.25.

3.1.3.5 – Aluminum-A structures

These structures have different dimensions from the others, due to the limitations in the SLM chamber dimensions of 125 mm x 125 mm x 125 mm. The G parameter was set as being 0.080. The dimensions of the aluminum structures are the following: 117 mm x 54 mm x 20 mm (Figure3.11).

Table 3.8 present the values for G parameter and relative density.

Table 3.8 - Aluminum-A Structures G parameter and relative density values for different structures.

Structure	***G parameter***	***Relative density***
Hexagonal	0.080	0.678
Plateau	0.080	0.679
Lotus	0.080	0.708

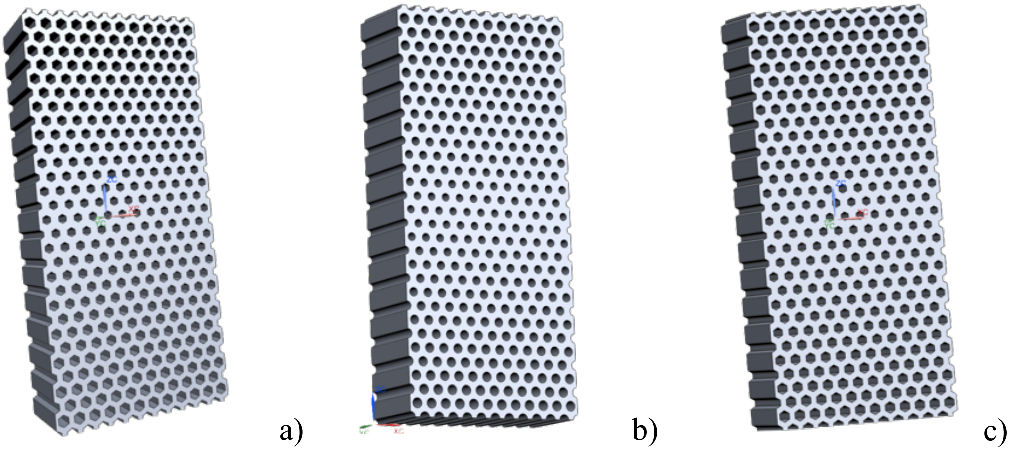
a)
b)
c)

Figure 3.11 - Aluminum-A structures, a) Hexagonal, b) Lotus and c) Plateau.

3.2 – Three-point bending test (3PB)

In this project, the specimens were subjected to three-point bending test. The tests were made in accordance with norm ASTMC393-00 – Standard Test Method for Flexural Properties of Sandwich Constructions [52]. The figure bellow shows a scheme of the three-point bending test where P is the applied load and L_2 is the support span which has a value around 150 mm for all tests performed. Figure 3.12 and 3.13 illustrates the 3PB test.

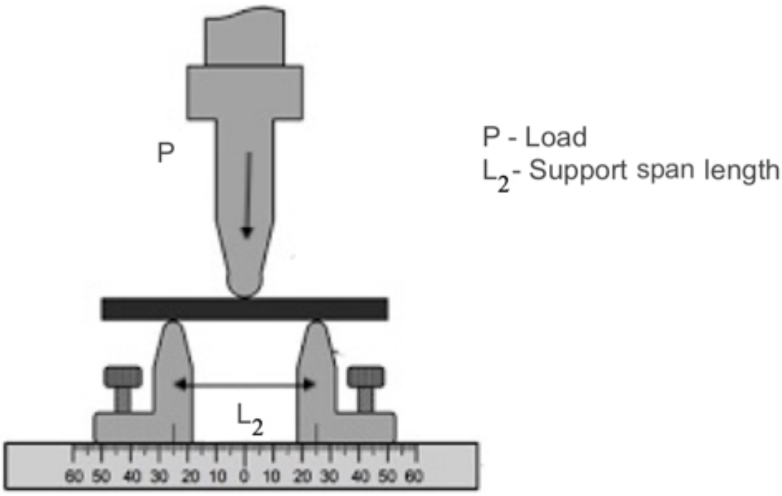

Figure 3.12 - Illustration of the 3PB test [54].

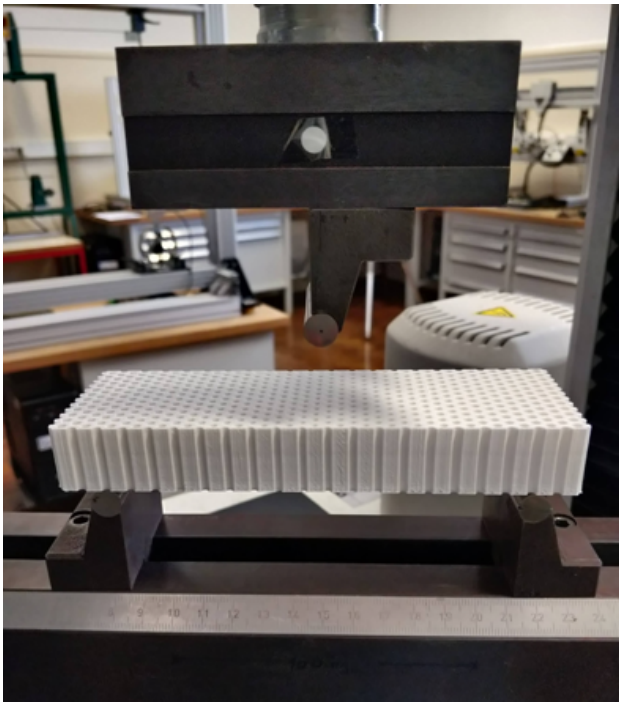

Figure 3.13 - Experimental setup for 3PB test (at IST).

The equipment used to perform these tests was the Instron 3369 (Figure 3.14) device which is a dual column tabletop testing system and has a load cell of 50 kN (Figure 3.15). During all tests, the crosshead speed for the upper roller was defined to be 2.5 mm/min. Also during the tests, the *Bluehill* software was used to get Load vs Displacement curves.

The procedures were the following. First, once the machine is ready, the parameters are given to the software. Despite the dimensions selected while designing the different structures, the dimensions after AM are slightly different in depth from the ones specified in CAD modeling (21 mm instead of 20 mm). After the test, the results are generated to several excel files where information as raw specimen data and bending results are presented. The results from the raw specimen data files are treated and will be presented and discussed in chapter 4.

Figure 3.14 - Instron 3369 testing machine present at the IST Experimental Mechanics Laboratory .

Figure 3.15 - Instron 3369 machine: load cell.

3.3 – Numerical Simulation

As previously mentioned, all the twenty-three structures were made in CAD software Solidworks and were imported to FE software Siemens NX 18 version 1851 as .SLDPRT files. For the analysis process, the software needs three types of files: part, fem and sim. After the sim file is created, a solver module was used [55].

In this section, the mesh refinement convergence study will also be included.

3.3.1 – Part File

The part file is the starting point for each of the analysis performed. The model used can be created in the Siemens NX software or can be imported from a different CAD software, which was the case. After importing the model, since the structures have two symmetric planes (coincident with half-length and half-width), created using *Datum Plane* command, by using the *Split Body* command it was possible to divide the model into four symmetrical pieces. Next, using the *Hide* command only a quarter of the complete model was selected to be shown (Figure 3.16).

Having a quarter of the model is useful in order to simplify and to decrease the computational processing (decreasing memory used and time consumed). The support rollers for the 3PB test were also added using the *Sketch* command and *Extrude* command as well[1].

The last step in the part file is to set planes, using *Datum Plane* command, to divide the model in sections to simplify computing processing once more.

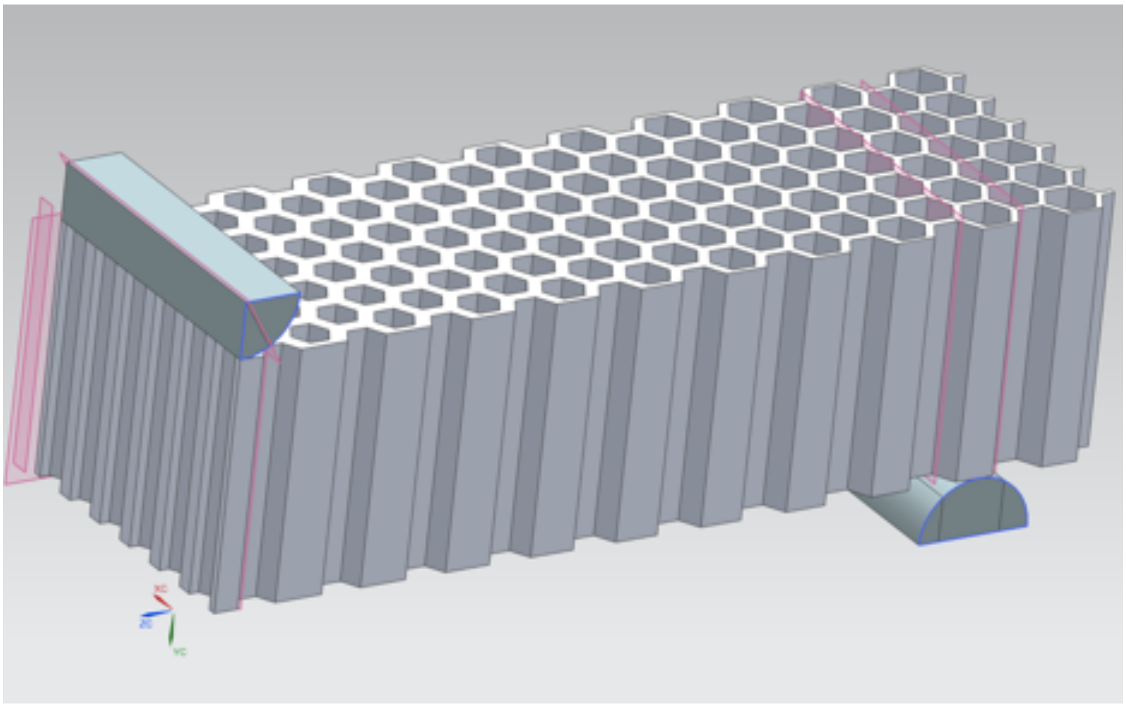

Figure 3.16 - Hexagonal structure part file in Siemens NX software.

---

[1] When using *Extrude*, once the support rollers are only in contact with the structure, Boolean must be set to none.

3.3.2 – Fem File

The fem file is critical file in achieving a good finite elements analysis, and is arguably the most important file of the three. It is where the mesh is created and the materials are assigned to the different parts of the model.

First in the fem file, the *Mesh Mating* command (Figure 3.17) is used to make the mesh mating, so as to align the mesh elements from both side of a plane. Then, the mesh is generated using *3D Swept Mesh* command (Figure 3.18). Here, to simplify computational processing, the use of layers was applied in the main structure meshing and not in the contact rollers.

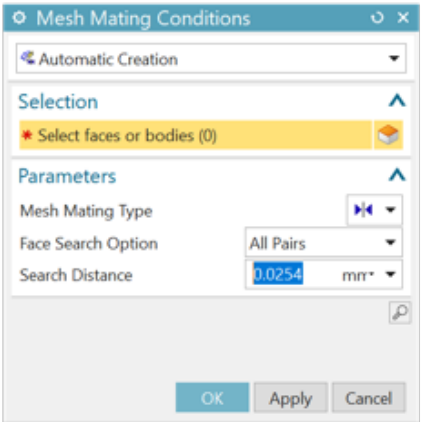

Automatic Creation
Select faces or bodies (0)
Mesh Mating Type
Face Search Option: All Pairs
Search Distance: 0.0254 mm

Figure 3.17 - Mesh Mating conditions window in Siemens NX software.

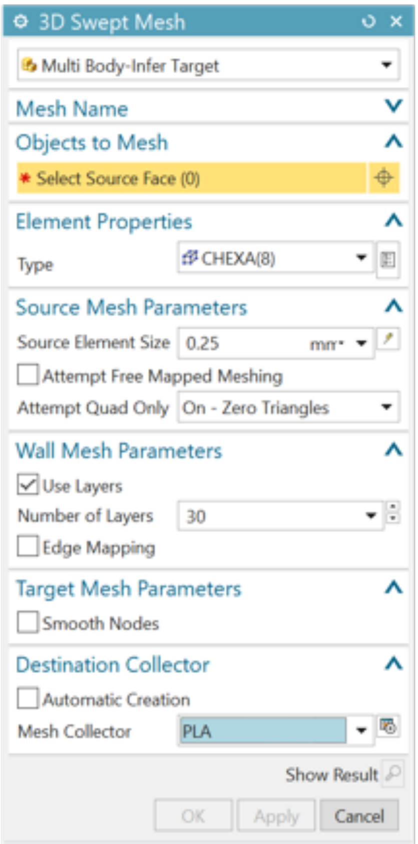

Multi Body-Infer Target
Select Source Face (0)
Type: CHEXA(8)
Source Element Size: 0.25 mm
☐ Attempt Free Mapped Meshing
Attempt Quad Only: On - Zero Triangles
☑ Use Layers
Number of Layers: 30
☐ Edge Mapping
☐ Smooth Nodes
☐ Automatic Creation
Mesh Collector: PLA

Figure 3.18 - 3D Swept Mesh window in Siemens NX software.

The mesh size used, after a mesh refinement convergence test was performed, was 0.25 mm in the contact regions and 0.5 mm in the rest. This refinement convergence test will be explained in section 3.3.5.

The material used for the structure was PLA and for the contact rollers was a steel AISI 1005, which has a much higher Young's Modulus than PLA, once the purpose of the contact rollers is to transmit forces without themselves being deformed.

For the assignment of the materials, a new material had to be created in the software, due to the absence of PLA in its library. The PLA created was in accordance to the data obtained by *Fernandes et al.* [24] (Figure 3.19). The .fem file window can be observed in Figure 3.20.

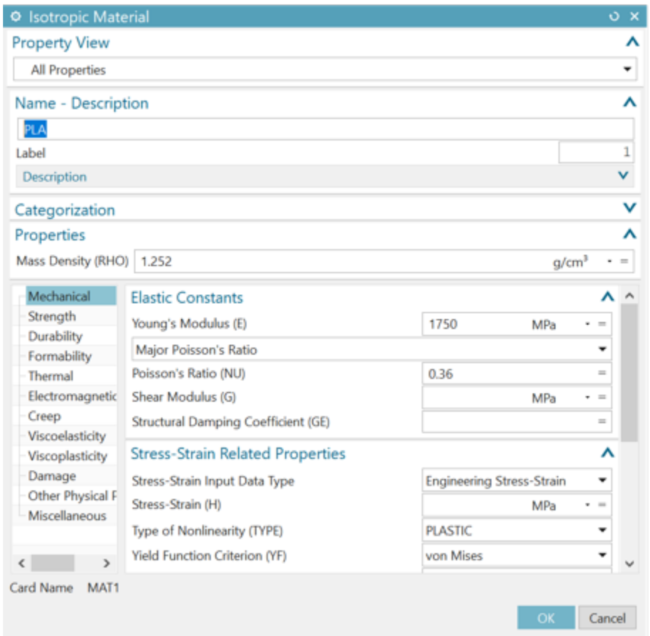

Isotropic Material

Property View: All Properties

Name - Description: PLA

Label: 1

Properties

Mass Density (RHO): 1.252 g/cm³

Elastic Constants

Young's Modulus (E): 1750 MPa

Major Poisson's Ratio

Poisson's Ratio (NU): 0.36

Shear Modulus (G): MPa

Structural Damping Coefficient (GE):

Stress-Strain Related Properties

Stress-Strain Input Data Type: Engineering Stress-Strain

Stress-Strain (H): MPa

Type of Nonlinearity (TYPE): PLASTIC

Yield Function Criterion (YF): von Mises

Card Name: MAT1

Figure 3.19 - Isotropic Material window in Siemens NX software.

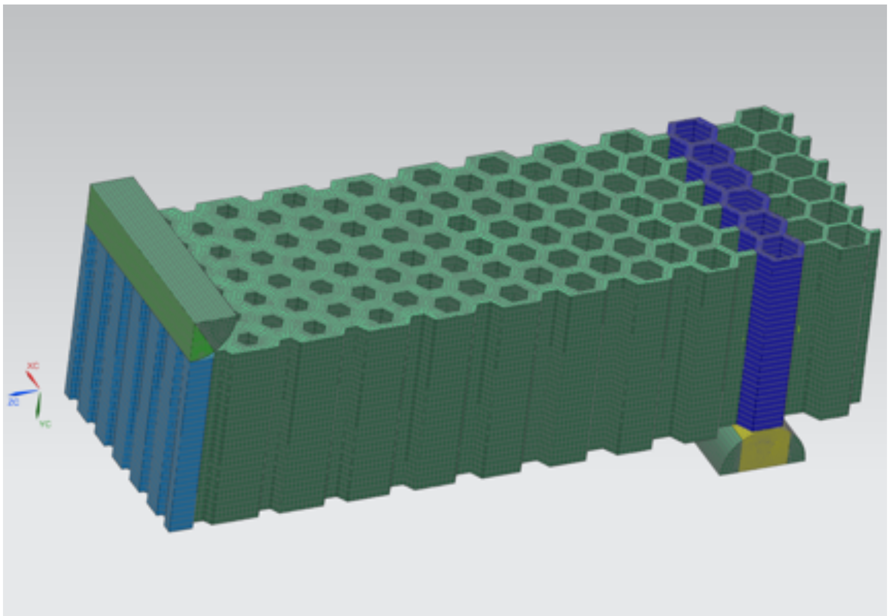

Figure 3.20 - Hexagonal structure fem file in Siemens NX software. Different meshes identified by colors.

3.3.3 – Sim File

This is the last part of the preparation for the FE analysis before running the solver. In this file, the constraints are defined and regions for the contacts are created.

First, starting with creating contact regions, using *Region* command (Figure 3.21), to generate the regions where the contact will be established.

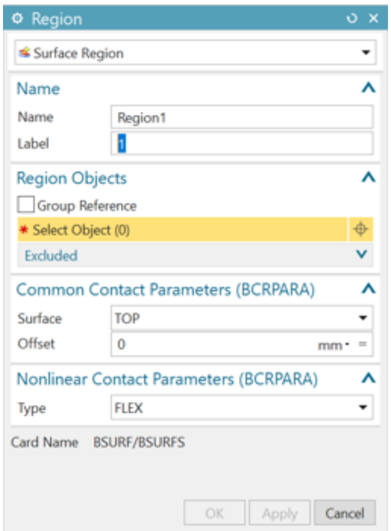

Surface Region

Name: Region1

Label: 1

☐ Group Reference

Select Object (0)

Excluded

Surface: TOP

Offset: 0 mm

Type: FLEX

Card Name: BSURF/BSURFS

Figure 3.21 - Region window Siemens NX software.

After, using *Surface-to-surface contact* command (Figure 3.22) the contact regions representing the contact between the rollers and the structure. The coefficient of static friction must be specified, being for all the tests 0.2. The coefficient of static friction was set in accordance with the values used by Araújo et al. [4,6]. Also, the initial penetrations were set to zero, to simplify the computational processing time. This assumption is due to the large difference between Young's Modulus.

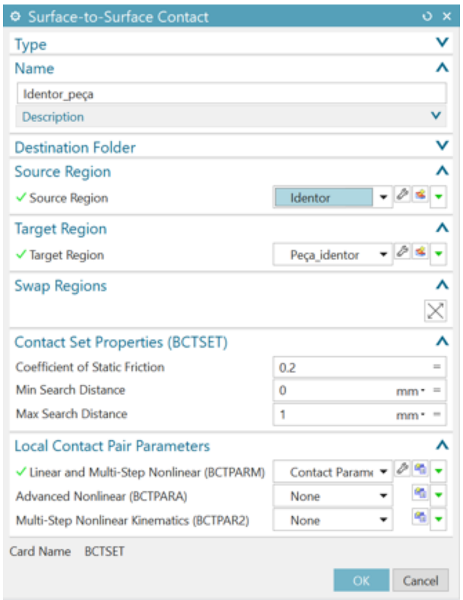

Name: Identor_peça

✓ Source Region: Identor

✓ Target Region: Peça_identor

Coefficient of Static Friction: 0.2

Min Search Distance: 0 mm

Max Search Distance: 1 mm

✓ Linear and Multi-Step Nonlinear (BCTPARM): Contact Param

Advanced Nonlinear (BCTPARA): None

Multi-Step Nonlinear Kinematics (BCTPAR2): None

Card Name: BCTSET

Figure 3.22 - Surface-to-Surface Contact window in Siemens NX software.

Then, two more constraints were applied using the following commands: *enforcement displacement constrain (Figure 3.23 a)) and* fixed *constraint (Figure 3.23 b)).* The first one was applied to the bottom support (roller) and the second was applied to the top roller. The enforcement constraint was set from 0 up to 2.5 mm with 0.5 mm increments.

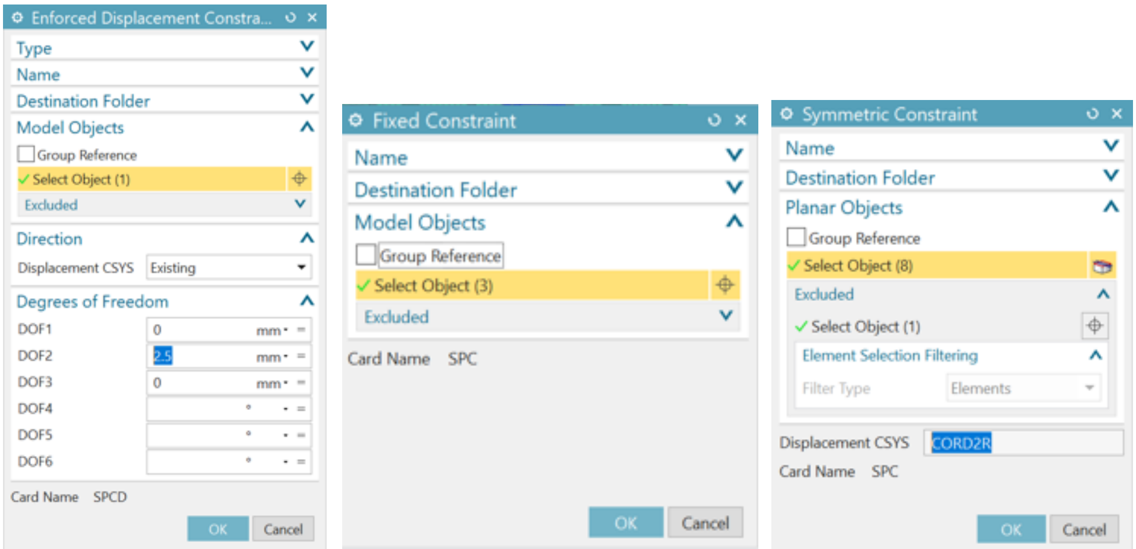

☐ Group Reference
✓ Select Object (1)
Excluded
Displacement CSYS Existing
DOF1 0 mm
DOF2 2.5 mm
DOF3 0 mm
DOF4
DOF5
DOF6
Card Name SPCD

☐ Group Reference
✓ Select Object (3)
Excluded
Card Name SPC

☐ Group Reference
✓ Select Object (8)
Excluded
✓ Select Object (1)
Filter Type Elements
Displacement CSYS CORD2R
Card Name SPC

a) b) c)

Figure 3.23 - Different constraints that are applied to the structure: a) Enforced Displacement Constraint, b) Fixed Constraint, c) Symmetric Constraint.

The last constraint applied was the symmetry using the *symmetrical constraint* command (Figure 3.23 c)). It is necessary due to the two-symmetric planes, and because only a quarter of the whole structure it's being used (Figure 3.24). The .sim file window is represented in Figure 3.26.

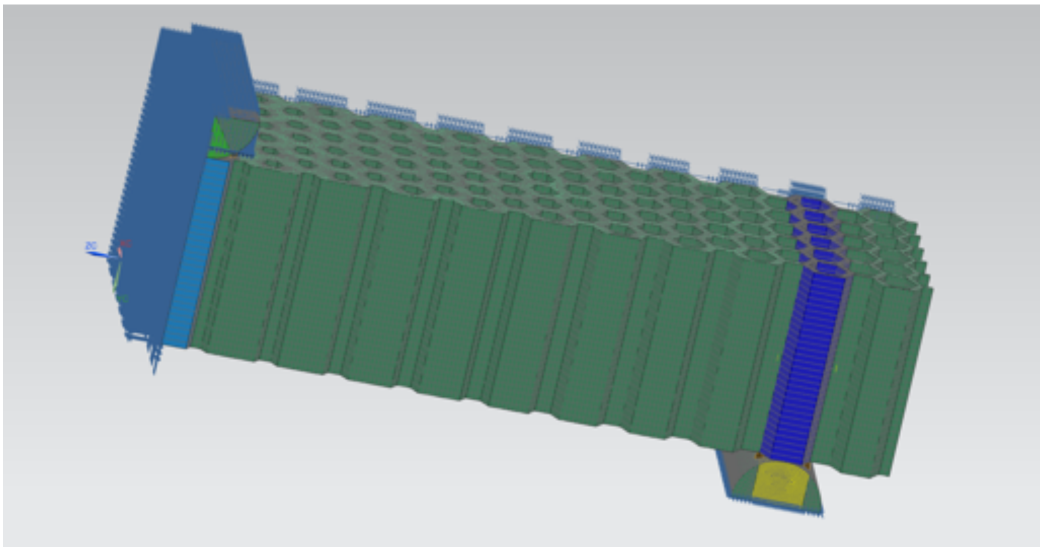

Figure 3.24 - Hexagonal structure sim file in Siemens NX software. Surface-to-surface contacts in yellow and constraints in blue.

3.3.4 – Solution Solver

Once the sim file is completed with the constraints, a solver code must be run to obtain the results. The most important part is to define the type of solution to use according to the analysis required. Choosing it according to the real problem is key. For all the tests, it was used a linear static solution – *SOL 101 Linear Statics – Global Constrains* (Figure 3.25 and 3.26). The linear type was selected instead of the non-linear due to computational space and processing limitations.

It is important to select the output parameters that are needed. In this case, for all tests the output requests were displacement, elemental and nodal stress, contact force, reaction force and strain. Once the output results are obtained, they will give information for the von Mises stress, force applied in the roller, absorbed energy, rigidity constant K and Load vs Displacement curves for every single analyzed topology. These results will be presented and discussed in the next chapter.

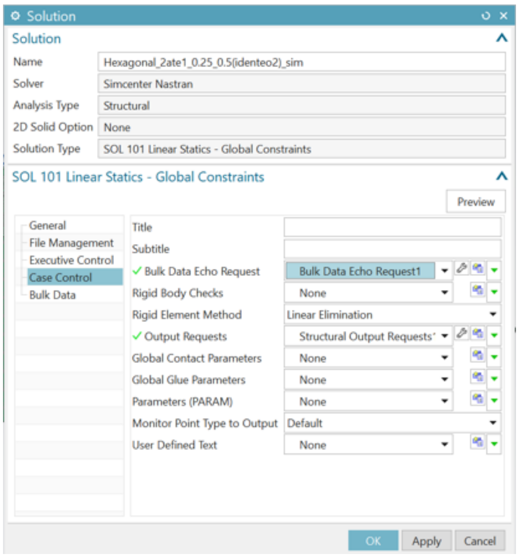

Name: Hexagonal_2ate1_0.25_0.5(identeo2)_sim
Solver: Simcenter Nastran
Analysis Type: Structural
2D Solid Option: None
Solution Type: SOL 101 Linear Statics - Global Constraints

✓ Bulk Data Echo Request: Bulk Data Echo Request1
Rigid Body Checks: None
Rigid Element Method: Linear Elimination
✓ Output Requests: Structural Output Requests'
Global Contact Parameters: None
Global Glue Parameters: None
Parameters (PARAM): None
Monitor Point Type to Output: Default
User Defined Text: None

Figure 3.25 - Solution window Siemens NX software.

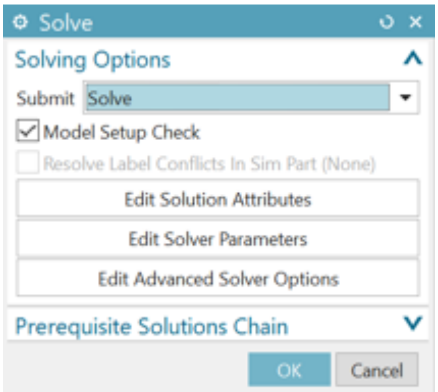

Submit: Solve
☑ Model Setup Check
☐ Resolve Label Conflicts In Sim Part (None)

Figure 3.26 - Solve window Siemens NX software.

After setting the output requests and the solution type, the analysis must be run. For that, the *solve* command must be used.

3.3.5 – Mesh refinement

In order to get good analysis results, a very important aspect is the quality of the mesh used. Because of that, a mesh refinement convergence study was performed. The convergence criterion used was defined as less than 5% changes in the values of the maximum von Mises stress. Then the mesh prior to the last was used, in order to reduce the computational processing time and memory. The smaller the mesh elements sizes, the better is the matching to the real behavior of the structure. On the other hand, the bigger the elements, less number of nodes, the mesh will become less dense and the results will be less precise. A balance between number of nodes and computational processing time must be made. The mesh refinement convergence test is necessary to make the analysis more efficient. All the convergence tests started with elements size being: 0.6 mm in the contact regions and 1.0 mm in the rest of the geometry. The convergence test was conducted using the thinner structure, being the one where the variation would be larger.

The first test was made with the maximum value for nodal von Mises stress. The data is presented in the following plot (Figure 3.27) and table 3.9.

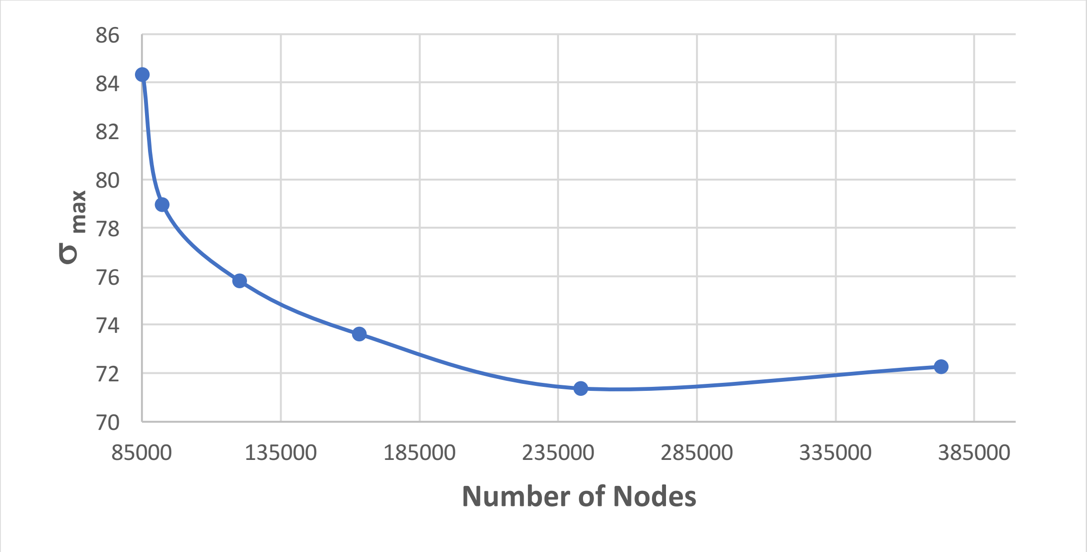

Figure 3.27 - Maximum nodal von Mises stress vs number of nodes plot.

Table 3.9 - List of values of maximum von Mises nodal stress, number of nodes and relative variation for different mesh element sizes.

Mesh Elements Size (mm)	***Maximum von Mises nodal stress (MPa)***	***Number of Nodes***	***Relative Variation (%)***
0.6/1	84.3248	85236	-
0.5/1	78.9614	92392	-6.36%
0.4/0.8	75.7984	120279	-4.01%
0.3/0.8	73.6101	163400	-2.89%
0.25/0.5	71.3699	243350	-3.04%
0.15/0.5	72.2661	373275	1.26%

The second convergence test was made with von Mises stress values for a specific point. This point was used to measure the stress value for each mesh configuration. The point was selected to be in the fourth element below the contact zone between the roller and the specimen. The results are shown in Figure 3.28 and table 3.10.

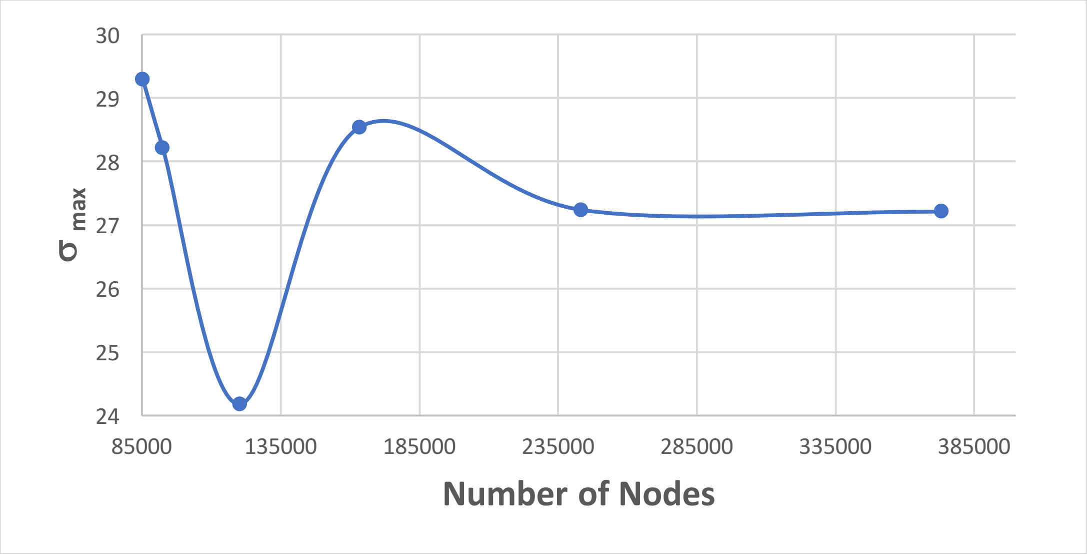

Figure 3.28 - Local von Mises nodal stress vs number of nodes graph.

Table 3.10 - List of values of local von Mises nodal stress, number of nodes and relative variation for different mesh element sizes.

Mesh Elements Size (mm)	***Local von Mises Nodal Stress (MPa)***	***Number of Nodes***	***Relative Variation (%)***
0.6/1	29.2943	85236	-
0.5/1	28.2182	92392	-3.67%
0.4/0.8	24.1823	120279	-14.30%
0.3/0.8	28.5434	163400	18.03%
0.25/0.5	27.2419	243350	-4.56%
0.15/0.5	27.2142	373275	-0.10%

The last test was made using the average value of von Mises stress. This average value was obtained by selecting the whole top roller contact region in the structure. The entire surface elements of the mesh gave an average value. The Figure 3.29 and table 3.11 presents the values.

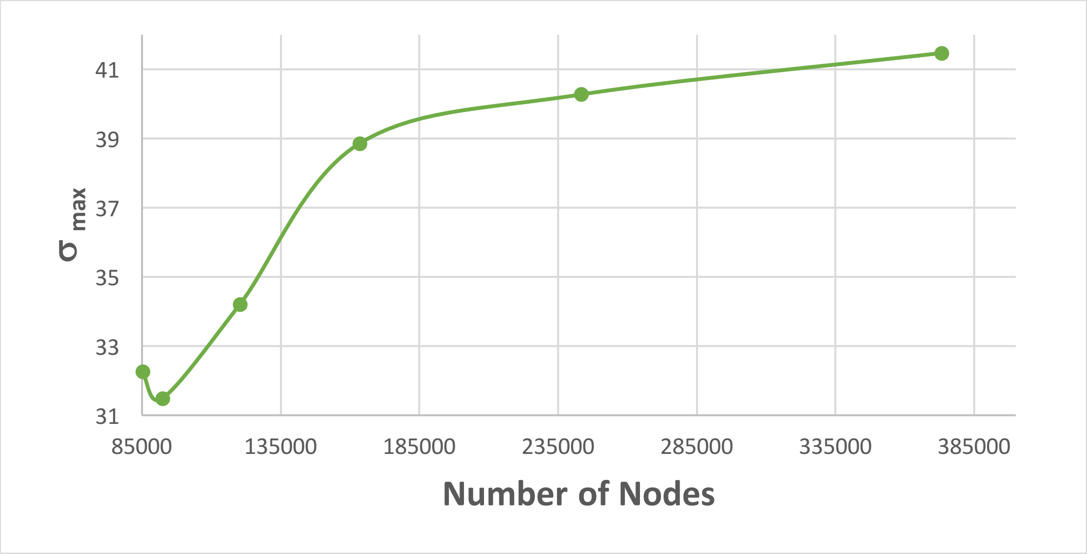

Figure 3.29 - Average von Mises stress vs number of nodes graph.

Table 3.11 - List of values of average von Mises stress, number of nodes and relative variation for different mesh element sizes.

Mesh Elements Size (mm)	***Average von Mises Stress (MPa)***	***Number of Nodes***	***Relative Variation (%)***
0.6/1	32.2595	85236	-
0.5/1	31.4914	92392	-2.38%
0.4/0.8	34.1982	120279	8.60%
0.3/0.8	38.8506	163400	13.60%
0.25/0.5	40.27	243350	3.65%
0.15/0.5	41.4676	373275	2.97%

As seen in the tables showed above, the mesh size used in the simulations was 0.25 mm for the contact regions and 0.5 mm for the rest of the geometry. Although the variation between the 0.3/ 0.8 is not larger than 5 % in neither case, the size chosen was 0.25 mm and 0.5 mm.

3.4 – Additive Manufacturing

As mentioned before, all specimens were created in SolidWorks 2018 Student Edition *software*, and then were converted to stereolithographic files (.STL). Once the files were converted, they were imported to the CURA software and then sent to the respective machine.

3.4.1 – PLA

The PLA specimens were manufactured through FFF method. An Ultimaker 3 printer (Figure 3.30 a)) was used. The most important parameters are the following: infill, layer thickness and temperatures of both the PLA filament and the printing bed (Figure 3.30 c)). All the specimens were manufactured by extruder 1 with print core AA0.4 (Figure 3.30 b)) and 100% infill with closed chamber. As denoted by the print core, the layer thickness used was 0.4 mm.

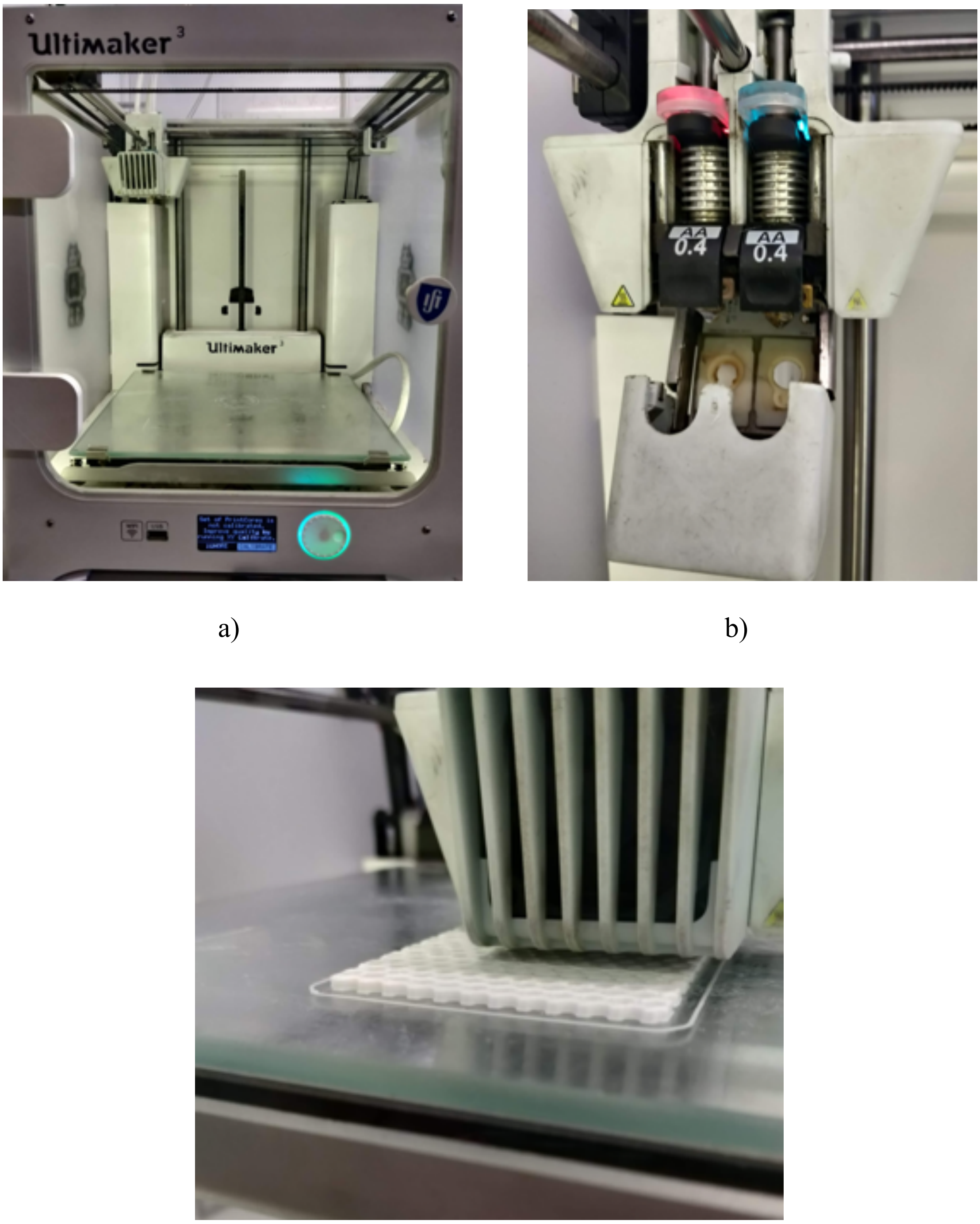

a) b)

c)

Figure 3.30 - a) Ultimaker 3 printing machine, b) printing cores AA 0.4, c) print of the first layers of a specimen.

The first parameter set of prints was conducted using the following parameters of Table 3.12.

Table 3.12 - List of the first parameter set-up tested.

Parameter	***Value***
Infill speed	50 (mm/s)
Outer Wall Speed	50 (mm/s)
Travel Speed	250 (mm/s)
Initial Layer Speed	26 (mm/s)
Extrusion Temperature	205 ºC
Built Plate Temperature	70 ºC
Infill Overlap	0 %

The result of the initial layers was not the expected, being noticeable the existence of small gaps between consecutive layers. This defect can be due to the CURA's *software* g code generating process that due to density gradient can have some issues.

The second set of parameters was performed changing the infill overlap parameter. It was set to 10%. All the remaining parameters were maintained (Table 3.13).

Table 3.13 - List of the second parameter set-up tested.

Parameter	***Value***
Infill Speed	50 (mm/s)
Outer Wall Speed	50 (mm/s)
Travel Speed	250 (mm/s)
Initial Layer Speed	26 (mm/s)
Extrusion Temperature	205 ºC
Built Plate Temperature	70 ºC
Infill Overlap	10 %

The results were considerably better than in the first test. The comparison between both tests is showed in the following image. Can be observed, the sample with infill overlap of 10% has a better manufacturing quality compared with the one without infill overlap. This is observed in Figure 3.31.

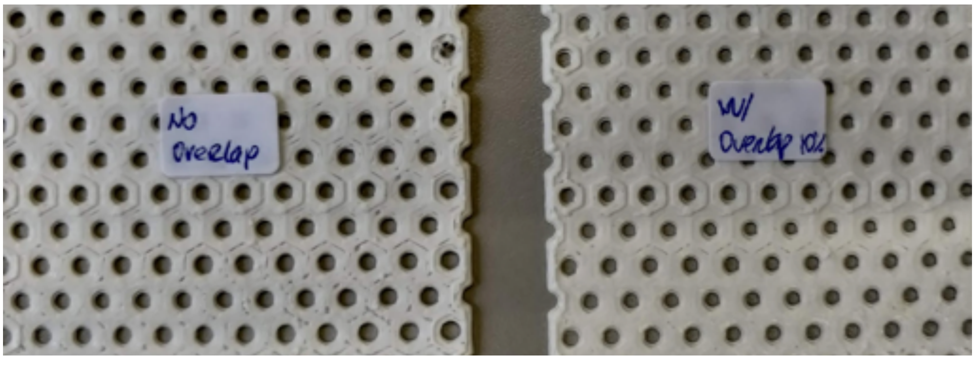

Figure 3.31 - Comparison between some layers printed with no infill overlap and some printed with infill overlap of 10%.

The third and last set of tests was conducted changing only the printing speed, from 50 mm/s to 90 mm/s (Table 3.14). The results were similar to the second test, but the manufacturing time has decreased in about 15%. The printing times vary from 16 h to 39 h depending on the topology of the model.

Table 3.14 - Third and the one used parameter set-up.

Parameter	Value
Infill Speed	90 (mm/s)
Outer Wall Speed	50 (mm/s)
Travel Speed	250 (mm/s)
Initial Layer Speed	26 (mm/s)
Extrusion Temperature	205 ºC
Built Plate Temperature	70 ºC
Infill Overlap	10 %

Some PLA specimens are shown in Figure 3.34. The dimensions of the AM structures have a small variation when compared to the intended dimensions (CAD dimensions). The height has 21 mm in the additively manufactured structure instead of 20 mm. It represents a dimensional error of 5 %. This error is negligible when analyzing both length and width.

In the final structures, there were some manufacturing errors due to the existent density gradient. Those issues are not present when observing the surface of the Upperbound and Lowerbound structures – both have no density gradients. Due to the density gradient, the machines g code has some difficulties in achieving the required arrangement. The use of the 10% infill overlap made it better.

The manufacturing times, the weights and the amount of PLA filament used for each specimen group are listed in the table 3.15.

Table 3.15 - List of times, weights and filament length for each type of specimen.

Specimen	***Time (h)***	***Weight (g)***	***Filament Length (m)***
Hexagonal	34.5	173	21.82
Plateau	32	170	21.51
Lotus	25	174	22.06
Upperbound	34.5	208	26.25
Lowerbound	26.2	143	18.02

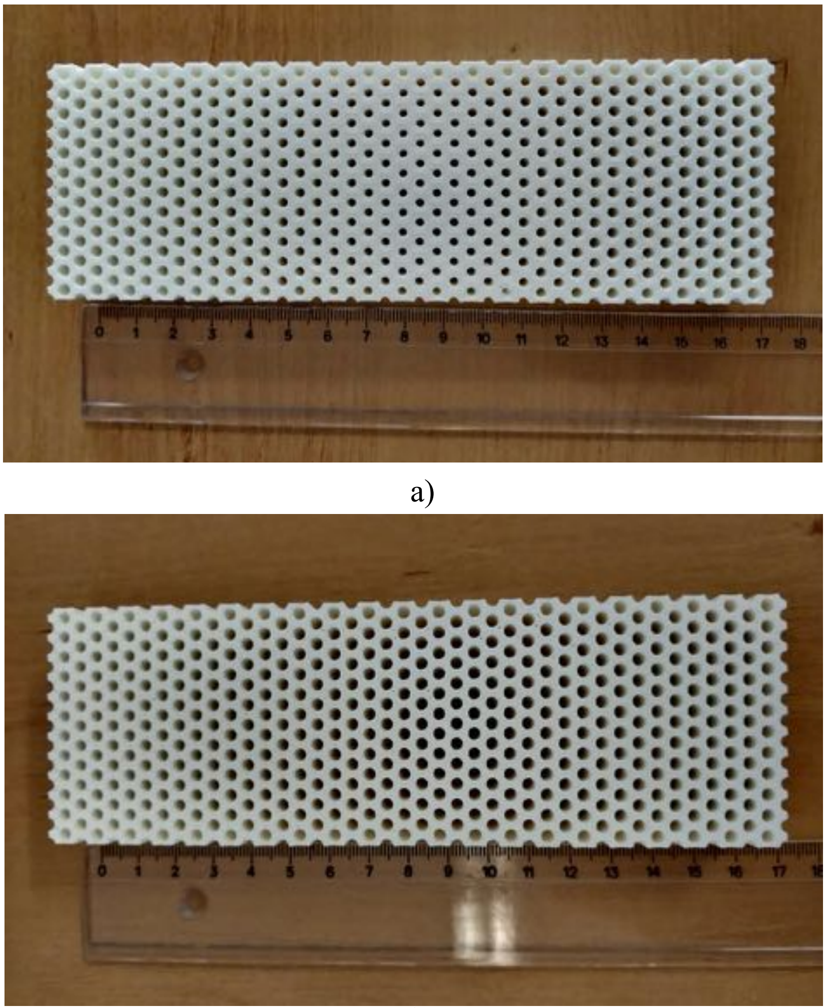

a)

b)

Figure 3.32 - Complete printed specimens: a) Plateau structure, b) Upperbound structure.

Figure 3.32 shows the printed parts for the Plateau d_{min} 0.80 d_{max} 1.20 and the Upperbound structure with d 0.80.

3.4.2 – Aluminum-A

It was not possible to obtain samples from Aluminum-A, as the device was not available, although, the Aluminum-A specimens were supposed to be manufactured through SLM method. They would be manufactured at École Nationale Supérieure des Mines d'Albi-Carmaux, Jarland Campus, France. The machine used would the SLM Solutions 125HL. The machine has a manufacturing chamber with dimensions of 125 mm x 125 mm x 125 mm. It has a maximum processing rate of 25 cm^3/h. The 3D optical system has a single 400 W IPG fiber laser with a diameter between 70 and 100 μm and a maximum speed of 10 m/s. Each material layer has a thickness from 20 to 75 μm and 1 μm increments can be made. Argon is the inert gas used in this machine with an average consumption of 2L/min.

The AlSi7Mg0.6 aluminum powder used has the composition presented in Table 3.16. It corresponds to a cast alloy, due to the fact it is the only type of Al alloy that can be printed successfully by SLM nowadays.

Table 3.16 - Aluminum-A (AlSi7Mg0.6) powder used for SLM printings.

Element	***Minimum (wt%)***	***Actual (wt%)***	***Maximum (wt%)***
Al	Balance	Balance	Balance
Cu	-	<0.01	0.05
Fe	-	0.13	0.19
Mg	0.45	0.47	0.70
Mn	-	<0.01	0.10
Si	6.50	6.65	7.50
Ti	-	0.01	0.25
Zn	-	<0.01	0.07
Others each	-	0.03	0.03
Others total	-	0.10	0.10

Chapter 4

Results and Discussion

In this chapter, the results obtained from both numerical (FEA) and experimental tests will be presented and evaluated. The correlation between these two methods will be also discussed.

The results will be divided by materials, PLA and Aluminum-A, by G parameters and by angle of rotation. For Aluminum-A, only finite element analysis is presented.

4.1 – Preliminary notes

In this section, some comments are made about the mechanical properties obtained from the additive manufacturing PLA structures and then, they are compared to the same properties obtained from 3PB experimental tests. For Aluminum structures, only FEA results will be evaluated.

4.2 – Numerical simulation results

All numerical simulation results, both for PLA and Aluminum, are for a quarter of the geometry only.

4.2.1 – PLA numerical results

The following results show the values of relative density, G parameters and the values of von Mises stress, the slope of the linear region Load vs Displacement curve, K, and the absorbed energy, $E_{a.}$ The von Mises stress included in the tables is the maximum von Mises stress, σ_{max}. The parameters K and E_a are obtained respectively from the initial slope of the Load vs Displacement curve and from the region until 2.5 mm displacement, for numerical and experimental comparison. The parameters von Mises stress, slope of the linear region and the absorbed energy were normalized with respect to the relative density. The data is divided in tables by G parameter and angle of rotation.

All the parameters were obtained using the Siemens NX *software,* where the respective *output requests* were selected and analyzed. Tables 4.1 until 4.3 present the values for 0-degree angle of rotation structures. Each table represents a set of structures with the same G parameter (Hexagonal core, Plateau core and Lotus core structures) as well as the respective Lowerbound and Upperbound. Table 4.4 present the results for the 90-degree angle of rotation structures.

Numerically, for a G parameter of 0.212 (Table 4.1), once the values are normalized, it is possible to verify that the core structure design with higher energy absorption and higher Load vs Displacement slope curve is Lotus. Lotus, is followed by Plateau and then Hexagonal as the structures that attain the highest values of specific K and Ea, although this tendency is more clearly marked for the steeper gradients. Third highest value was obtained with the Upperbound structure. Concerning the von Mises stress, the situation is less well defined, but the Lowerbound structures seem to have a small advantage.

Table 4.1 - Values of relative density, G parameter and values of stress, initial stiffness, Absorbed Energy normalized with relative density for different structures (G=0.212).

Geometry	$\bar{\rho}$	$\bar{\sigma}_y/\bar{\rho}$ (MPa)	$K/\bar{\rho}$ (N/mm)	$E_a/\bar{\rho}$ (N.mm)	G parameter
Lowerbound d0.25	0.210	339.112	38.594	109.152	-
Hexagonal d0.25-1.25	0.552	154.572	271.092	315.556	0.212
Plateau d0.25-1.25	0.554	151.098	277.845	379.410	0.212
Lotus d0.25-1.25	0.589	143.773	292.249	460.269	0.212
Upperbound d1.25	0.803	133.833	258.205	323.194	-

For G parameter of 0.105 (Table 4.2), it is possible to verify that the core structure design with higher values, for both absorbed energy and Load vs Displacement slope curve, is Lotus. The second highest values, both for curve slope and absorbed energy were obtained with the Plateau structure. The third highest were obtained with the Hexagonal structure. Once again, being the same structure, the one with higher von Mises value is the Lowerbound.

Table 4.2 - Values of relative density, G parameter and values of stress, initial stiffness, Absorbed Energy normalized with relative density for different structures (G=0.105).

Geometry	$\bar{\rho}$	$\bar{\sigma}_y/\bar{\rho}$ (MPa)	$K/\bar{\rho}$ (N/mm)	$E_a/\bar{\rho}$ (N.mm)	G parameter
Lowerbound d0.25	0.210	339.112	38.594	109.152	-
Hexagonal d0.25-0.75	0.399	191.374	167.806	310.075	0.105
Plateau d0.25-0.75	0.401	177,679	182.010	377.595	0.105
Lotus d0.25-0.75	0.455	175.453	236.466	396.762	0.105

For G parameter of 0.091 (Table 4.3), it is possible to observe that the core structure design with better performance, higher value for absorbed energy and Load vs Displacement slope curve, is Lotus. The second highest value for slope curve was obtained with the Plateau structure and the second highest value of absorbed energy was obtained with the Upperbound structure. The third highest value for slope curve was obtained with the Upperbound structure and the third highest value of absorbed energy was obtained with the Hexagonal structure. The core structure design with higher value for von Mises stress is the Plateau.

Table 4.3 - Values of relative density, G parameter and values of stress, initial stiffness, Absorbed Energy normalized with relative density for different structures (G=0.091).

Geometry	$\bar{\rho}$	$\bar{\sigma}_y/\bar{\rho}$ (MPa)	$K/\bar{\rho}$ (N/mm)	$E_a/\bar{\rho}$ (N.mm)	G parameter
Lowerbound d 0.80	0.585	137.520	179.274	285.883	-
Hexagonal d0.80-1.20	0.684	151.916	248.774	303.084	0.091
Plateau d0.80-1.20	0.685	155.798	254.187	299.614	0.091
Lotus d0.80-1.20	0.713	129.294	271.976	412.422	0.091
Upperbound d1.20	0.782	147.576	250.405	303.606	-

For the structures with 0-degree angle of rotation, the following plots in Figure 4.1 summarize the values, and allow a better comparison between the three different core designs. The first comparison plot (Figure 4.1 a)), compares the von Mises stress between the different structures and sums the information in the tables above. The second plot (Figure 4.1 b)), compares the values of slope of the linear region Load vs Displacement curve, and the third one (Figure 4.1 c)), compares the values of the absorbed energy.

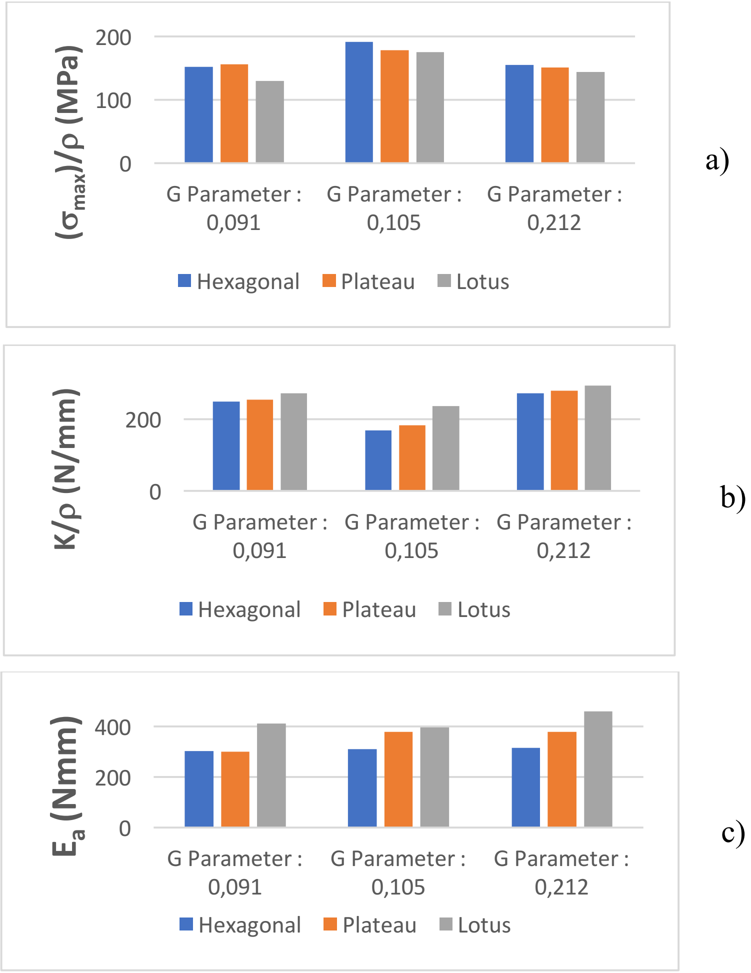

Figure 4.1 - Comparison plots between Hexagonal, Plateau and Lotus core: a) von Mises stress normalized by relative density, b) Slope of the linear region, c) Absorbed energy.

In the numerical part, the best results for most of the 0-degree angle of rotation structures were obtained with the Lotus design. This can be seen from the aforementioned plots, where the specimens with Lotus core design achieve better results overall. The explanation offered for the higher von Mises values observed with the Hexagonal structure lies in the presence of sharp edges acting as stress concentrators. On the other hand, the small radius of the Plateau design also induces some stress concentration. From this standpoint, the most advantageous structure is the Lotus.

The following plots from *Siemens NX* show the numerical results for the 3PB loading, featuring the displacement of the part and the roller, the von Mises stress and the rollers reaction force in z-axis. Only the printed models are showed, and only a quarter of the geometry was simulated because of the symmetry conditions; the others are showed in Appendix B. Figure 4.2 exhibits the results for FEA of a Hexagonal structure (G = 0.091) under 3PB loading showing: displacement of the model and rollers, element von Mises stress in the skins and rollers reaction force in z-axis. The maximum von Mises stress was in the fixed support contact area.

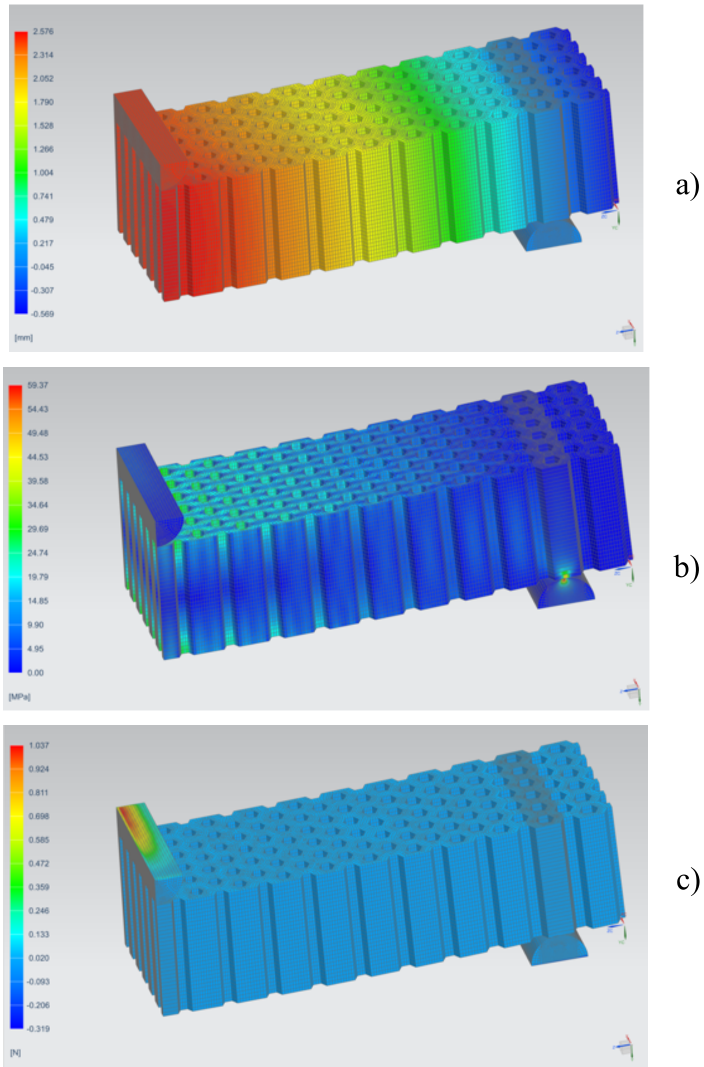

Figure 4.2 - FEA of a Hexagonal structure under 3PB loading, one quarter of the geometry showed: a) displacement of the model and rollers, b) elemental von Mises stress in the skins and c) rollers reaction force in z-axis.

Figure 4.3 exhibits the results for FEA of a Plateau structure (G = 0.091) under 3PB loading showing: displacement of the model and rollers, elemental von Mises stress in the skins and rollers reaction force in z-axis. The maximum von Mises stress was in the moving indenter contact area.

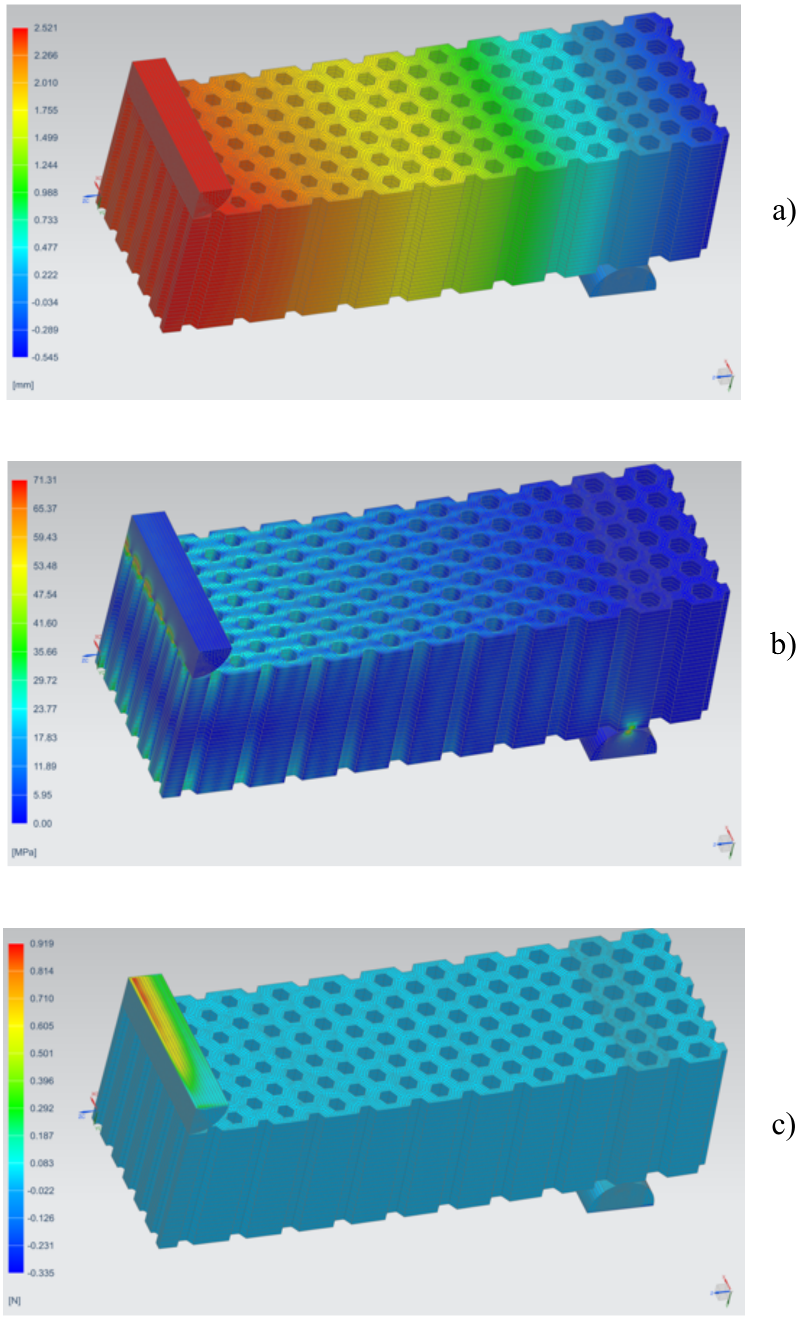

Figure 4.3 - FEA of a Plateau structure under 3PB loading, one quarter of the geometry showed: a) displacement of the model and rollers, b) elemental von Mises stress in the skins and c) rollers reaction force in z-axis.

Figure 4.4 exhibits the results for FEA of a Lotus structure (G = 0.091) under 3PB loading showing: displacement of the model and rollers, elemental von Mises stress in the skins and rollers reaction force in z-axis. The maximum von Mises stress was in the moving indenter contact area.

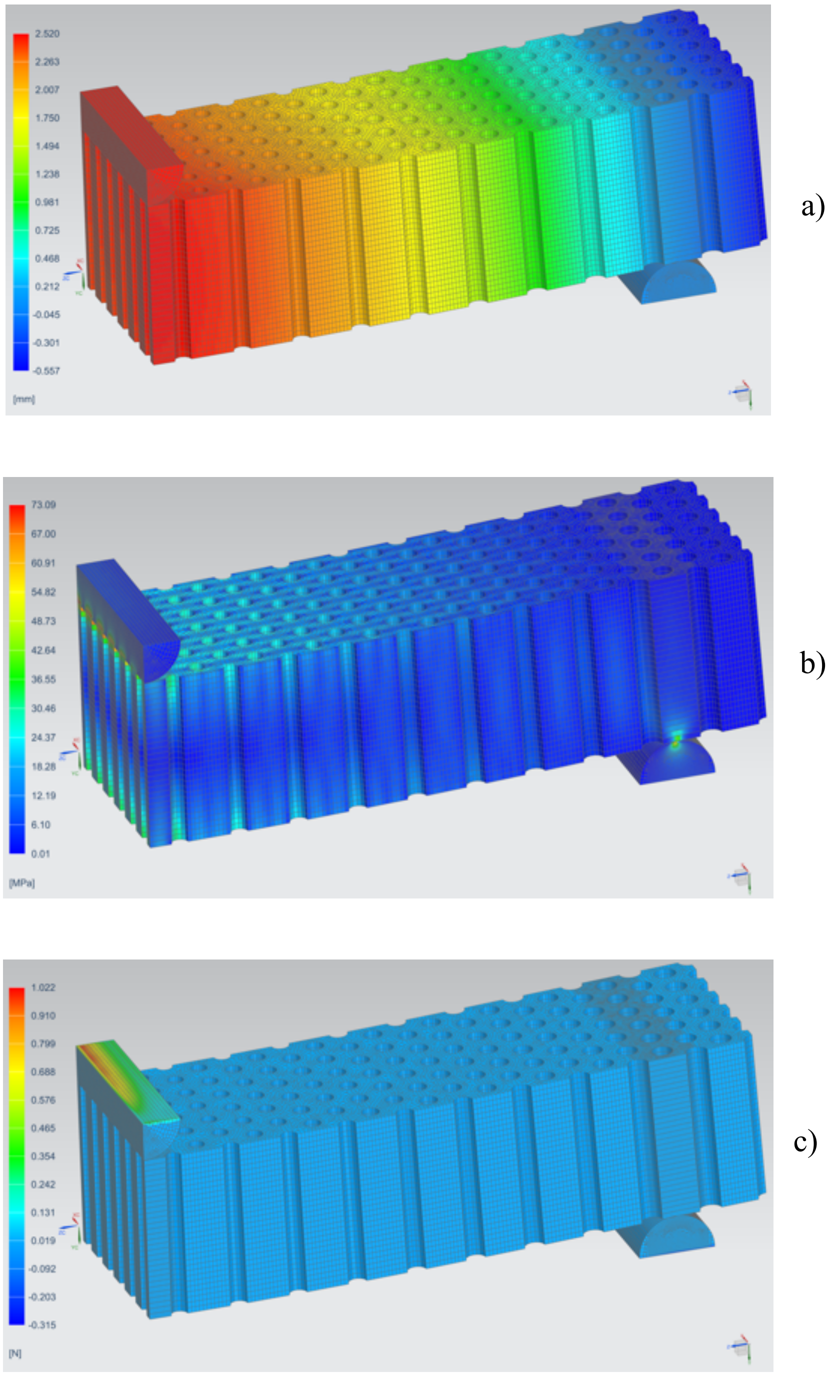

Figure 4.4 - FEA of a Lotus structure under 3PB loading, one quarter of the geometry showed: a) displacement of the model and rollers, b) elemental von Mises stress in the skins and c) rollers reaction force in z-axis.

Figure 4.5 exhibits the results for FEA of a Upperbound structure (G = 0.091) under 3PB loading showing: displacement of the model and rollers, elemental von Mises stress in the skins and rollers reaction force in z-axis. The maximum von Mises stress was in the moving indenter contact area.

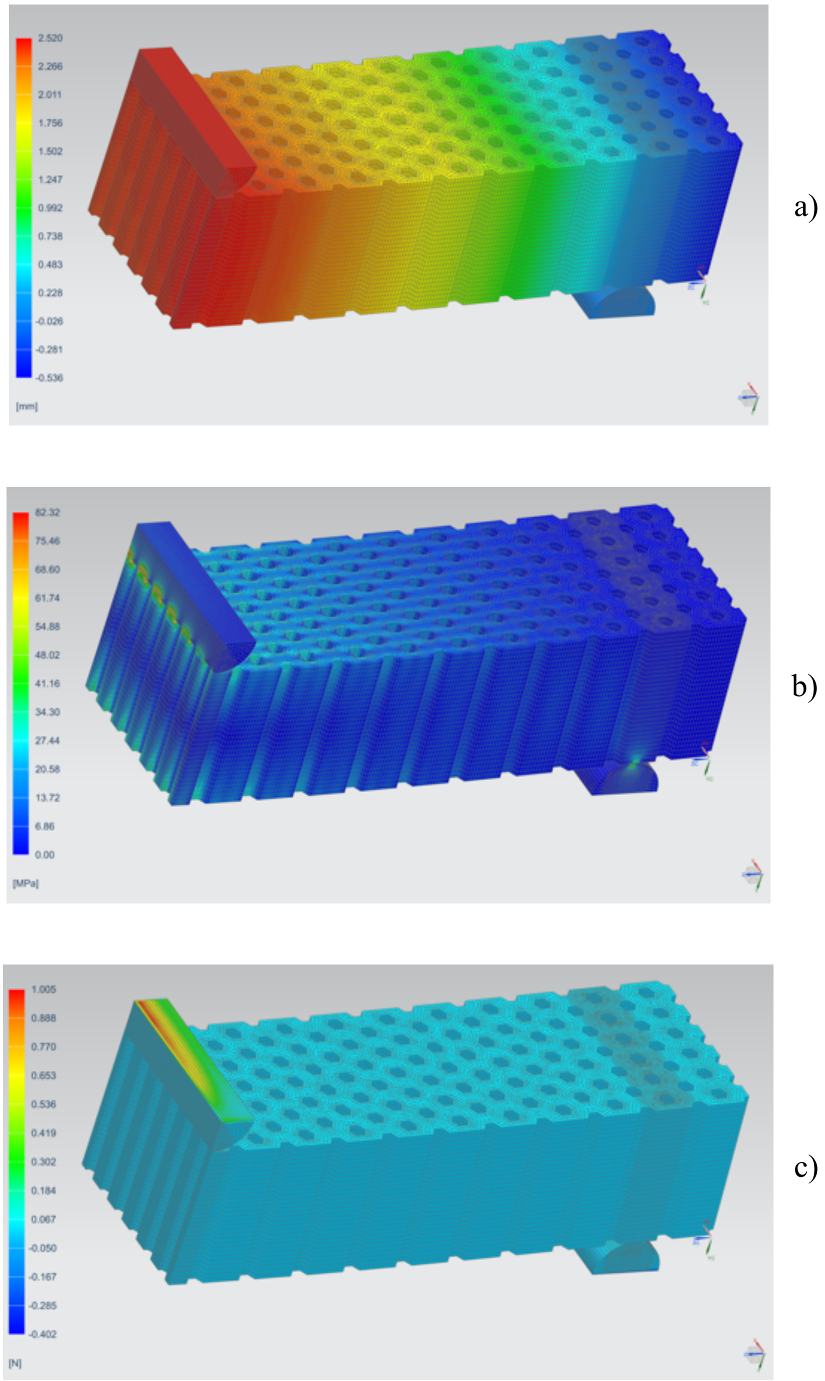

Figure 4.5 - FEA of Upperbound structure under 3PB loading, one quarter of the geometry showed: a) displacement of the model and rollers, b) elemental von Mises stress in the skins and c) rollers reaction force in z-axis.

Figure 0.6 exhibits the results for FEA of a Lowerbound (G= 0.091) structure under 3PB loading, showing: displacement of the model and rollers, elemental von Mises stress in the skins and rollers reaction force in z-axis. The maximum von Mises stress was in the moving indenter contact area.

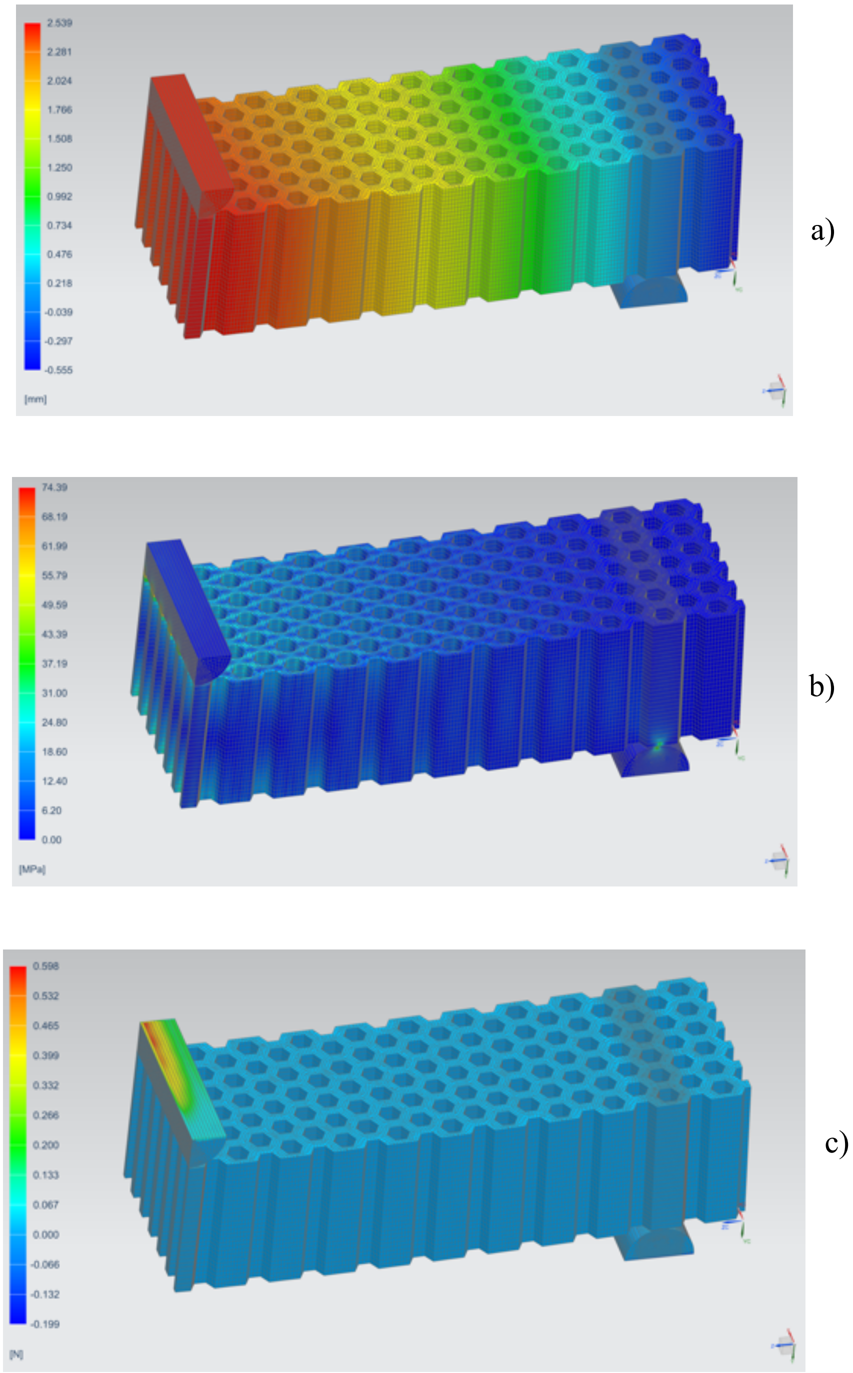

Figure 4.6 - FEA of Lowerbound structure under 3PB loading, one quarter of the geometry showed: a) displacement of the model and rollers, b) elemental von Mises stress in the skins and c) rollers reaction force in z-axis.

For the 90-degree structures Table 4.4 presents the FEA results. The numerical results show that the higher results for von Mises stress was obtained by Plateau structure, being the second highest results achieved with Hexagonal and then followed by the Lowerbound structure. For K, the highest value was obtained by the Hexagonal structure, followed by the Lotus and then the Plateau structure. When analyzing the E_a, it is observable that the structure that performed better was the Plateau structure, followed by the Lotus and then, the third best result was obtained by the Hexagonal structure.

Table 4.4 –Values of relative density, G parameter and values of stress, initial stiffness, Absorbed Energy normalized with relative density for different structures (G=0.677).

Geometry	$\bar{\rho}$	$\bar{\sigma}_y/\bar{\rho}$ *(MPa)*	$K/\bar{\rho}$ *(N/mm)*	$E_a/\bar{\rho}$ *(N.MM)*	*G parameter*
Lowerbound_90 d0.74	0.431	140.11	127.23	298.43	-
Hexagonal_90 d0.74-d1.48	0.678	148.49	306.11	347.48	0.677
Plateau_90 d0.74-d1.48	0.679	152.50	275.09	408.44	0.677
Lotus_90 d0.74-d1.48	0.687	126.88	287.10	403.44	0.677
Upperbound_90 d1.48	0.866	124.84	263.05	286.10	-

4.2.2 – Aluminum-A numerical results

As for the PLA numerical results, for the Aluminum-A results, the Siemens NX software was used. Only one set of specimens was designed, with a G parameter of 0.080. The dimensions of the specimens were smaller than the PLA specimens due to the dimensions of the printing chamber of the SLM printer.

There are two regular honeycomb structures, one Lowerbound d=1.165 and one Upperbound d=0.815. There will be no experimental results for the Aluminum-A specimens due to the pandemic situation. There are also, three configurations, the Hexagonal, Lotus and Plateau. The Table 4.5 summarizes all the results.

Table 4.5 - Values of relative density, G parameter and values of stress, initial stiffness, Absorbed Energy corrected with relative density for different structures (G=0.080).

Geometry	$\bar{\rho}$	$\bar{\sigma}_y/\bar{\rho}$ **(MPa)**	$K/\bar{\rho}$ **(N/mm)**	$E_a/\bar{\rho}$ **(N.mm)**	**G parameter**
Lowerbound d 0.815	0.579	11632.33	22146.22	31799.84	-
Hexagonal d0.815-1.165	0.678	9745.82	30077.33	33345.57	0.080
Plateau d0.815-1.165	0.679	11346.95	30519.23	43770.98	0.080
Lotus d0.815-1.165	0.708	8820.90	31888.51	39450.69	0.080
Upperbound d1.165	0.768	9451.84	29670.27	32334.69	-

For the Aluminum-A structures, the numerical results show that the best results for K were achieved by Lotus structures, followed by the Plateau and then the Hexagonal. For the absorbed energy, the higher values were achieved by the Plateau structures, followed by the Lotus and then the Hexagonal. In both parameters, the structures which have a G parameter performed better than those which do not have.

4.3 – Experimental results

The experimental tests were performed with only one G parameter. The specimens with better dimensions for AM were selected. This selection was based on the nozzle diameters available. The selected G parameter was the 0.091. The other G parameters had associated small wall thicknesses, and because of that, the number of layers would be very small. The obtained results, would not be suitable for comparison. Contrary to the results presented in section 4.2, which were for only a quarter of the geometry, results in this section are presented for the entire geometry.

After accomplishing the experimental tests, the raw data from *Bluehill* software was extracted and treated. The results are shown in Table 4.6. The results will be presented until 2.5 mm of vertical displacement to compare with the numerical results. The entire Load vs Displacement curve will be exhibited as well. All geometries had three samples each.

All three samples had a very similar result during the 3PB testing (Figure 4.7). Presenting firstly the results for displacement until 2.5 mm for the three Hexagonal samples, Table 4.7 shows the values of initial stiffness and absorbed energy for each of the three samples of displacement until 2.5 mm.

Table 4.6 - Experimental results of load for 2.5 mm displacement for the 3 Hexagonal samples.

Sample	***Load (N)***
Hexagonal 1	2304.88
Hexagonal 2	2505.09
Hexagonal 3	2304.28
Average	2371.42

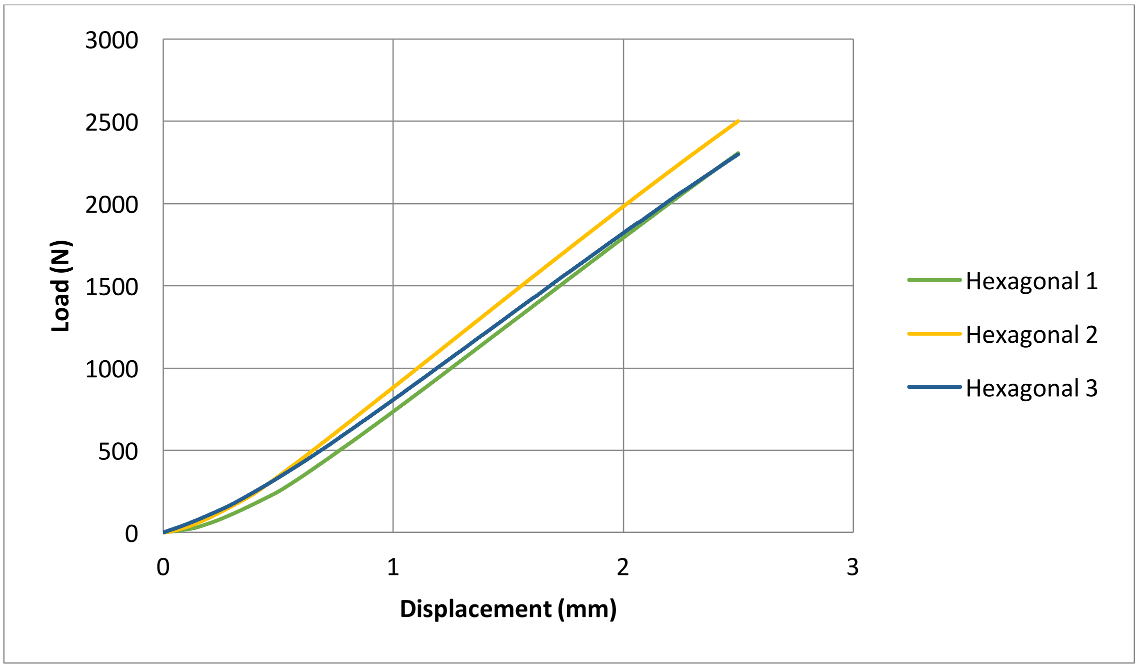

Figure 4.7 - Experimental Load vs Displacement curve for a maximum displacement of 2.5 mm Hexagonal (G=0.091).

Table 4.7 - Initial stiffness and absorbed energy for the 3 Hexagonal samples.

Sample	***K (N/mm)***	***Ea (N.mm)***
Hexagonal 1	1054.66	2574.60
Hexagonal 2	1100.31	2940.07
Hexagonal 3	1014.61	2705.04
Average	1056.53	2739.90

The absorbed energy was obtained computing the area below the curve. The curves were obtained in excel using a trend line modulated in a 5th degree polynomial. Table 4.7 presents the values of K and E_a for each Hexagonal sample.

With the Plateau arrangement, were tested three samples. The results are shown below. The load values at 2.5 mm displacement shows a significant difference in the third sample (Figure 4.8). That significant difference can be due to a manufacturing defects. This problem was visible as well when observing the failure mode. Table 4.8 shows the corresponding load for the 2.5 mm displacement for the Plateau samples. Table 4.8 presents the values for the initial stiffness and absorbed energy for each of the Plateau samples.

Table 4.8 - Experimental results of load for 2.5 mm displacement for the 3 Plateau samples.

Sample	***Load (N)***
Plateau 1	2381.12
Plateau 2	2533.86
Plateau 3	1626.24
Average	2180.41

The first two samples presented values that are closer to the values achieved with Hexagonal samples. The third sample has a deviation of 31.7 % compared with sample 1 and 35.82 % compared with sample 2. Table 4.9 presents the values of K and E_a for each Plateau sample.

Table 4.9 - Initial stiffness and absorbed energy for the 3 Plateau samples.

Sample	***K (N/mm)***	***Ea (N.mm)***
Plateau 1	1034.73	2793.09
Plateau 2	1061.61	3118.11
Plateau 3	730.92	1798.48
Average	942.42	2569.89

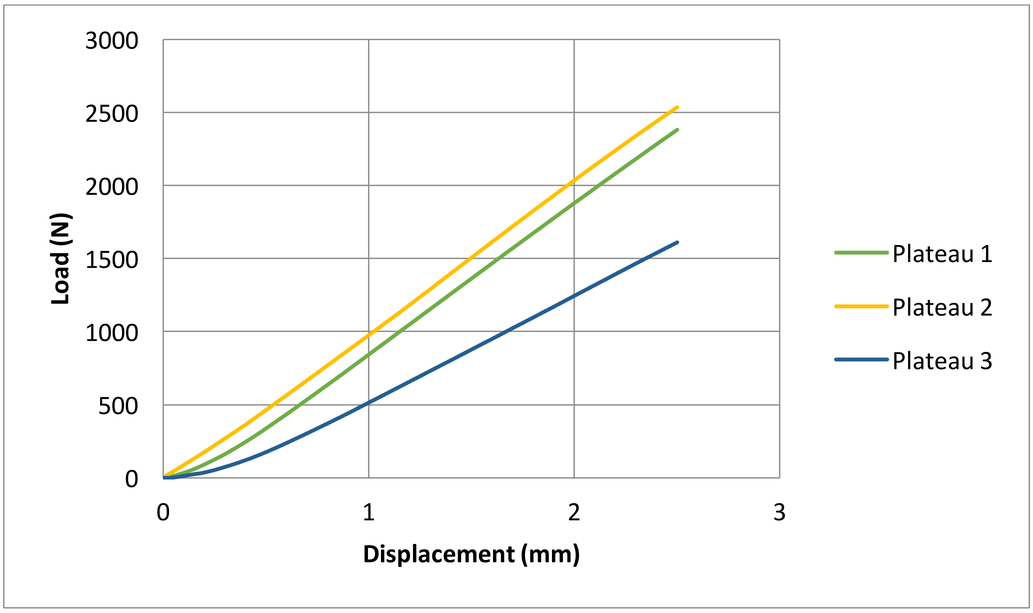

Figure 4.8 - Experimental Load vs Displacement curve for a maximum displacement of 2.5 mm Plateau (G=0.091).

Three samples of the Lotus geometry were tested, and the results were very similar for the three samples (Figure 4.9). The results are similar for all three samples. Its failure mode was not in accordance with the rest of the samples (the failure modes will be analyzed later in this chapter). Table 4.10 shows the corresponding load for the 2.5 mm displacement for the Lotus samples. Table 4.11 presents the values for the initial stiffness and absorbed energy for Lotus samples.

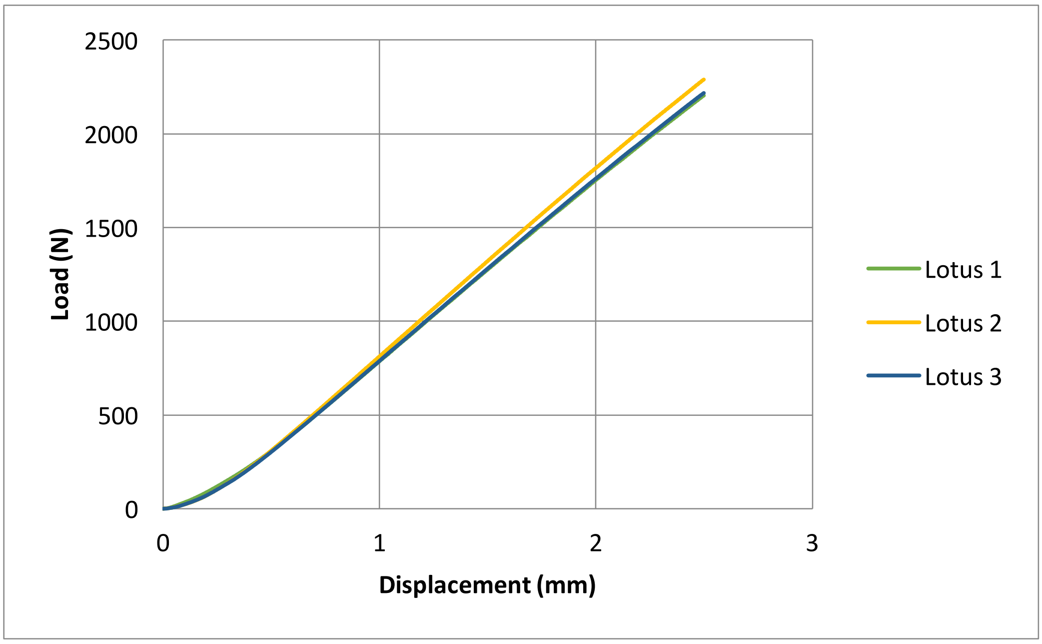

Figure 4.9 - Experimental Load vs Displacement curve for a maximum displacement of 2.5 mm Lotus (G=0.091).

Table 4.10 - Experimental results for 2.5 mm displacement for the 3 Lotus samples.

Sample	***Load (N)***
Lotus 1	2205.56
Lotus 2	2290.37
Lotus 3	2219.53
Average	2238.49

Table 4.11 - Initial stiffness and absorbed energy for the 3 Lotus samples.

Sample	***K (N/mm)***	***Ea (N.mm)***
Lotus 1	966.46	2601.67
Lotus 2	1004.37	2687.16
Lotus 3	971.61	2608.04
Average	980.81	2632.29

The results for the Lotus structures were expected to be the highest ones, although, and because of the manufacturing issue, that was not the case.

The homogeneous structures (without a density gradient), namely Upperbound d=0.80 and Lowerbound d=1.20 are presented next. These structures represent the results for structures with the higher and the lower densities. Three samples of the Upperbound d=0.80 samples, had very similar results among them (Figure 4.10). Table 4.12 present the values of load for 2.5 mm for each Upperbound sample. Table 4.13 presents the values for the initial stiffness and absorbed energy for each sample.

Table 4.12 – Experimental results for 2.5 mm displacement for the 3 Upperbound samples.

Sample	***Load (N)***
Upperbound 1	1929.48
Upperbound 2	1944.62
Upperbound 3	1996.74
Average	1956.95

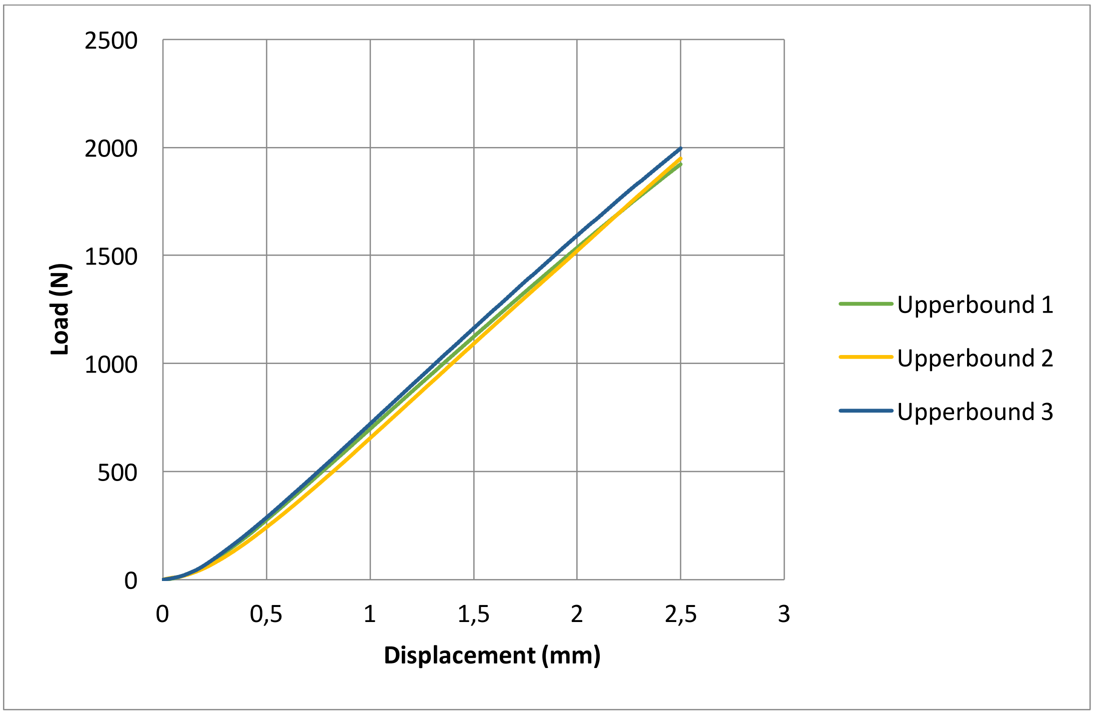

Figure 4.10 - Experimental Load vs Displacement curve for a maximum displacement of 2.5 mm Upperbound (G=0.091).

Table 4.13 - Initial stiffness and absorbed energy for the 3 Upperbound samples.

Sample	***K (N/mm)***	***Ea (N.mm)***
Upperbound 1	838.08	2281.34
Upperbound 2	865.47	2218.67
Upperbound 3	872.45	2368.02
Average	858.67	2289.34

The results for the Upperbound d=0.80, were lower than Hexagonal, Plateau and Lotus.

The Lowerbound d=1.20, had three samples. The load results for the 3PB test of the three samples are presented in Table 4.14. Table 4.15 present the results for the initial stiffness and absorbed energy for Lowerbound samples. As expected, this structure presented the lower values for all the analyzed parameters, once it has the lower relative density. The three samples had two very similar results and one sample presented a higher value than the other two (Figure 4.11).

Table 4.14 – Experimental results for 2.5 mm displacement for the 3 Lowerbound samples.

Sample	***Load (N)***
Lowerbound 1	939.24
Lowerbound 2	1271.08
Lowerbound 3	993.89
Average	1068.07

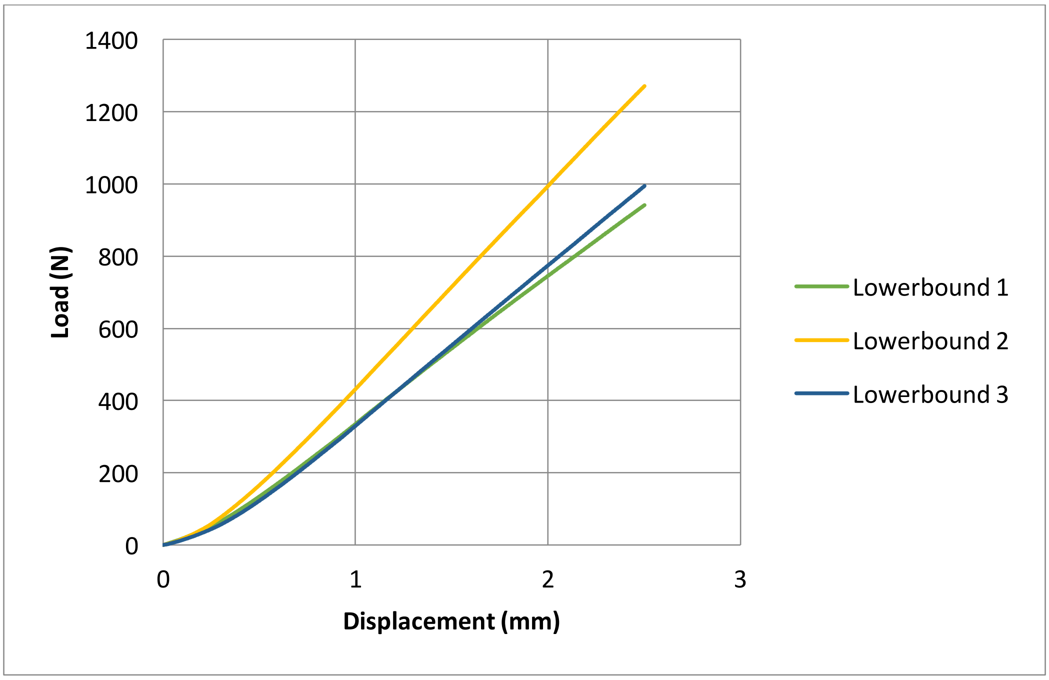

Figure 4.11 - Experimental Load vs Displacement curve for a maximum displacement of 2.5 mm Lowerbound (G=0.091).

Table 4.15 - Initial stiffness and absorbed energy for the 3 Lowerbound samples.

Structure	***K (N/mm)***	***Ea (N.mm)***
Lowerbound 1	409.47	1108.41
Lowerbound 2	561.83	1466.06
Lowerbound 3	443.63	1133.01
Average	471.64	1235.83

All the values showed in the experimental results section, were absolute and none were normalized with the relative density. Table 4.16 presents the average values scaled with the relative density and the standard deviation.

Table 4.16 – Average and standard deviation values of load, initial stiffness and absorbed energy scaled to the relative density for the different structures.

Structure	$\bar{\rho}$	***$L/\bar{\rho}$ (N)***	±	***$K/\bar{\rho}$ (N/mm)***	±	***$E_a/\bar{\rho}$ (N.mm)***	±
Lowerbound	0.585	1825.76	248.32	806.22	111.59	2112.53	278.82
Hexagonal	0.684	3466.99	138.19	1544.64	51.18	4005.71	221.096
Plateau	0.685	3183.08	579.26	1375.80	217.53	3751.67	819.38
Lotus	0.713	3139.53	52.08	1375.61	23.55	3691.85	54.54
Upperbound	0.782	2502.49	36.84	1098.04	18.96	2927.55	78.30

In the experimental tests, the functional graded cellular structures (Hexagonal, Plateau and Lotus) had a better performance than the other cellular structures (Lowerbound and Upperbound) in terms of strength, stiffness and absorbed energy.

The load needed for a displacement of 2.5 mm was higher for the Hexagonal structure, then for the Plateau structure and then for the Lotus structure. The lower value, as expected was achieved by the Lowerbound structure. The Upperbound structure, despite its designation, did not performed as an upper bound.

The highest initial stiffness value was obtained with the Hexagonal configuration, the second highest value was performed by the Plateau structure. The third highest value, being almost the same value as the Plateau structure, was obtained with the Lotus structure. Both homogeneous structures did not perform as good as the functional graded cellular structures.

The highest absorbed energy value was obtained by the Hexagonal configuration, followed by the Plateau configuration and then by the Lotus configuration. Both homogeneous structures, once more, were outperformed by the functional graded cellular structures.

4.4 – Results until failure

The results and analysis obtained until the failure of the samples are presented below. The load at break was obtained by analyzing the maximum load value. When loads are applied perpendicular to axis X in the functional graded cellular structures, failure of cells should start at the mid-section of the samples. This is not what happened. The defects on the manufacturing of the samples are more visible when analyzing the location of the failure and the location of the mid-section of the sample.

The results of maximum load for the Hexagonal core geometry samples are presented in Table 4.17 and Figure 4.12. The Hexagonal core geometry samples performed the best. These results relate to the failure mode in these structures. As expected, the break happened in the mid-section of the specimens in all Hexagonal core samples. Failure modes will be presented in section 4.5.

Table 4.17 –Load and displacement at break for the 3 Hexagonal samples.

Geometry	***Load at break (N)***	***Disp. at break (mm)***	***E_a (Nmm)***
Hexagonal 1	4404.16	6.65	21950.66
Hexagonal 2	4522.79	7.03	25090.36
Hexagonal 3	4187.24	6.55	21816.41
Average Hexagonal	4371.40	6.74	22952.48

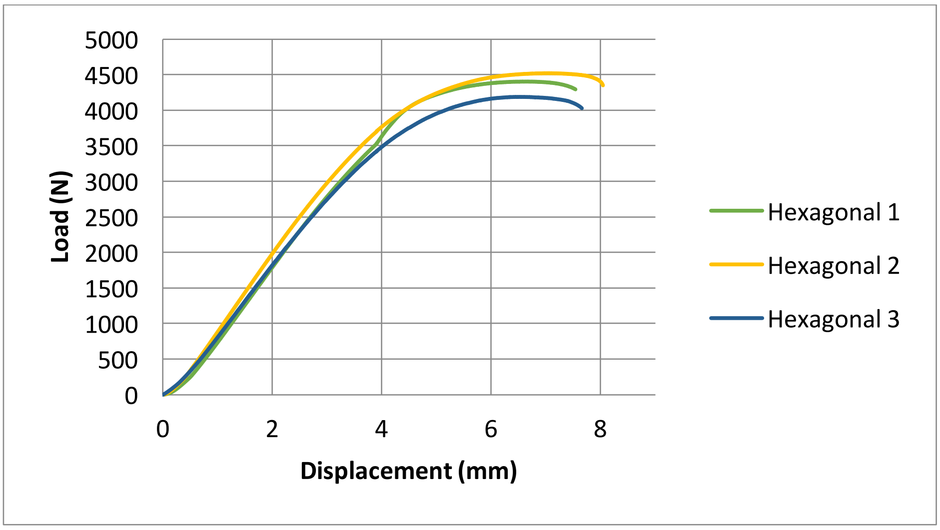

Figure 4.12 – Load vs Displacement curves until break of the 3 Hexagonal samples (G=0.091).

The Load vs Displacement plots were very similar in all three samples, only varying in values. It is visible the elastic region, the yield point, the plastic region and maximum load.

The Load vs Displacement plots of the three Plateau core samples (Figure 4.13), had different performances. The Plateau 1 and Plateau 2 presented very similar curves. The same cannot be observed with Plateau 3 curve. All three clearly present an elastic region, a plastic region, being more pronounced in Plateau 3 sample. Table 4.18 presents the values for load at break, displacement at break and absorbed energy.

Table 4.18 - Load and displacement at break for the 3 Plateau samples.

Geometry	***Load at break (N)***	***Disp. at break (mm)***	***E_a (Nmm)***
Plateau 1	4281.97	6.45	21339.44
Plateau 2	4149.56	6.45	21205.60
Plateau 3	3212.51	7.37	21230.25
Average Plateau	3881.35	6.76	21258.43

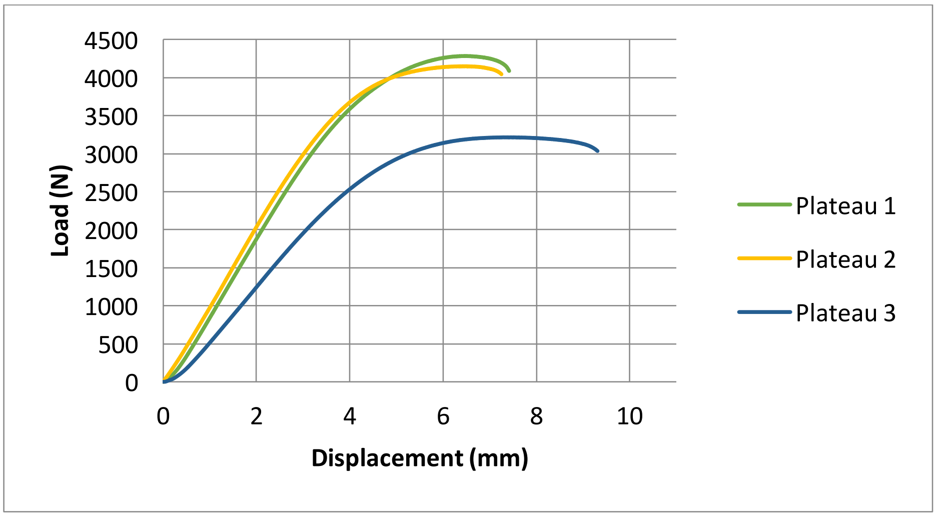

Figure 4.13 - Load vs Displacement curves until break of the 3 Plateau sample (G=0.091).

The Load vs Displacement plots of the three Lotus core samples (Figure 4.14) presented three very similar curves. One can observe that exists an elastic region but there is no non-linear region, plastic region. It is well visible the yield point. This lack of plastic region, being the only core design without a non-linear region, can be justified by a possible manufacturing defect. Table 4.19 presents the values for load at break, displacement at break and absorbed energy.

Table 4.19 - Load and displacement at break for the 3 Lotus samples.

Geometry	***Load at break (N)***	***Disp. at break (mm)***	***E_a (Nmm)***
Lotus 1	2939.03	3.54	5791.48
Lotus 2	3058.45	3.54	5999.33
Lotus 3	3231.84	3.97	6809.32
Average Lotus	3076.44	3.68	6200.04

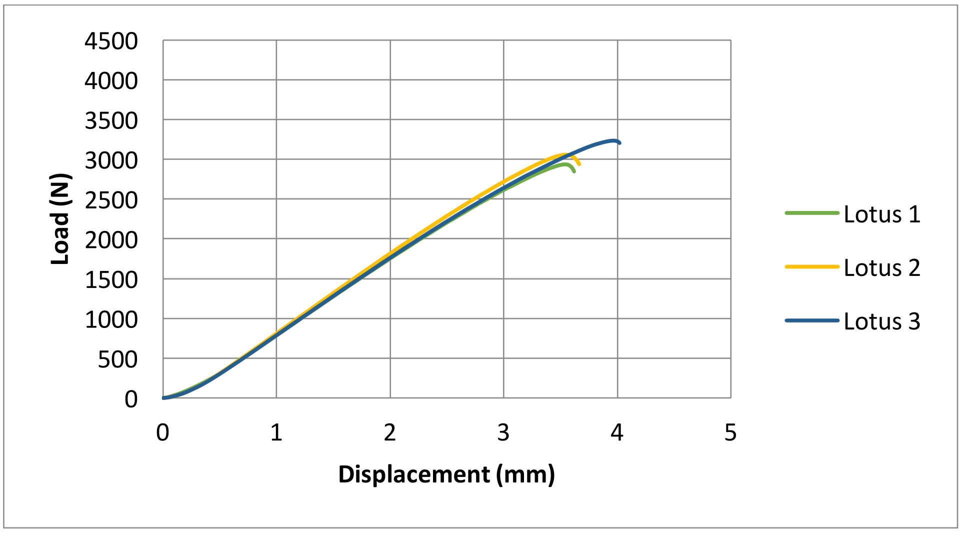

Figure 4.14 - Load vs Displacement curves until break of the 3 Lotus samples (G=0.091).

The Load vs Displacement plots of the three Upperbound d=0.80 structures (Figure 4.15) presented a similar elastic region. Again, there are visible two regions, an elastic region and a plastic one, in Upperbound 2 and Upperbound 3. For the Uppererbound 1, there is not an extreme plastic region. There are also visible the yield points. Table 4.20 presents the values for load at break, displacement at break and absorbed energy.

Table 4.20 - Load and displacement at break for the 3 Upperbound samples.

Geometry	**Load at break (N)**	**Disp. at break (mm)**	**E_a (Nmm)**
Upperbound 1	2939.74	4.59	8385.53
Upperbound 2	3436.84	5.86	18248.45
Upperbound 3	3305.41	5.97	16075.51
Average Upperbound	3227.33	5.47	14236.49

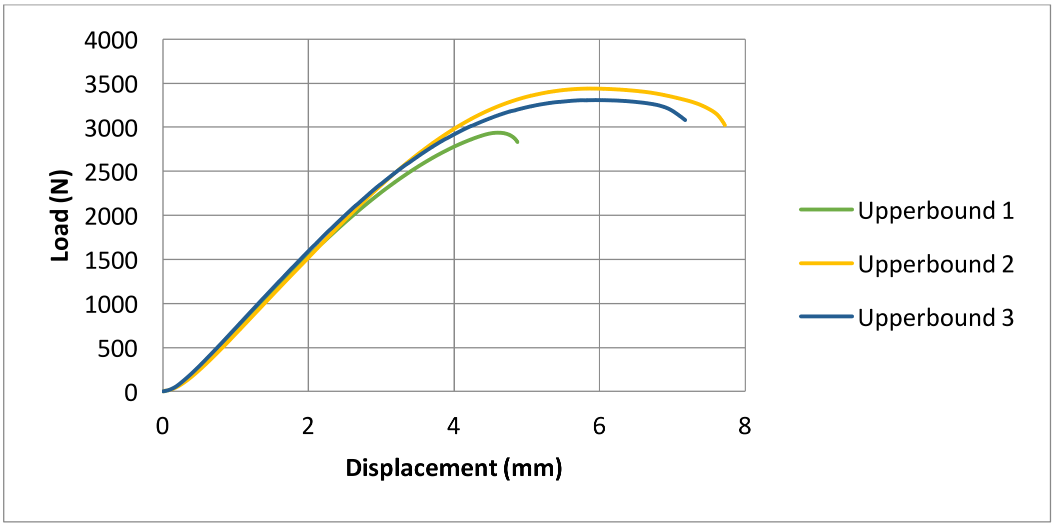

Figure 4.15 - Load vs Displacement curves until break of the 3 Upperbound samples (G=0.091).

The Load vs Displacement plots of the three Lowerbound structures (Figure 4.16) present a similar curve shape, with different values. It is clearly visible an elastic region and a plastic one. There are also visible the yield points. Table 4.21 presents the values for load at break, displacement at break and absorbed energy.

Table 4.21 - Load and displacement at break for the 3 Lowerbound samples.

Geometry	**Load at break (N)**	**Disp. at break (mm)**	**E_a (Nmm)**
Lowerbound 1	1643.32	6.32	10341.80
Lowerbound 2	2313.05	7.07	15107.20
Lowerbound 3	1786.09	6.42	11706.30
Average Lowerbound	1914.15	6.60	12385.1

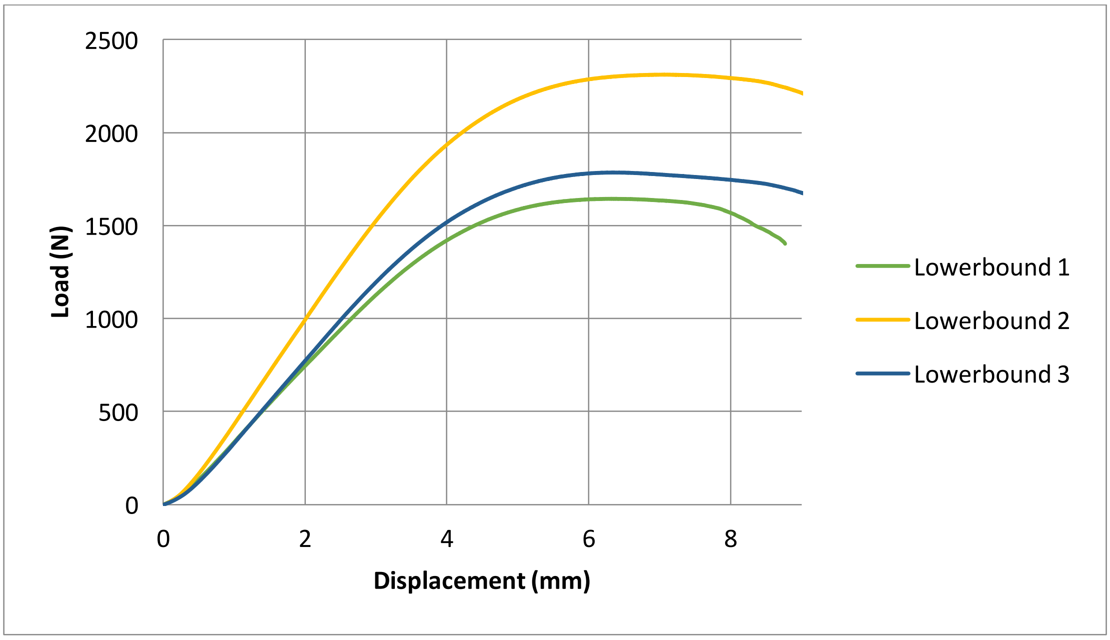

Figure 4.16 – Load vs Displacement curves until break of the 3 Lowerbound samples (G=0.091).

The Table 4.22 presents the summarized values presented in this section. These values are normalized, being corrected with the relative density. Moreover, the standard deviation is presented for each parameter.

Table 4.22 – Average and standard deviation values of load until breaking, initial stiffness and absorbed energy.

Structure	$\bar{\rho}$	$L_B/\bar{\rho}$ (N)	±	$K/\bar{\rho}$ (N/mm)	±	$E_a/\bar{\rho}$ (J)	±
Lowerbound	0.585	3272.05	492.34	806.22	111.59	21.17	3.43
Hexagonal	0.684	6390.94	237.49	1544.64	51.18	33.56	2.21
Plateau	0.685	5666.20	694.92	1375.80	217.53	31.03	0.08
Lotus	0.713	4314.78	168.60	1375.61	23.55	8.70	0.62
Upperbound	0.782	4127.02	268.95	1098.04	18.96	18.21	5.41

The structure with higher load at breaking was the Hexagonal, followed by the Plateau and then the Lotus. These results are coincident with the initial stiffness, K, presenting the same order. Comparing with the regular honeycomb structures, once more represented by the Lowerbound and Upperbound structures, the structures with density gradient (G=0.091 for this case) achieved better results in all the studied parameters.

4.5 – Failure observations

Failure surfaces were observed for all samples. All photographs exhibit two lines: in red the failure behavior and in blue the mid-section of each specimen. Only for Lowerbound and Upperbound samples, the red line and blue line correspond to a same cell thickness. For all the others, the blue line corresponds for the mid-section of the specimens and consequently, it has a thicker cell than a red line which is not coincident.

Figure 4.17 exhibits the failure surface of Hexagonal samples. The deviation relative to the mid-section of the sample can be caused by the indenter not being a point, but a surface. All three Hexagonal samples presented the same failure results. The failure is well visible that happens inside the core as well. The region where the failure occurs has a lower cell thickness compared to the mid-section. Comparing to section 4.2.1, analyzing both the Figure 4.2 b) and Figure 4.17, in the numerical simulation, for the Hexagonal structure, the maximum von Mises stress occurred in the support contact area.

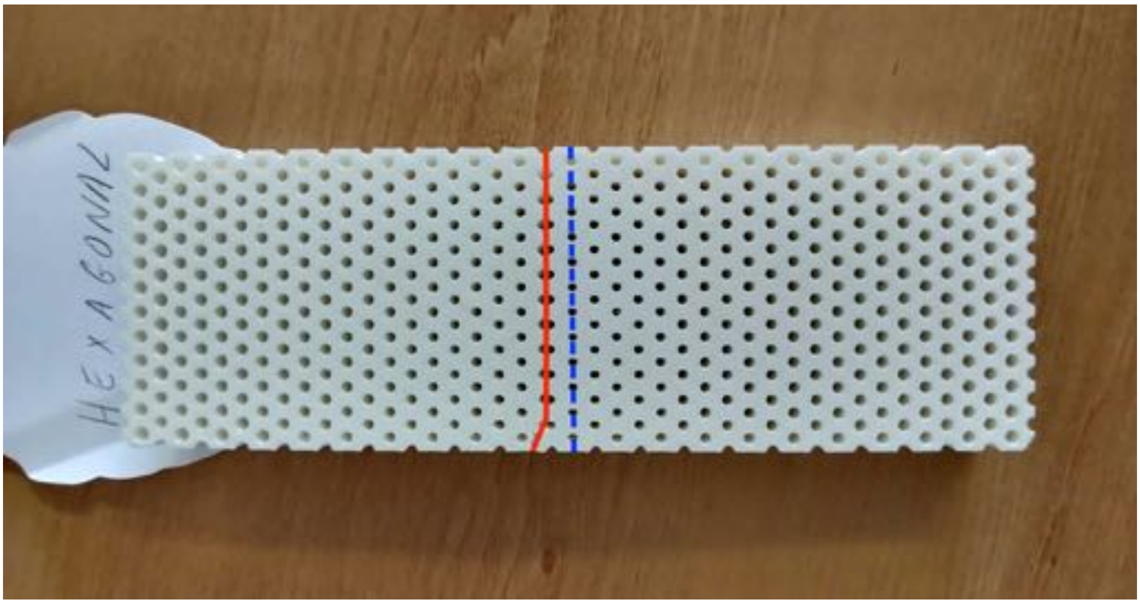

Figure 4.17 –Failure mode of a Hexagonal sample, in blue representing the mid-section of the specimen and in red the experimental failure mode.

The failure mode for the three Plateau specimens (Figure 4.18) were very similar to the failure mode in the Hexagonal specimens. The failure is well visible inside the core. The propagation of the failure does not happen through the mid-section of the structure. This can be related, once more, to the fact that the indenter is not a line but a surface. Comparing to section 4.2.1, analyzing both the Figure 4.3 b) and Figure 4.18, in the numerical simulation, for the Plateau structure, the maximum von Mises stress occurred in the indenter contact region, in the center of the specimen.

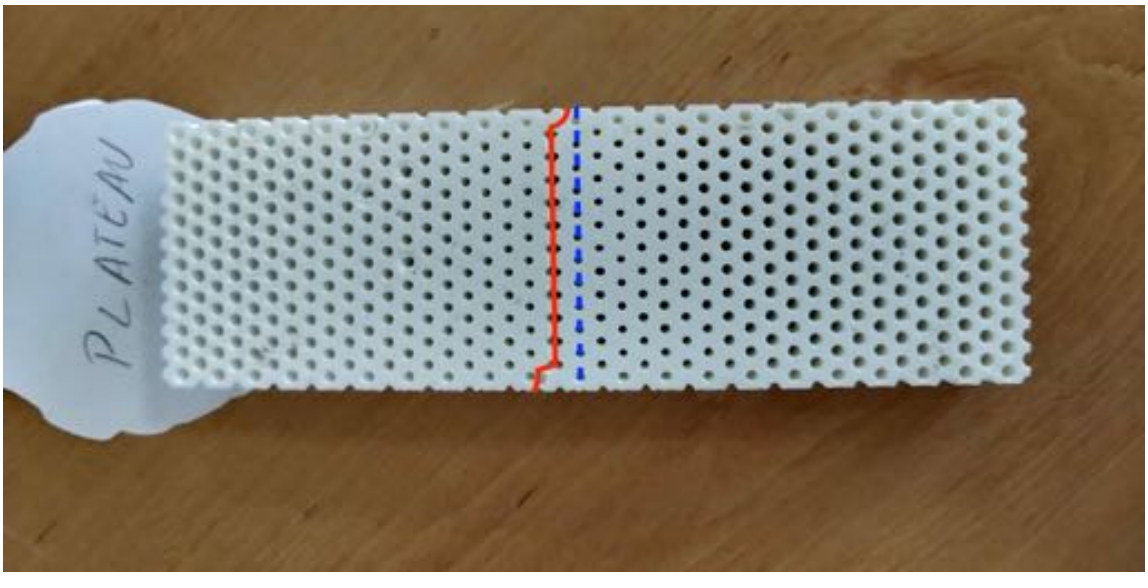

Figure 4.18 - Failure mode of a Plateau sample, in blue representing the mid-section of the specimen and in red the experimental failure mode.

The Lotus samples, all had the same failure behavior. In the Figure 4.19, it is clearly visible that a manufacturing problem occurred. The failure occurred around the Lotus core and far from the mid-section of the structure. This behavior can be related to a common issue associated with FFF, which is the existence of gaps between infill and outline. This is probably the reason for the worst performance was performed by the Lotus samples. Comparing to section 4.2.1, analyzing both the Figure 4.4 b) and Figure 4.19, in the numerical simulation, for the Lotus structure, the maximum von Mises stress occurred in the indenter contact region, in the center of the specimen.

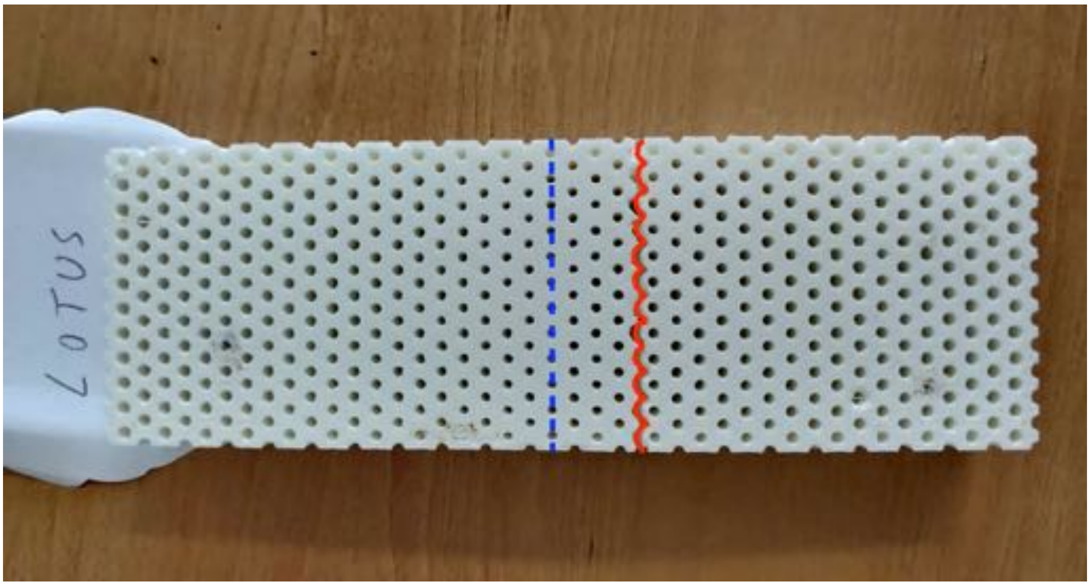

Figure 4.19 - Failure mode of a Lotus sample, in blue representing the mid-section of the specimen and in red the experimental failure mode.

The Upperbound samples (Figure 4.20) performed as expected. The failure occurred inside the core and along the mid-section of the structure. All three samples presented the same failure results. Comparing to section 4.2.1, analyzing both the Figure 4.5 b) and Figure 4.20, in the numerical simulation, for the Upperbound structure, the maximum von Mises stress occurred in the indenter contact region, in the center of the specimen.

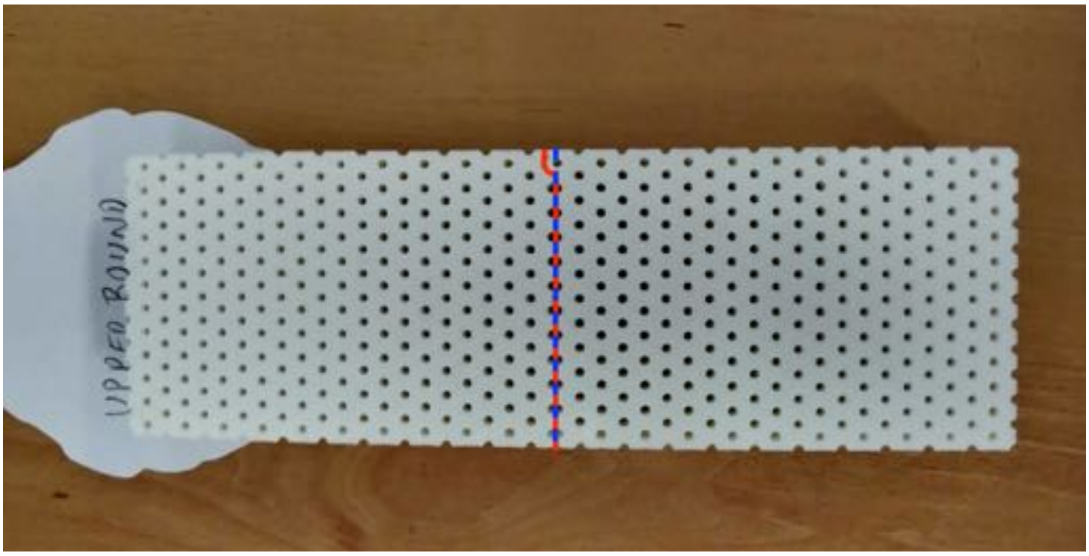

Figure 4.20 - Failure mode of a Upperbound sample, in blue representing the mid-section of the specimen and in red the experimental failure mode.

The Lowerbound samples (Figure 4.21) all performed similarly. The Lowerbound structures were the one with higher displacement. Because of that, and once the structures are subjected to both bending and stretching in addition to other effects as shearing, torsion and nodal interactions, all these interactions were better observed in the Lowerbound case. The failure occurred inside the core and near the mid-section of the specimen. Comparing to section 4.2.1, analyzing both the Figure 4.6 b) and Figure 4.21, in the numerical simulation, for the Plateau structure, the maximum von Mises stress occurred in the indenter contact region, in the center of the specimen.

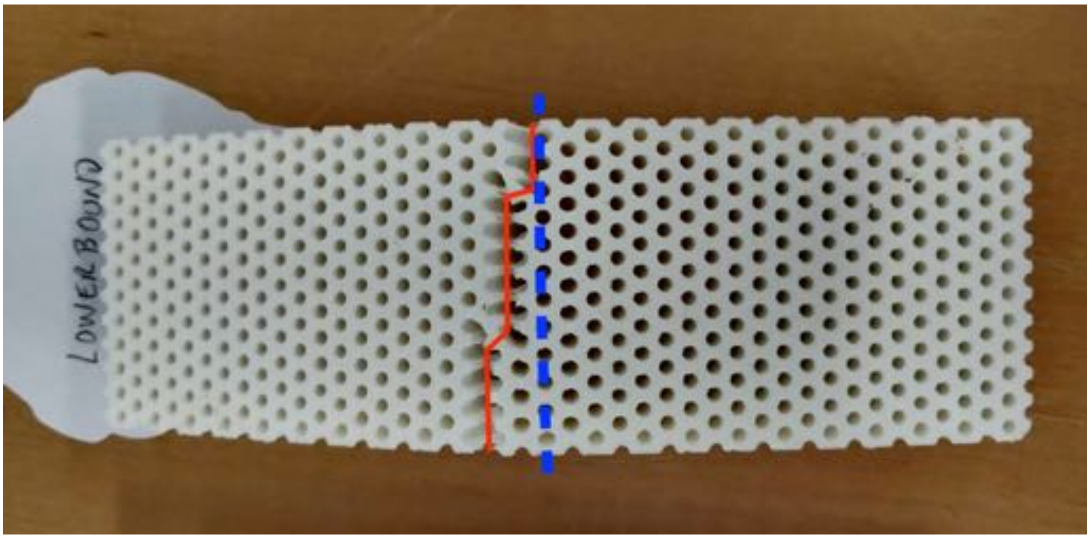

Figure 4.21 - Failure mode of a Lowerbound sample, in blue representing the mid-section of the specimen and in red the experimental failure mode.

4.6 – Correlation between methods

Analyzing the load vs displacement curves of the five structures that were designed to be additively manufactured, it is visible a prevailing of the elastic behavior, although some specimens present a substantial plastic region. This leads, under the range of loads used, to a more brittle fracture, except for the Lowerbound samples that presents a ductile fracture. As the elastic behavior prevails, that is the reason for the linear elastic numerical analysis to be done in order to correlate with the experimental work. For the numerical analysis, the displacement was set to be 2.5 mm and for those values it is clearly visible that all specimens are in the linear region. The following five figures of Figure 4.22 presents the comparison between the experimental data and the numerical data for each topology. Data is summarized in Table 4.23.

Table 4.23 –Comparison between numerical and experimental results, load, K and absorbed energy.

Topology	**Load_Num (N)**	**Load_Exp (N)**	**K_Num (N/mm)**	**K_Exp (N/mm)**	**E.Abs_Num (J)**	**E.Abs_Exp (J)**	**$\sigma_{(vM)}/\bar{\rho}$ (MPa)**
Hexagonal	2538.13	3466.99	1015.25	1544.64	3.15	4.01	151.92
Plateau	2553.46	3183.08	1021.38	1375.80	3.17	3.75	155.80
Lotus	2733.37	3139.53	1093.35	1375.61	3.40	3.69	129.30
Upperbound	2517.04	2502.49	1006.82	1098.04	3.13	2.93	147.65
Lowerbound	1814.99	1825.76	726.00	806.22	2.26	2.12	137.52

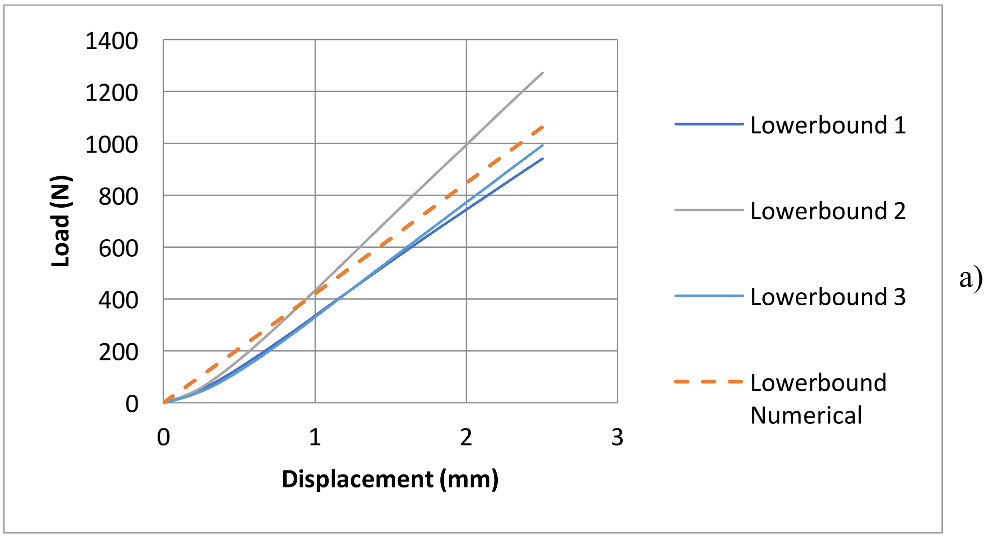

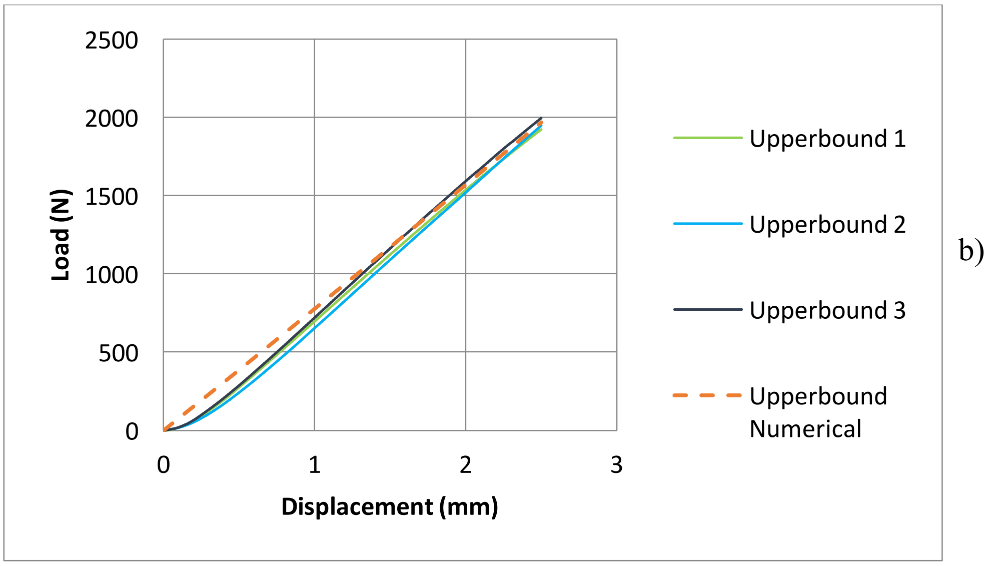

Figure 4.22 - Graphical comparison between experimental samples data and numerical data: a) Lowerbound and b) Upperbound.

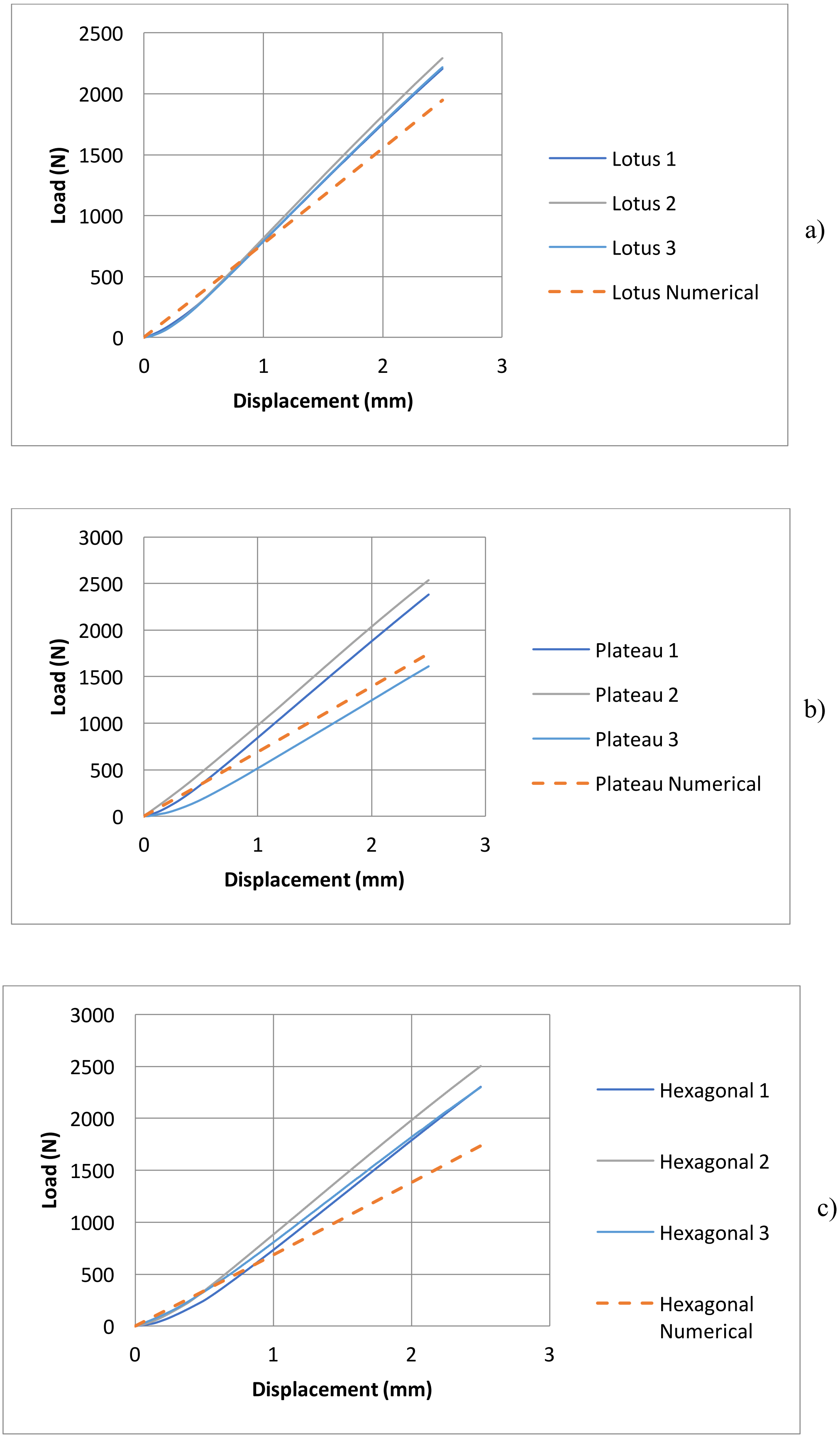

Figure 4.23 – Graphical comparison between experimental samples data and numerical data: a) Lotus, b) Plateau and c) Hexagonal.

The numerical results are in agreement with the experimental results. Deviations in the results may be due to manufacturing defects of the FFF procedure.

Chapter 5

Conclusions

5.1 – Achievements

For this thesis, FGC structures were created using different density gradients, that are characterized by a G parameter. These structures were designed to be applied on sandwich panel cores. The manufacturing of the specimens through FFF allowed the experimental analysis of these structures.

As for the FFF manufacturing process, although it allows the production of structures with quite complex geometries, if they are not homogeneous (regular honeycomb structures), as is the case for structures with density gradient, the setting of the printing parameters requires more complex tuning.

The correspondence between the FEA and the experimental testing was satisfactory, when comparing the loads and the stiffness in both methods. For the failure mode, although the FEA showed that the contact area with the moving roller was the area of higher von Mises stress, the failure did not occur in that manner in most cases. That was due to manufacturing defects – Lotus – and due to a slight deviation of the moving roller.

Once the correlation between methods is deemed satisfactory, the FEA results can be validated. For all geometries, the functionally graded cellular structures presented a better performance when compared to regular cellular structures in terms of strength, stiffness and absorbed energy.

Geometry wise, in FEA, the geometry with better performance depended on the rotation of the structure. The performance depends on the angle. For 0-degree rotation, structures with G parameter of 0.091, 0.105 and 0.212 Lotus had had the better performance. For 90-degree rotation, the structure with higher stiffness was the Hexagonal and the structure with higher absorbed energy value was the Plateau.

When analyzing the Aluminum FEA results, with an G parameter of 0.080 and 0-degree rotation, the geometry with the higher stiffness was the Lotus and the one with higher absorbed energy value was the Plateau.

The core design and the G parameter were found to be the main influences of the mechanical properties. Having a G parameter influences positively both in stiffness and absorbed energy ability. The structures with G parameter of 0 performed the worst in all parameters. Although the structures with G parameter of 0.212 performed better than the ones with G parameter of 0.091 showing that the performance gets better with the higher G parameter, that was not the case for structures with G parameter of 0.105, which performed slightly worse than structures with G parameter of 0.091.

Finally, this work concludes firstly that the performance of FGC structures may be better than regular honeycomb structures, which presented both numerically and experimentally higher values of stiffness and energy absorption. Secondly, it may be concluded that the higher the G parameter, the better is the mechanical performance of the structures. Thirdly, for 0-degree rotation, the Lotus structures are superior to the more common Hexagonal ones. Therefore, the FGC structures may be substitutes to conventional structures in the design of composite panels.

5.2 – Future work

Future work on this topic may consist of performing a numerical and experimental comparison using Aluminum-A and SLM manufacturing process, since that was not possible due to the covid-19 pandemic situation.

Other future work would be managing to produce a viable analysis using less computational space and processing time. This can be studied by performing a scale test as shown in a very preliminary analysis presented in Appendix C.

Bibliography

[1] Ronan, William, et al. “The Tensile Ductility of Cellular Solids: The Role of Imperfections.” *International Journal of Solids and Structures*, vol. 102-103, 15 Dec. 2016, pp. 200–213., doi:10.1016/j.ijsolstr.2016.10.004.

[2] Campbell, F. C. *Structural Composite Materials*. ASM International, 2010.

[3] “Honeycomb structure”. In OpenLab at City Tech. https://openlab.citytech.cuny.edu/detienne-eportfolio/academics/building-tech-3/exterior-research/honeycomb-composite/. Accessed: 2020-10-25

[4] Araújo, Hugo, et al. “The Effect of Geometry on the Flexural Properties of Cellular Core Structures.” *Jornal of Materials: Design and Applications*, vol. 233, no. 3, 11 Oct. 2018, pp. 338–347., doi:10.1177/1464420718805511.

[5] “Composite material”. In Wikipedia. https://en.wikipedia.org/wiki/Composite_material. Accessed: 2020-09-15

[6] Araújo, H., M. Leite, A. Ribeiro, A. M. Deus, L. Reis, and M. F. Vaz. “Investigating the Contribution of Geometry on the Failure of Cellular Core Structures Obtained by Additive Manufacturing”. *Frattura Ed Integrità Strutturale*, vol. 13, no. 49, June 2019, pp. 478-86, doi:10.3221/IGF-ESIS.49.45.

[7] Gibson, Lorna J., and Michael F. Ashby. *Cellular Solids: Structure and Properties*. Cambridge Univ. Press, 1999.

[8] Vatanabe, S.l., et al. “Modeling of Functionally Graded Materials.” *ComprehensiveMaterials Processing*, 2014, pp. 261–282., doi:10.1016/b978-0-08-096532-1.00222-3.

[9] Miranda, Rosa. “Surface Reinforcements of Light Alloys.” *Surface Modification by Solid State Processing*, 2014, pp. 113–152., doi:10.1533/9780857094698.113.

[10] Liang, Minzu, et al. “Theoretical and Numerical Investigation of Blast Responses of Continuous-Density Graded Cellular Materials.” *Composite Structures*, vol. 164, Mar. 2017, pp. 170–179., doi: 10.1016/j.compstruct.2016.12.065.

[11] Xiao, Lijun, and Weidong Song. “Additively-Manufactured Functionally Graded Ti-6Al-4V Lattice Structures with High Strength under Static and Dynamic Loading: Experiments.” *International Journal of Impact Engineering*, vol. 111, 2018, pp. 255–272., doi:10.1016/j.ijimpeng.2017.09.018.

[12] Y. Zhang, M. Xiao, X. Zhang et al., “Topological design of sandwich structures with graded cellular cores by multiscale optimization”, Computer Methods in Applied Mechanics and Engineering , 2019. p.112749, doi: 10.1016/j.cma.2019.112749.

[13] Zhang, Chi & Huang, Zhifeng & Jia, Mingyong & Chen, Guiyi & Ye, Yongqiang & Lin, Yaojun & Liu, Wei & Chen, Bingqing & Shen, Qiang & Zhang, L. & Lavernia, Enrique. (2019). Additive

manufacturing of functionally graded materials: A review. Materials Science and Engineering A. 762. 138209. 10.1016/j.msea.2019.138209.

[14] Brothers, Alan H, and David C Dunand. “Mechanical Properties of a Density-Graded Replicated Aluminum Foam.” *Materials Science and Engineering: A*, vol. 489, no. 1-2, Aug. 2008, pp. 439–443., doi:10.1016/j.msea.2007.11.076.

[15] Ajdari, A., et al. “Mechanical Properties of Functionally Graded 2-D Cellular Structures: A Finite Element Simulation.” *Materials Science and Engineering: A*, vol. 499, no. 1-2, 2009, pp. 434–439., doi:10.1016/j.msea.2008.08.040.

[16] Zeng, H.b., et al. “Impact Behaviour of Hollow Sphere Agglomerates with Density Gradient.” *International Journal of Mechanical Sciences*, vol. 52, no. 5, May 2010, pp. 680–688., doi:10.1016/j.ijmecsci.2009.11.012.

[17] Li, Shiqiang, et al. “Finite Element Simulation of Metallic Cylindrical Sandwich Shells with Graded Aluminum Tubular Cores Subjected to Internal Blast Loading.” *International Journal of Mechanical Sciences*, vol. 96-97, June 2015, pp. 1–12., doi:10.1016/j.ijmecsci.2015.03.011.

[18] Jin, Xiaochao, et al. “Dynamic Response of Sandwich Structures with Graded Auxetic Honeycomb Cores under Blast Loading.” *Composites Part B: Engineering*, vol. 106, Dec. 2016, pp. 206–217., doi:10.1016/j.compositesb.2016.09.037.

[19] Xiao, Lijun, and Weidong Song. “Additively-Manufactured Functionally Graded Ti-6Al-4V Lattice Structures with High Strength under Static and Dynamic Loading: Experiments.” *International Journal of Impact Engineering*, vol. 111, 2018, pp. 255–272., doi:10.1016/j.ijimpeng.2017.09.018.

[20] Limmahakhun, Sakkadech, et al. “Stiffness and Strength Tailoring of Cobalt Chromium Graded Cellular Structures for Stress-Shielding Reduction.” *Materials & Design*, vol. 114, Jan. 2017, pp. 633–641., doi:10.1016/j.matdes.2016.11.090.

[21] Mirzaali, M.j., et al. “Mechanics of Bioinspired Functionally Graded Soft-Hard Composites Made by Multi-Material 3D Printing.” *Composite Structures*, vol. 237, 3 Jan. 2020, p. 111867., doi:10.1016/j.compstruct.2020.111867.

[22] Bru, J, et al. “Bioinspired Structures for Core Sandwich Composites Produced by Fused Deposition Modelling.” *Proceedings of the Institution of Mechanical Engineers, Part L: Journal of Materials: Design and Applications*, vol. 234, no. 3, 22 Nov. 2019, pp. 379–393., doi:10.1177/1464420719886906.

[23] Vicente, Carlos, et al. “Effect of Protective Coatings on the Water Absorption and Mechanical Properties of 3D Printed PLA.” *Frattura Ed Integrità Strutturale*, vol. 13, no. 48, 15 Apr. 2019, pp. 748–756., doi:10.3221/igf-esis.48.68.

[24] J. Fernandes, A. M. Deus, L. Reis, M. F. Vaz, and M. Leite. “Study of the influence of 3D printing parameters on the mechanical properties of PLA”. *Proceedings of the International Conference on Progress in Additive Manufacturing*, May. 2018. ISSN 24248967. doi: 10.25341/D4988C.

[25] L. J. Gibson. “cellular solids: Structure, properties and applications - lecture notes”. in: Mit courses (2015). https://ocw.mit.edu/courses/materials-science-and-engineering/ 3-054-cellular-solids-structure-properties-and-applications-spring-2015/ lecture-notes/. Accessed: 2019-08-06.

[26] Hexcel Corporation (2016). HexWeb® Honeycomb Attributes and Properties. In Hexcel. hexcel.com/Products/Honeycomb/. Accessed: 2020-04-17

[27] “2 - Honeycomb Core.” *Honeycomb Technology: Materials, Design, Manufacturing, Applications and Testing*, by T. N. Bitzer, Springer, 2012, pp. 11–24.

[28] Totten, George E., et al. *Encyclopedia of Aluminum and Its Alloys*. CRC Press, 2018.

[29] Monzon, Mario & Ortega, Zaida & Martínez, A. & Ortega, F.. (2014). Standardisation in additive manufacturing: Activities carried out by international organizations and projects. The International Journal of Advanced Manufacturing Technology. 76. 1111-1121. 10.1007/s00170-014-6334-1.

[30] Syed A.M. Tofail, Elias P. Koumoulos, Amit Bandyopadhyay, Susmita Bose, Lisa O'Donoghue, Costas Charitidis,Additive manufacturing: scientific and technological challenges, market uptake and opportunities,Materials Today,Volume 21, Issue 1,2018,Pages 22-37,ISSN 1369-7021,https://doi.org/10.1016/j.mattod.2017.07.001.

[31] Gibson, I., et al. *Additive Manufacturing Technologies: 3D Printing, Rapid Prototyping, and Direct Digital Manufacturing*. Springer, 2016.

[32] Alkaios Bournias Varotsis. Introduction to FDM 3D printing, How does FDM work? Schematic of a typical FDM printer. https://www.3dhubs.com/ knowledge-base/introduction-fdm-3d-printing. Accessed: 2020-05-25.

[33] B. Redwood, F. Schöffer e B. Garret. *The 3D Printing Handbook: Technologies, design and applications*. 3D Hubs B.V., 2017, pp. 13–14, 34–62, 205–206. ISBN 9082748509.

[34] Alkaios Bournias Varotsis. Introduction to FDM 3D printing. https://www.3dhubs.com/ knowledge-base/introduction-fdm-3d-printing. Accessed: 2020-05-25.

[35] "Highly Engineered Thermoplastic Materials". In Performance Plastics. https://www.performanceplastics.com/materials/. Accessed: 2020-08-14.

[36] "Ultimate 3D Printing Materials Guide". In Simplify3D. https://www.simplify3d.com/support/materials-guide/. Accessed: 2020-08-14.

[37] Wu W, Ye W, Wu Z, Geng P, Wang Y, Zhao J. Influence of Layer Thickness, Raster Angle, Deformation Temperature and Recovery Temperature on the Shape-Memory Effect of 3D-Printed Polylactic Acid Samples. *Materials (Basel)*. 2017;10(8):970. Published 2017 Aug 19. doi:10.3390/ma10080970

[38] "Relation between ayer height and bond strength". In 3Dprinting.stackexchange. https://3dprinting.stackexchange.com/questions/6722/relation-between-layer-height-and-bond-strength. Accessed: 2020-08-15.

[39] "3D Print Warping or Curling: Easy Ways to Fix and Prevent it". In Pick 3D Printer. https://pick3dprinter.com/3d-print-warping-or-curling/. Accessed: 2020-08-13.

[40] "Layer Shifting". https://www.simplify3d.com/support/print-quality-troubleshooting/layer-shifting/. Accessed: 2020-08-16.

[41] "3D Printing Pillowing – How to Prevent Top Layer Problems.". https://all3dp.com/2/3d-printing-top-layer-problems-easy-fixes-for-pillowing/. Accessed: 2020-08-16.

[42] "The ultimate 3D Print Quality Troubleshooting Guide 2019". In Rigid.Ink. https://rigid.ink/pages/ultimate-troubleshooting-guide. Accessed: 2020-08-16.

[43] L. Yang, K. Hsu, B. Baughman, D. Godfrey, F. Medina, M. Menon e S. Wiener. *Additive Manufacturing of Metals: The Technology, Materials, Design and Production*. Springer International Publishing AG, 2017, pp. 6–24, 33–43, 120–121, 127. ISBN 978-3-319-55127-2. doi: 10.1007/978-3-319-55128-9.

[44] A.Y. Hussein.The Development of Lightweight Cellular Structures for Metal Additive Manufacturing. Phd Thesis, University of Exeter, 2013.

[45] Bremen, Sebastian, et al. "Selective Laser Melting: a Manufacturing Technology for the Future?" *Laser Technik Journal*, vol. 9, no. 2, 2 May 2012, pp. 33–38., doi:10.1002/latj.201290018.

[46] Hopmann C, Yesildag N, Bremen S, Wissenbach K, Merkt S (2015). Surface quality of profile extrusion dies manufactured by Selective Laser Melting. RTeJournal - Forum für Rapid Technologie, Vol. 2015. (urn:nbn:de:0009-2-42900).

[47] "Selective Laser Melting (SLM) – 3D Printing Simply Explained." *All3DP*, 15 Apr. 2019, all3dp.com/2/selective-laser-melting-slm-3d-printing-simply-explained/.

[48] "Small batch manufacturing of a bicycle frame using SLM. Courtesy: Renishaw and Empire Cycles". In 3D Hubs. https://www.3dhubs.com/knowledge-base/introduction-metal-3d-printing/. Accessed: 2020-10-28.

[49] Chua, Chee Kai., et al. *Standards, Quality Control, and Measurement Sciences in 3D Printing and Additive Manufacturing*. Academic Press, an Imprint of Elsevier, 2017.

[50] J. Reddy. *An introduction to the finite element method*. McGraw-Hill, New York, 3rd edition, 1993, pp. 1–2, 13–14, 104–136. ISBN 007-124473-5.

[51] "All You Need to Know about PLA for 3D Printing." *3Dnatives*, 16 Aug. 2019, www.3dnatives.com/en/pla-3d-printing-guide-190820194/.

[52] ASTM C393-00. Standard Test Method for Flexural Properties of Sandwich Constructions. Standard, ASTM International, West Conshohocken, PA, Mar. 2000.

[53] "Impresora 3D SLM SLM® 125". In DirectIndustry by virtualexpo group. https://www.directindustry.es/prod/slm-solutions/product-114591-1184397.html. Accessed: 2020-07-03.

[54] Saga, A. "Introduction on flexural testing machine". In slideshare (2014). https://pt.slideshare.net/abhisheksagar49/introduction-on-flexural-testing-machine/2. Accessed: 2020-09-22.

[55] Siemens. "siemens nx online guide". in: *Siemens website* (2020). https://docs.plm.automation.siemens.com/tdoc/nx/12/nx_help/#uid:index. Accessed: May-August 2020.

Appendix A

In this appendix, the computation of these values is furthermore explained. Figure A.1 a) presents a schematic of G parameter and b) presents the G parameter seen as a slope. All measurements presented from Figure A.2 a) to Figure A.5 a) were obtained from *Solidworks* 2018.

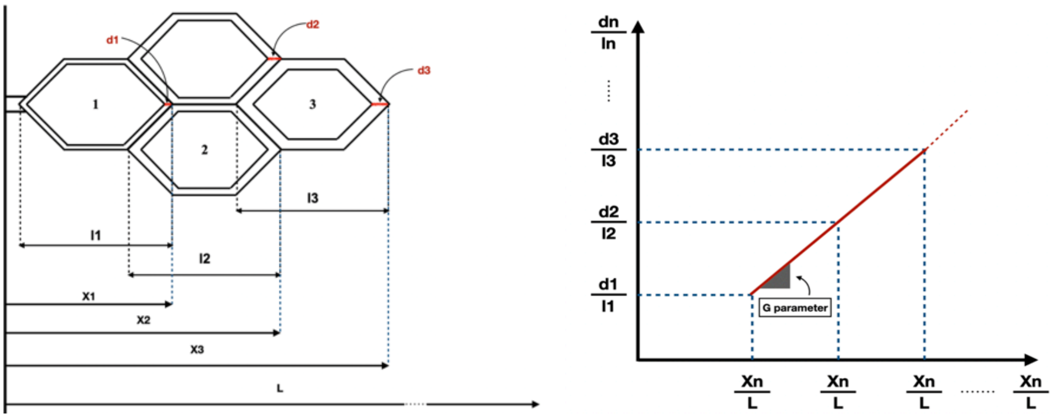

a) b)

Figure A.1 –a) Schematic of G parameter and b) G parameter seen as a slope.

Figure A.2 shows the data needed to compute the G parameter for Hexagonal d0.80-1.20 structure. The G parameter value was the same for the Lotus d0.80-1.20 and Plateau d0.80-1.20 structures.

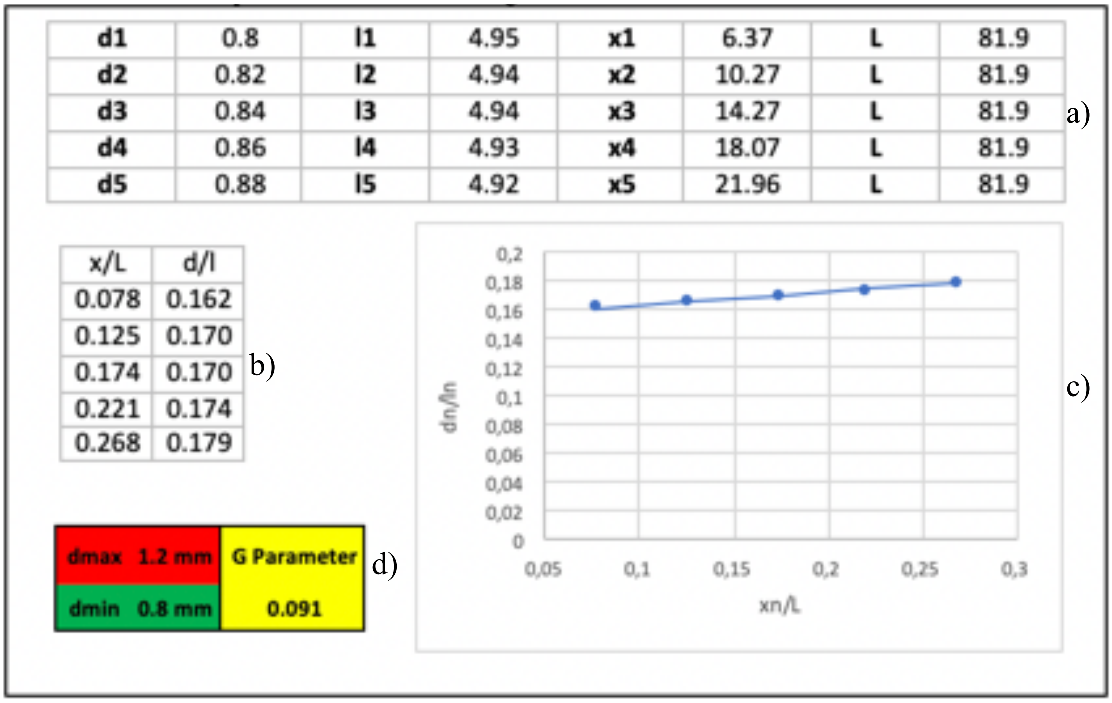

d1	0.8	**l1**	4.95	**x1**	6.37	**L**	81.9
d2	0.82	**l2**	4.94	**x2**	10.27	**L**	81.9
d3	0.84	**l3**	4.94	**x3**	14.27	**L**	81.9
d4	0.86	**l4**	4.93	**x4**	18.07	**L**	81.9
d5	0.88	**l5**	4.92	**x5**	21.96	**L**	81.9

a)

x/L	d/l
0.078	0.162
0.125	0.170
0.174	0.170
0.221	0.174
0.268	0.179

b)

c)

dmax 1.2 mm	G Parameter
dmin 0.8 mm	0.091

d)

Figure A.1 - Hexagonal d0.80-1.20 G parameter data: a) Values of the diffeent G parameter measurements, b) x/L and d/L ratios, C) G parameter slope and d) dmin, dmax and G parameter value.

Figure A.3 shows the data needed to compute the G parameter for Hexagonal d0.25-1.25 structure. The G parameter value was the same for the Lotus d0.25-1.25 and Plateau d0.25-1.25 structures.

d1	0.3	**l1**	5.1	**x1**	6.45	**L**	81.9
d2	0.35	**l2**	5.09	**x2**	10.34	**L**	81.9
d3	0.4	**l3**	5.07	**x3**	14.24	**L**	81.9
d4	0.45	**l4**	5.06	**x4**	18.13	**L**	81.9
d5	0.5	**l5**	5.04	**x5**	22.02	**L**	81.9

a)

x/L	**d/l**
0.079	0.059
0.126	0.069
0.174	0.079
0.221	0.089
0.269	0.099

b)

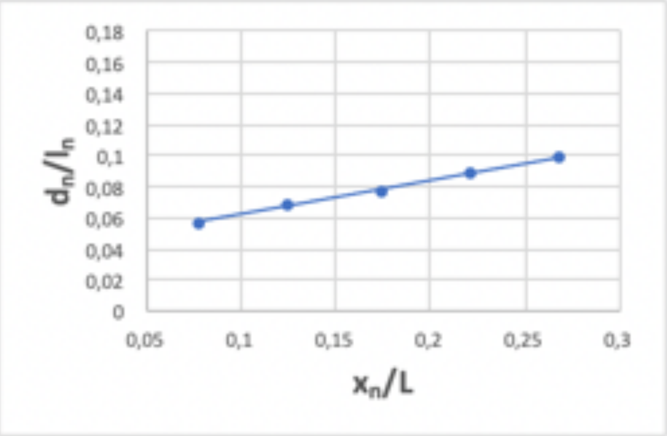

c)

dmax 1.25 mm	G Parameter
dmin 0.25 mm	0,212

d)

Figure A.3 - Hexagonal d0.25-1.25 G parameter data: a) Values of the diffeent G parameter measurements, b) x/L and d/L ratios, C) G parameter slope and d) dmin, dmax and G parameter value.

Figure A.4 shows the data needed to compute the G parameter for Hexagonal d0.25-0.75 structure. The G parameter value was the same for the Lotus d0.25-0.75 and Plateau d0.25-0.75 structures.

d1	0.28	**l1**	5.12	**x1**	6.46	**L**	81.9
d2	0.3	**l2**	5.1	**x2**	10.35	**L**	81.9
d3	0.33	**l3**	5.11	**x3**	14.25	**L**	81.9
d4	0.35	**l4**	5.09	**x4**	18.14	**L**	81.9
d5	0.38	**l5**	5.09	**x5**	22.05	**L**	81.9

a)

x/L	**d/l**
0.079	0.055
0.126	0.059
0.174	0.065
0.221	0.069
0.269	0.075

b)

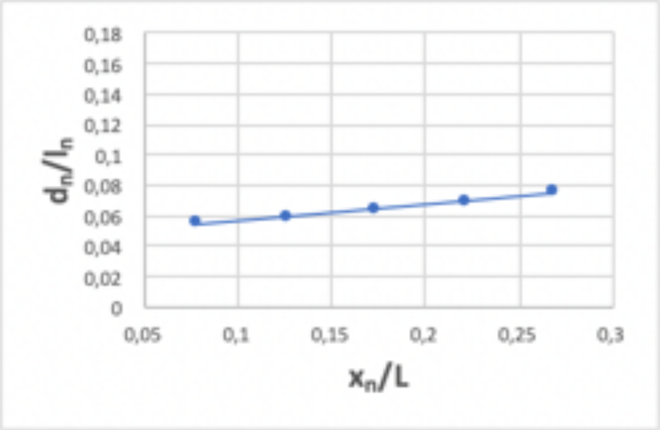

c)

dmax 0.75 mm	G Parameter
dmin 0.25 mm	0.105

d)

Figure A.4 - Hexagonal d0.25-0.75 G parameter data: a) Values of the diffeent G parameter measurements, b) x/L and d/L ratios, C) G parameter slope and d) dmin, dmax and G parameter value.

Figure A.5 shows the data needed to compute the G parameter for Hexagonal_90 d0.78-1.48 structure. The G parameter value was the same for the Lotus_90 d0.78-1.48 and Plateau_90 d0.78-1.48 structures.

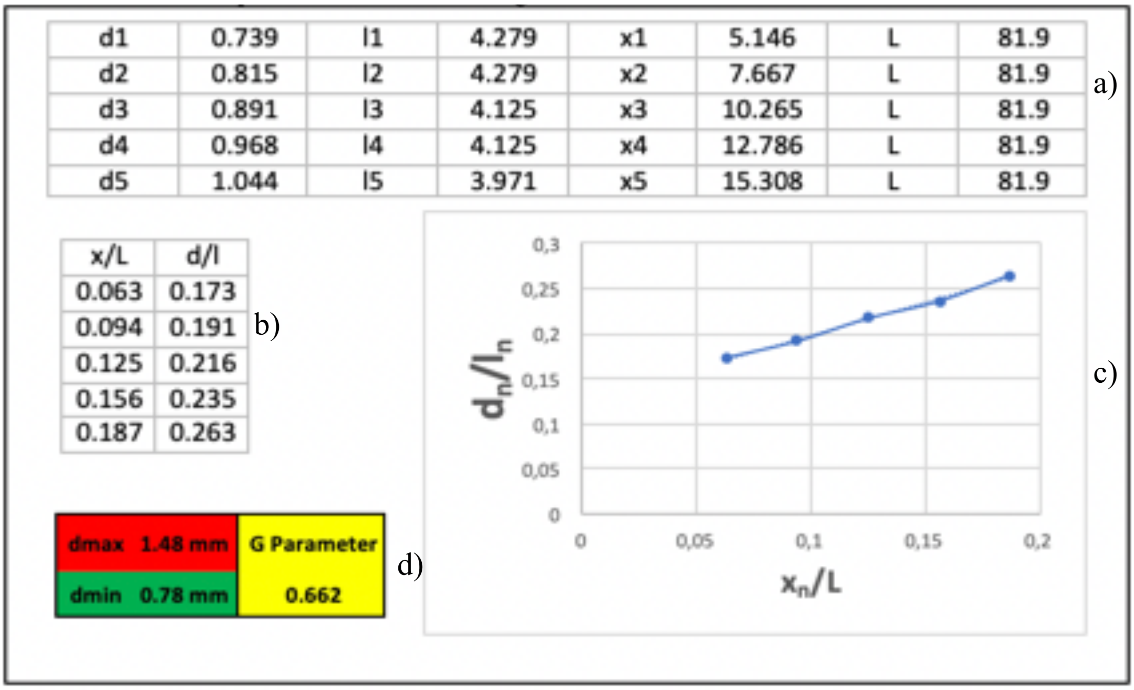

a)

d1	0.739	l1	4.279	x1	5.146	L	81.9
d2	0.815	l2	4.279	x2	7.667	L	81.9
d3	0.891	l3	4.125	x3	10.265	L	81.9
d4	0.968	l4	4.125	x4	12.786	L	81.9
d5	1.044	l5	3.971	x5	15.308	L	81.9

b)

x/L	d/l
0.063	0.173
0.094	0.191
0.125	0.216
0.156	0.235
0.187	0.263

d)

dmax 1.48 mm	G Parameter
dmin 0.78 mm	0.662

Figure A.5 – Hexagonal_90 d0.78-1.48 G parameter data: a) Values of the diffeent G parameter measurements, b) x/L and d/L ratios, C) G parameter slope and d) dmin, dmax and G parameter value.

Appendix B

In this appendix, all the other structures that were not manufactured numerical simulations are showed. Figures B.1 until B.3 present simulations for G=0.212 structures.

Figure B.1 exhibits the results for FEA of a Hexagonal structure (G = 0.212) under 3PB loading showing: displacement of the model and rollers, elemental von Mises stress in the skins and rollers reaction force in z-axis. The maximum von Mises stress was in the moving indenter contact area.

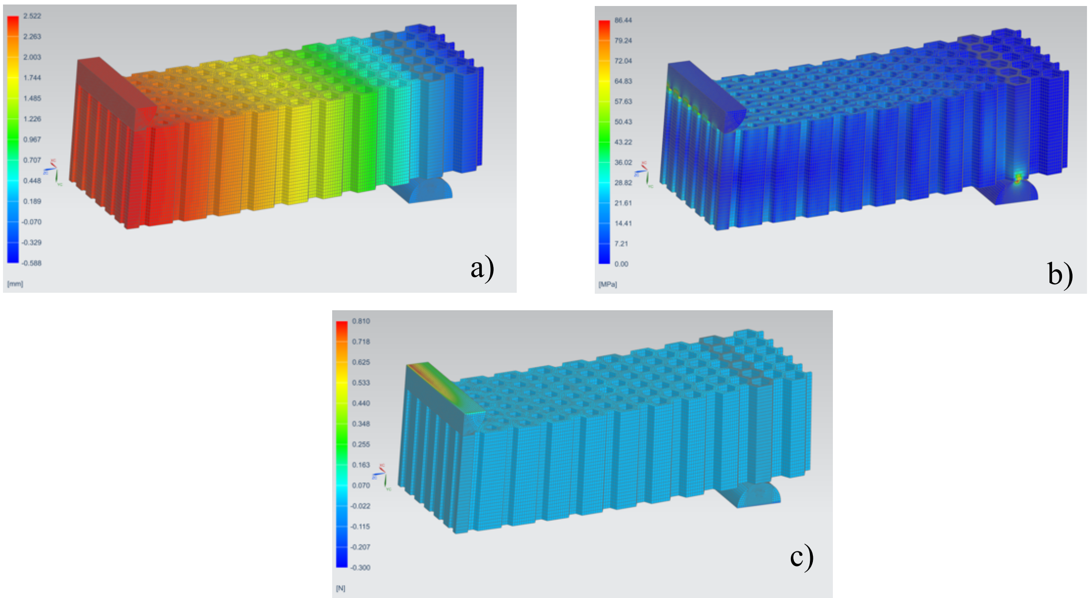

Figure B.1 - FEA of a Hexagonal structure (G=0.212) under 3PB loading, one quarter of the geometry showed: a) displacement of the model and rollers, b) elemental von Mises stress in the skins and c) rollers reaction force in z-axis.

Figure B.2 exhibits the results for FEA of a Plateau structure (G = 0.212) under 3PB loading showing: displacement of the model and rollers, elemental von Mises stress in the skins and rollers reaction force in z-axis. The maximum von Mises stress was in the moving indenter contact area.

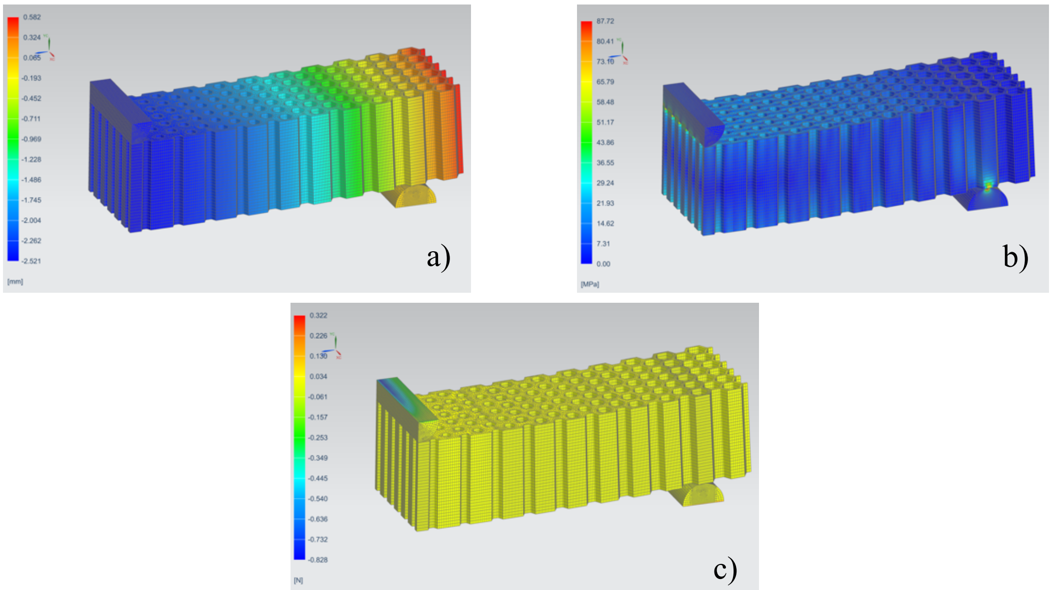

Figure B.2 - FEA of a Plateau structure (G=0.212) under 3PB loading, one quarter of the geometry showed: a) displacement of the model and rollers, b) elemental von Mises stress in the skins and c) rollers reaction force in z-axis.

Figure B.3 exhibits the results for FEA of a Lotus structure (G = 0.212) under 3PB loading showing: displacement of the model and rollers, elemental von Mises stress in the skins and rollers reaction force in z-axis. The maximum von Mises stress was in the moving indenter contact area.

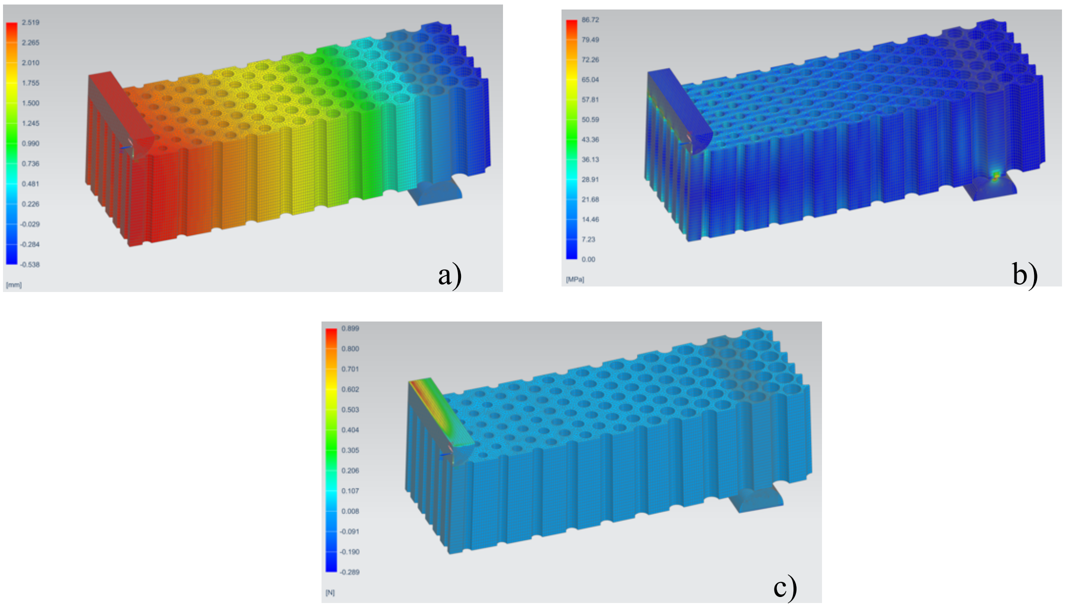

Figure B.3 - FEA of a Lotus structure (G=0.212) under 3PB loading, one quarter of the geometry showed: a) displacement of the model and rollers, b) elemental von Mises stress in the skins and c) rollers reaction force in z-axis.

Figure B.4 exhibits the results for FEA of a Upperbound d1.25 structure under 3PB loading showing: displacement of the model and rollers, elemental von Mises stress in the skins and rollers reaction force in z-axis. The maximum von Mises stress was in the moving indenter contact area.

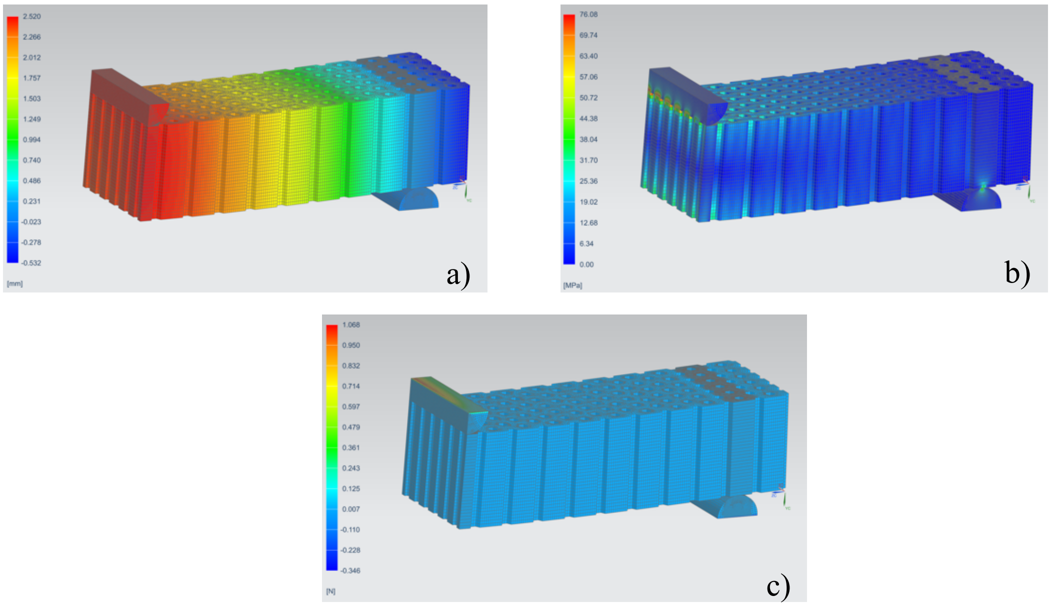

Figure B.4 - FEA of a Upperbound d1.25 structure under 3PB loading, one quarter of the geometry showed: a) displacement of the model and rollers, b) elemental von Mises stress in the skins and c) rollers reaction force in z-axis.

Figure B.5 exhibits the results for FEA of a Lowerbound d.0.25 structure under 3PB loading showing: displacement of the model and rollers, elemental von Mises stress in the skins and rollers reaction force in z-axis. The maximum von Mises stress was in the moving indenter contact area. The model had the axis inverted, and because of that, the displacement scale is negative.

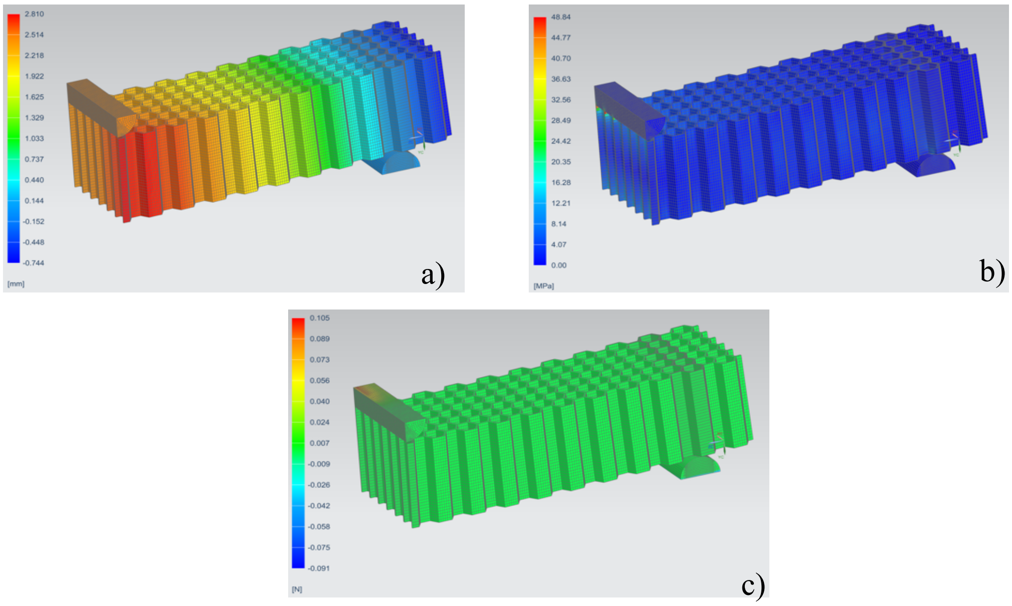

Figure B.5 - FEA of a Lowerbound d0.25 structure under 3PB loading, one quarter of the geometry showed: a) displacement of the model and rollers, b) elemental von Mises stress in the skins and c) rollers reaction force in z-axis.

Figures B.6 until B.8 present simulations for G=0.105 structures. Figure B.6 exhibits the results for FEA of a Hexagonal structure (G = 0.105) under 3PB loading showing: displacement of the model and rollers, elemental von Mises stress in the skins and rollers reaction force in z-axis. The maximum von Mises stress was in the moving indenter contact area.

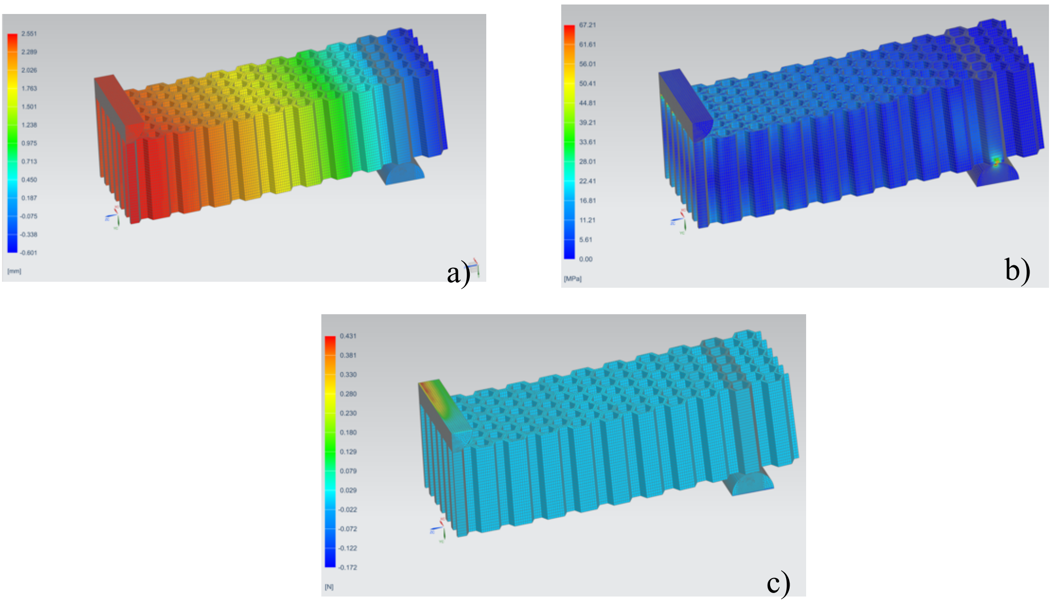

Figure B.6 - FEA of a Hexagonal structure (G=0.105) under 3PB loading, one quarter of the geometry showed: a) displacement of the model and rollers, b) elemental von Mises stress in the skins and c) rollers reaction force in z-axis.

Figure B.7 exhibits the results for FEA of a Plateau structure (G = 0.105) under 3PB loading showing: displacement of the model and rollers, elemental von Mises stress in the skins and rollers reaction force in z-axis. The maximum von Mises stress was in the moving indenter contact area.

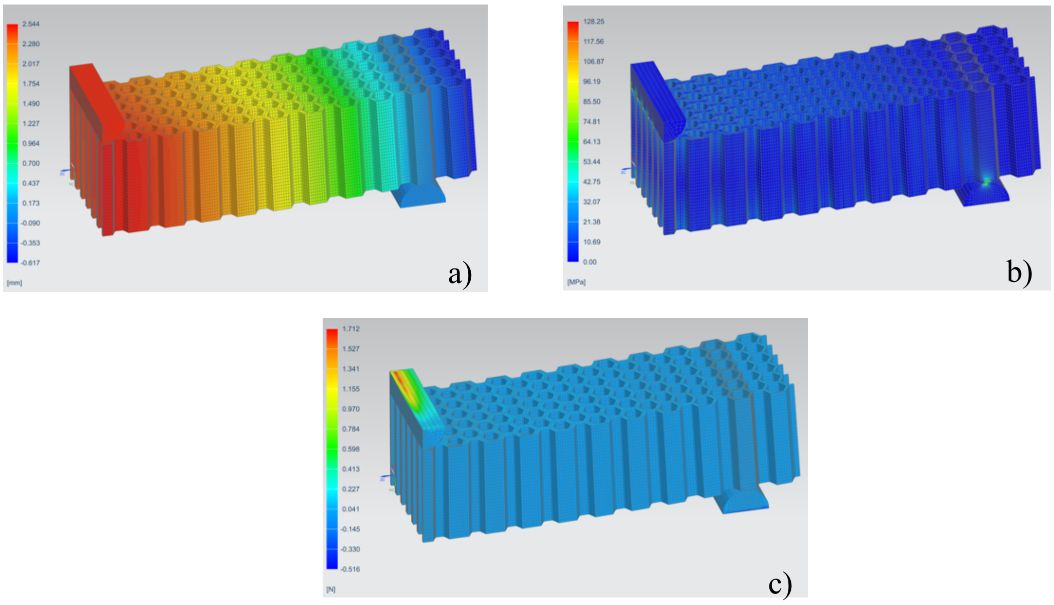

Figure B.7 - FEA of a Plateau structure (G=0.105) under 3PB loading, one quarter of the geometry showed: a) displacement of the model and rollers, b) elemental von Mises stress in the skins and c) rollers reaction force in z-axis.

Figure B.8 exhibits the results for FEA of a Lotus structure (G = 0.105) under 3PB loading showing: displacement of the model and rollers, elemental von Mises stress in the skins and rollers reaction force in z-axis. The maximum von Mises stress was in the moving indenter contact area.

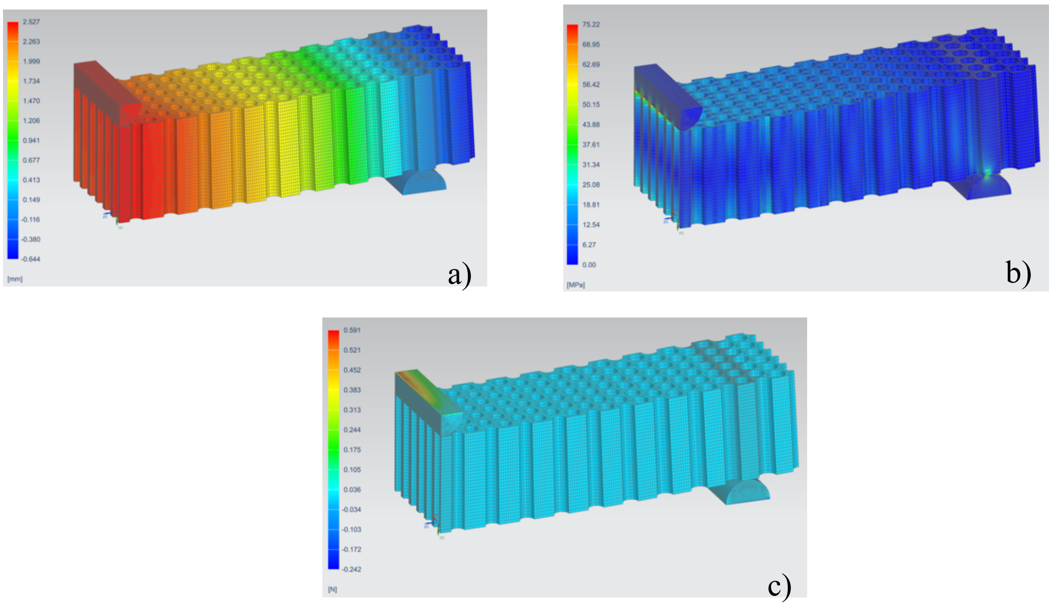

Figure B.8 - FEA of a Lotus structure (G=0.105) under 3PB loading, one quarter of the geometry showed: a) displacement of the model and rollers, b) elemental von Mises stress in the skins and c) rollers reaction force in z-axis.

Figures B.9 until B.13 presents simulations for G=0.677 structures, with 90-degree angle of rotation. Figure B.9 exhibits the results for FEA of a Hexagonal structure (G = 0.677) under 3PB loading showing: displacement of the model and rollers, elemental von Mises stress in the skins and rollers reaction force in z-axis. The maximum von Mises stress was in the moving indenter contact area.

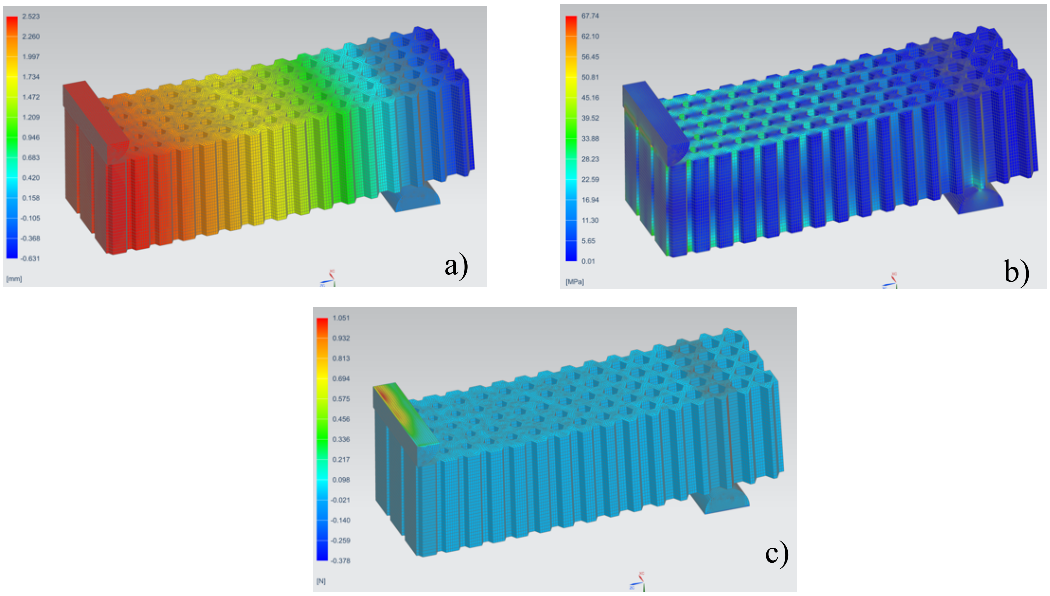

Figure B.9 - FEA of a Hexagonal structure (G=0.677) under 3PB loading, one quarter of the geometry showed: a) displacement of the model and rollers, b) elemental von Mises stress in the skins and c) rollers reaction force in z-axis.

Figure B.10 exhibits the results for FEA of a Plateau structure (G = 0.677) under 3PB loading showing: displacement of the model and rollers, elemental von Mises stress in the skins and rollers reaction force in z-axis. The maximum von Mises stress was in the moving indenter contact area.

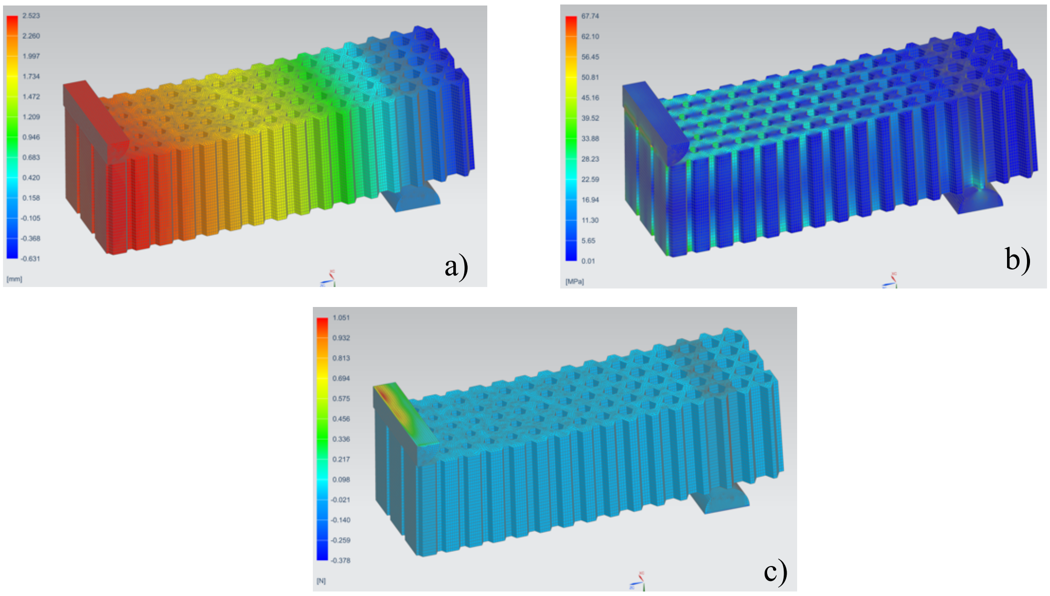

Figure B.10 - FEA of a Plateau structure (G=0.677) under 3PB loading, one quarter of the geometry showed: a) displacement of the model and rollers, b) elemental von Mises stress in the skins and c) rollers reaction force in z-axis.

Figure B.11 exhibits the results for FEA of a Lotus structure (G = 0.677) under 3PB loading showing: displacement of the model and rollers, elemental von Mises stress in the skins and rollers reaction force in z-axis. The maximum von Mises stress was in the moving indenter contact area.

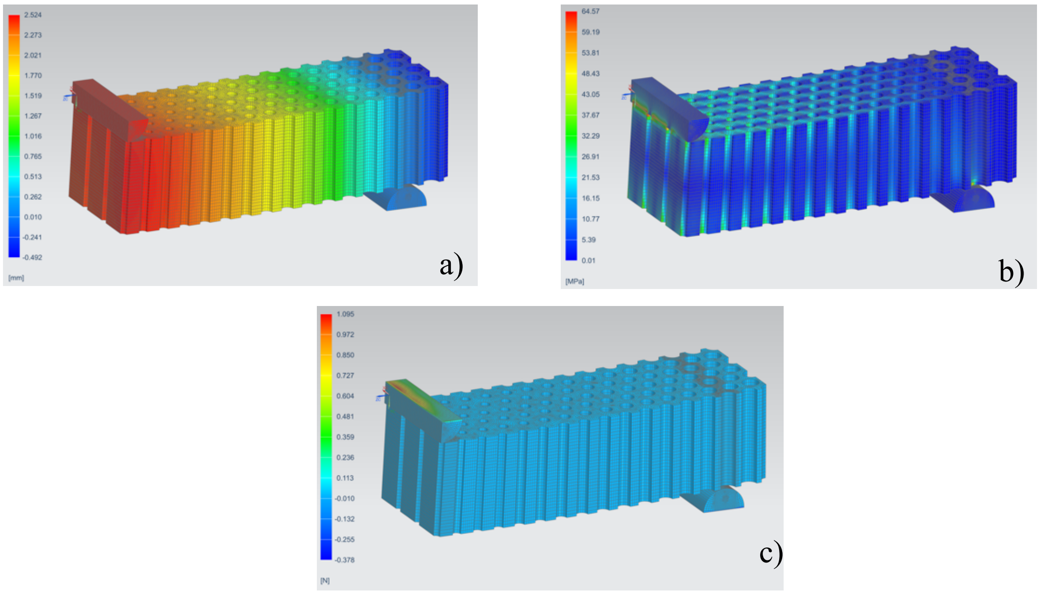

Figure B.11 - FEA of a Lotus structure (G=0.677) under 3PB loading, one quarter of the geometry showed: a) displacement of the model and rollers, b) elemental von Mises stress in the skins and c) rollers reaction force in z-axis.

Figure B.12 exhibits the results for FEA of a Upperbound d1.48 structure under 3PB loading showing: displacement of the model and rollers, elemental von Mises stress in the skins and rollers reaction force in z-axis. The maximum von Mises stress was in the moving indenter contact area.

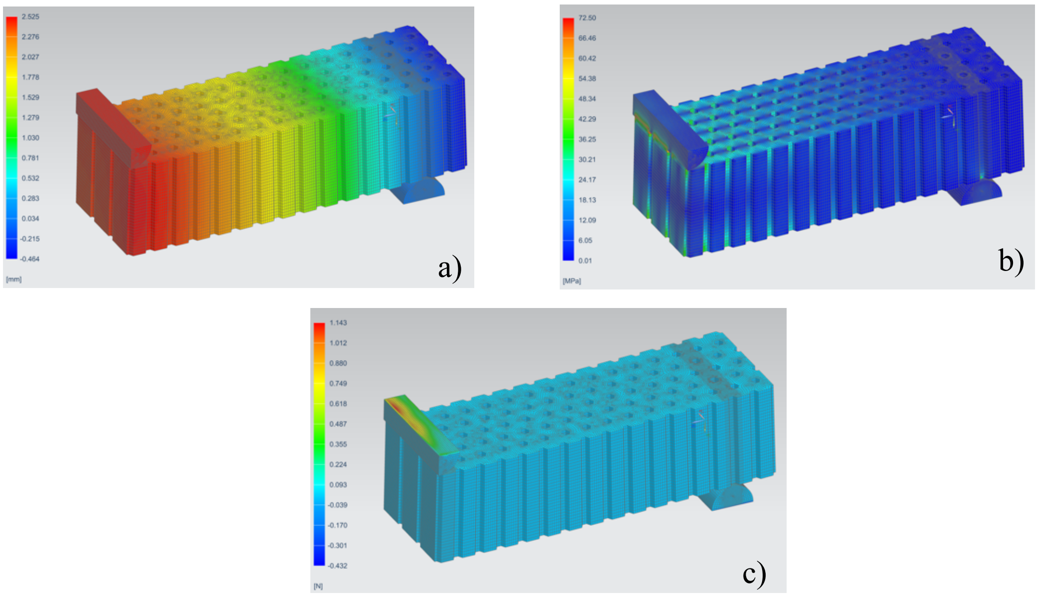

Figure B.12 - FEA of a Upperbound d1.48 structure under 3PB loading, one quarter of the geometry showed: a) displacement of the model and rollers, b) elemental von Mises stress in the skins and c) rollers reaction force in z-axis.

Figure B.13 exhibits the results for FEA of a Lowerbound d0.74 under 3PB loading showing: displacement of the model and rollers, elemental von Mises stress in the skins and rollers reaction force in z-axis. The maximum von Mises stress was in the moving indenter contact area.

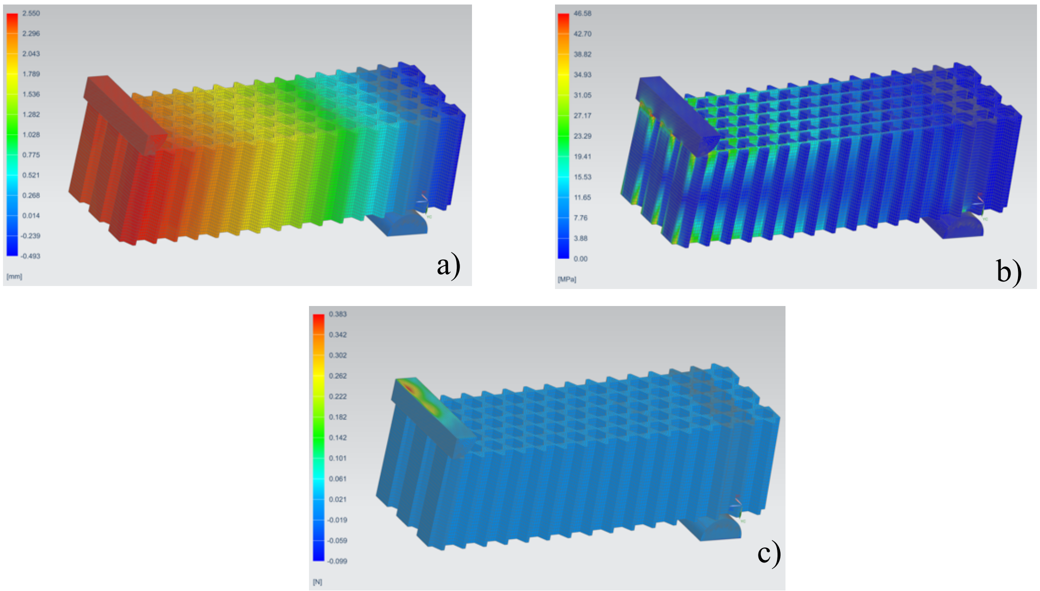

Figure B.13 - FEA of a Lowerbound d0.74 structure under 3PB loading, one quarter of the geometry showed: a) displacement of the model and rollers, b) elemental von Mises stress in the skins and c) rollers reaction force in z-axis.

Figures B.14 until B.18 presents simulations for G=0.080 Aluminum-A structures. Figure B.14 exhibits the results for FEA of a Hexagonal structure (G = 0.080) under 3PB loading showing: displacement of the model and rollers, elemental von Mises stress in the skins and rollers reaction force in z-axis. The maximum von Mises stress was in the moving indenter contact area.

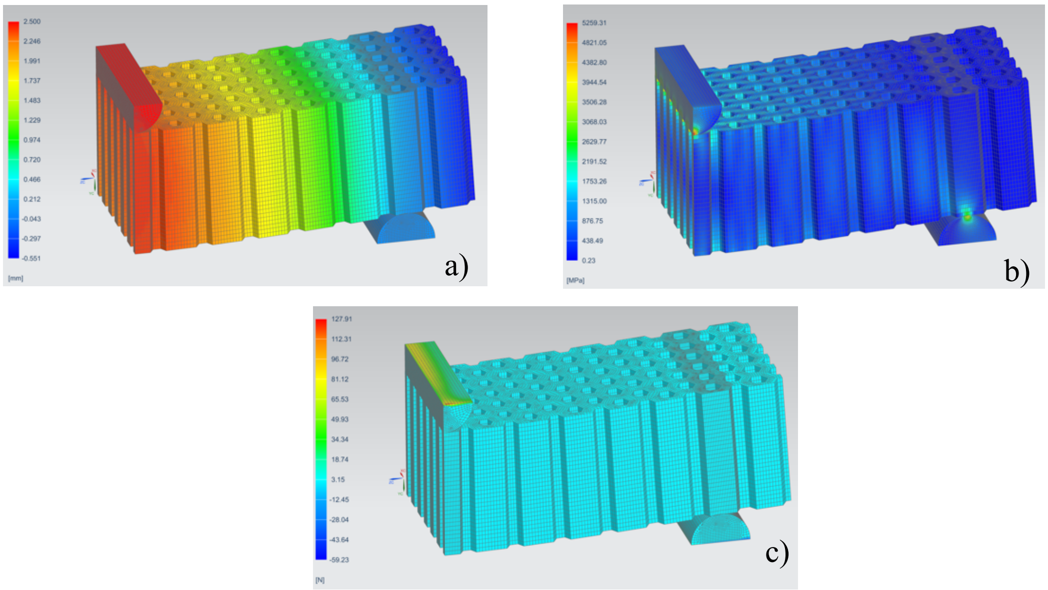

Figure B.14 - FEA of a Hexagonal structure (G=0.080) under 3PB loading, one quarter of the geometry showed: a) displacement of the model and rollers, b) elemental von Mises stress in the skins and c) rollers reaction force in z-axis.

Figure B.15 exhibits the results for FEA of a Plateau structure (G = 0.080) under 3PB loading showing: displacement of the model and rollers, elemental von Mises stress in the skins and rollers reaction force in z-axis. The maximum von Mises stress was in the moving indenter contact area.

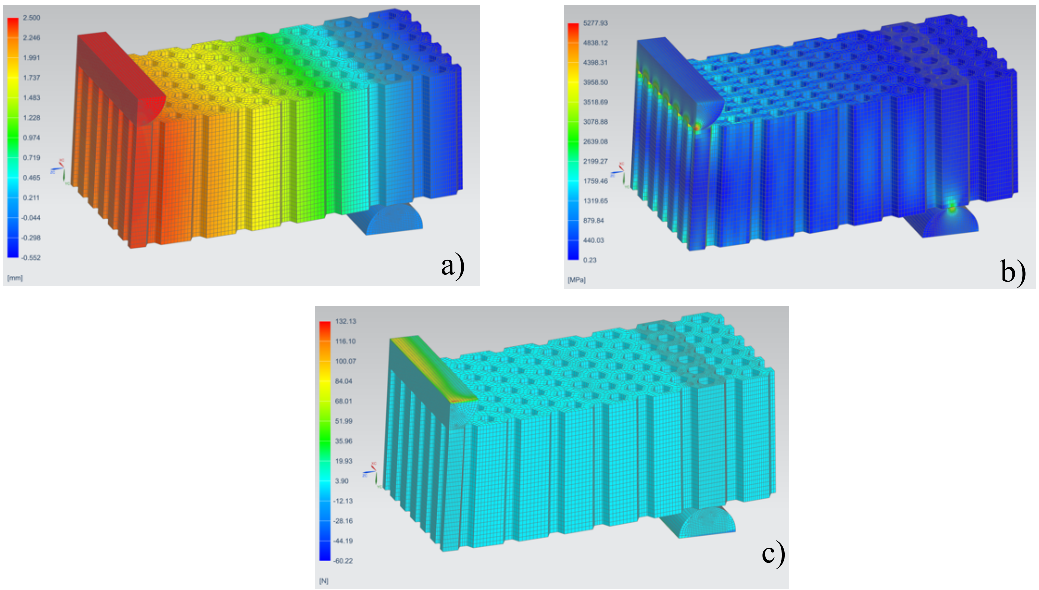

Figure B.15 - FEA of a Plateau structure (G=0.080) under 3PB loading, one quarter of the geometry showed: a) displacement of the model and rollers, b) elemental von Mises stress in the skins and c) rollers reaction force in z-axis.

Figure B.16 exhibits the results for FEA of a Lotus structure (G = 0.080) under 3PB loading showing: displacement of the model and rollers, elemental von Mises stress in the skins and rollers reaction force in z-axis. The maximum von Mises stress was in the moving indenter contact area.

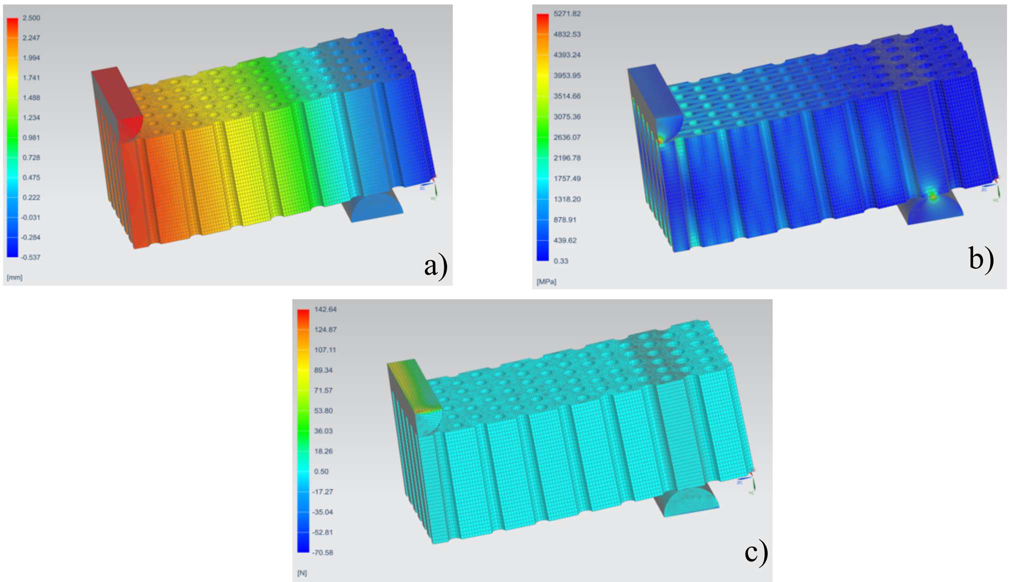

Figure B.16 - FEA of a Lotus structure (G=0.080) under 3PB loading, one quarter of the geometry showed: a) displacement of the model and rollers, b) elemental von Mises stress in the skins and c) rollers reaction force in z-axis.

Figure B.17 exhibits the results for FEA of Upperbound d1.165 structure under 3PB loading showing: displacement of the model and rollers, elemental von Mises stress in the skins and rollers reaction force in z-axis. The maximum von Mises stress was in the moving indenter contact area.

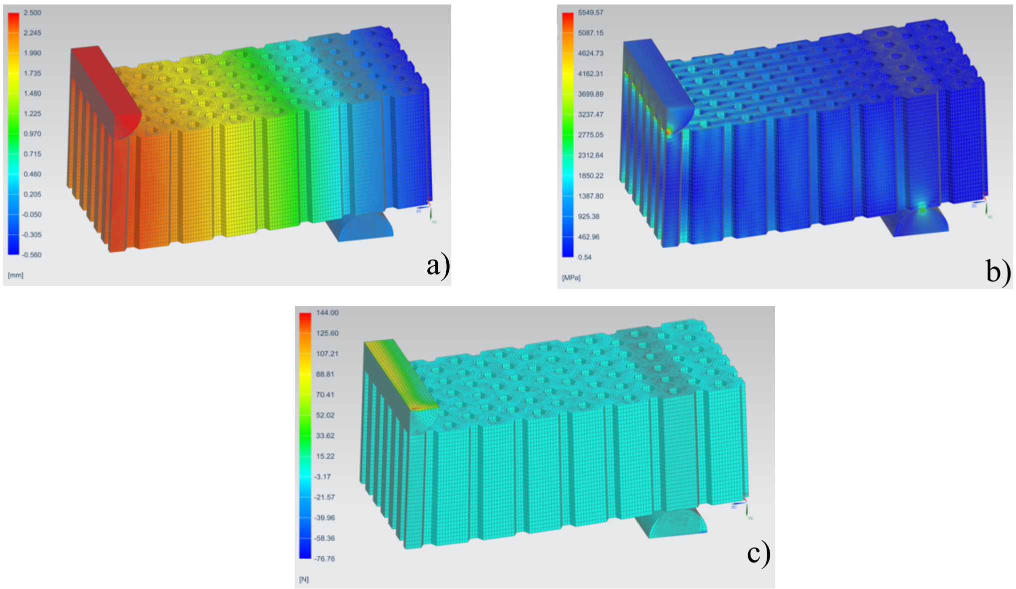

Figure B.17 - FEA of a Upperbound d1.165 structure under 3PB loading, one quarter of the geometry showed: a) displacement of the model and rollers, b) elemental von Mises stress in the skins and c) rollers reaction force in z-axis.

Figure B.18 exhibits the results for FEA of a Lowerbound d0.815 under 3PB loading showing: displacement of the model and rollers, elemental von Mises stress in the skins and rollers reaction force in z-axis. The maximum von Mises stress was in the moving indenter contact area.

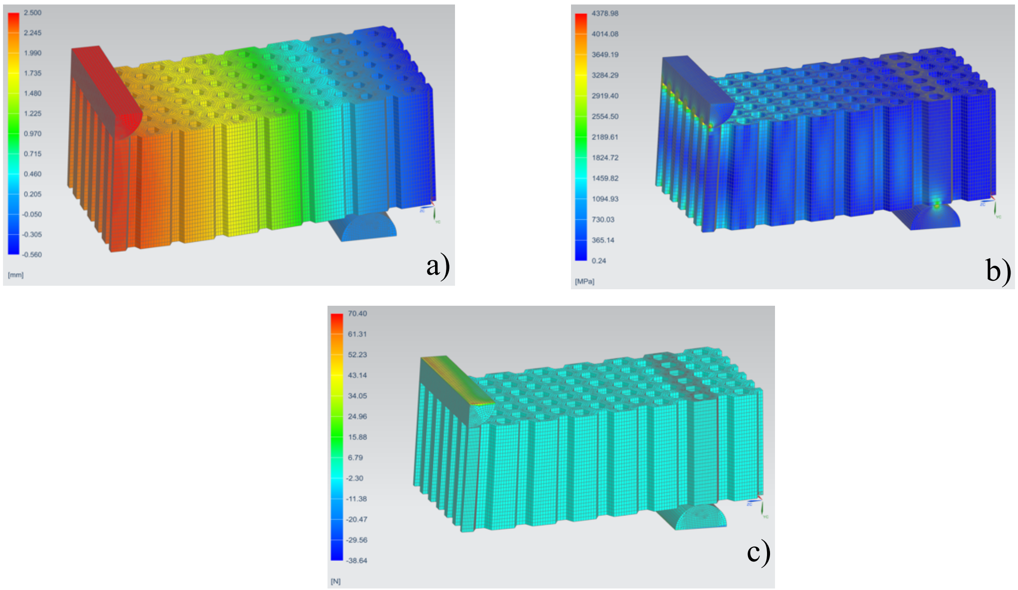

Figure B.18 - FEA of a Lowerbound d0.815 structure under 3PB loading, one quarter of the geometry showed: a) displacement of the model and rollers, b) elemental von Mises stress in the skins and c) rollers reaction force in z-axis.

Appendix C

One limitation, even nowadays, in finite element analysis is when simulating objects with a large number of nodes, which translate in a very elevate number of equations the computer has to compute, and consequently, a long computational time. To try to reduce the time required to compute the equations and the memory necessary to do so, a scale model of one of the specimens was used.

The reduction in size of the model would have another advantage, which would be a faster manufacturing process. It would allow a quicker study, since it would reduce both the computational time, as well as the manufacturing time, allowing a more agile process.

The specimen chosen for this analysis was the Lotus Aluminum specimen with a G parameter value of 0.080. To perform the reduction scaling of the specimen, the following procedures were taken. In the. part file duplicated, to be the same as the Lotus Aluminum specimen, the command scale body was used. In this preliminary analysis, the scale factor was set to 0.5 (Figure B.1 a)). This scale factor means that the final part has half the dimensions of the original one.

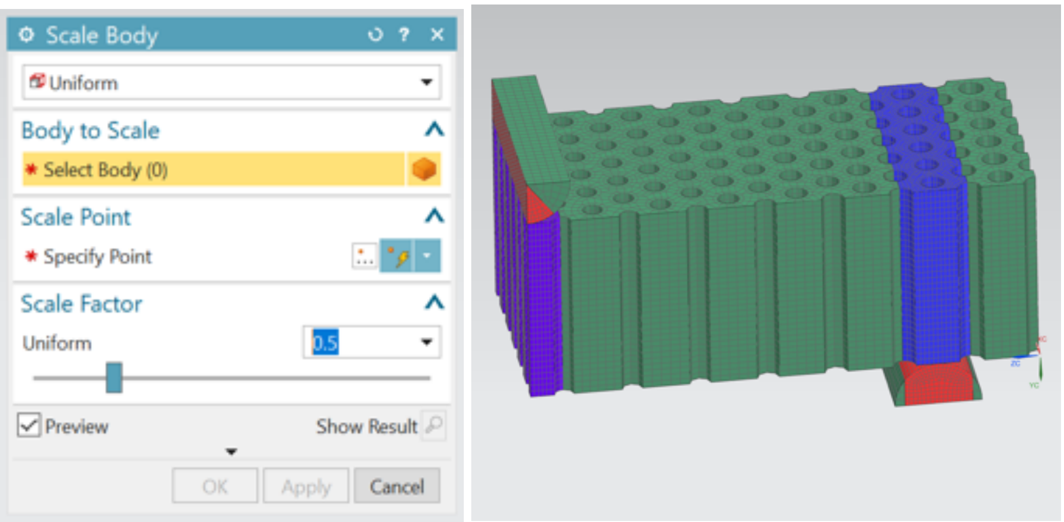

Uniform

Scale Factor: Uniform 0.5

☑ Preview

a) b)

Figure C.1 – a) Scale body command window, b) Lotus Aluminum 1:2 scale. FEM model window.

Figure B.1 b) shows the reduced part. All the parameters were kept the same as the original. The mesh was created using the 3D swept mesh command, and the materials both for the part itself and for the indenter and support were once more the same as the original. The size of the elements of the mesh was kept the same, not maintaining the same seed size. The. sim file had the same constrains once more as the original. The simulation was performed using the solver 101 linear static. The results are presented in the Table C.1.

Table C.1 – Reaction force, contact force, von Mises stress and strain energy for different scale Lotus Aluminum specimens.

Structure	Displacement (mm)	Reaction Force (N)	Contact Force (N)	von Mises Stress (MPa)	Strain Energy (N.mm)
Lotus Aluminum 1:1	2.5	55332	-55411	4283.51	27932
Lotus Aluminum 1:2	2.5	30095.3	-30136,3	5943.29	26003.8
Lotus Aluminum 1:2	1.25	14340.9	-14347.5	3998.42	6193.72

The table presents the values obtained for displacement of 2.5 mm and for displacement of 1.25 mm, i.e. half the maximum displacement. The correlation between the different values is presented next. The comparison was performed by dividing the values.

Table C.2 box presents the ratios between the Lotus Aluminum 1:1 and the Lotus Aluminum 1:2 for 2.5 mm displacement.

Table C.2 - Ratios between the Lotus Aluminum 1:1 and the Lotus Aluminum 1:2 for 2.5 mm displacement.

Reaction Force Ratio	Contact Force Ratio	Von Mises Stress Ratio	Strain Energy Ratio
$\frac{55332}{30095.3} = 1.8385$	$\frac{55411{,}7}{30136.3} = 1.8387$	$\frac{4283{,}51}{5943.29} = 0.7207$	$\frac{27932}{26003.8} = 1.0741$

Table C.3 presents the ratios between the Lotus Aluminum 1:1 and the Lotus Aluminum 1:2 for 1.25 mm displacement.

Table C.3 - Ratios between the Lotus Aluminum 1:1 and the Lotus Aluminum 1:2 for 1.25 mm displacement.

Reaction Force Ratio	Contact Force Ratio	Von Mises Stress Ratio	Strain Energy Ratio
$\frac{55332}{14340.9} = 3.8583$	$\frac{55411{,}7}{14347.5} = 3.8621$	$\frac{4283{,}51}{3998.42} = 1.0713$	$\frac{27932}{6193.72} = 4.5097$

There is no visible correlation between the values. The ratios vary a lot between the different parameters, not being evident scaling correlation between them.

The simulation time and the memory used was reduced as showed in the Table C.4.

Table C.4 – Simulation time, memory used and printing times comparison between scales.

Structure	Simulation Time (h)	Memory used (gb)	Printing time (h)
Lotus Aluminum 1:1	2.2	3.72	21.25
Lotus Aluminum 1:2	0.14	1.21	4.5

The plot presented in Figure C.2 shows the Load vs. Displacement until 2.5 mm showing the initial stiffness for both specimens.

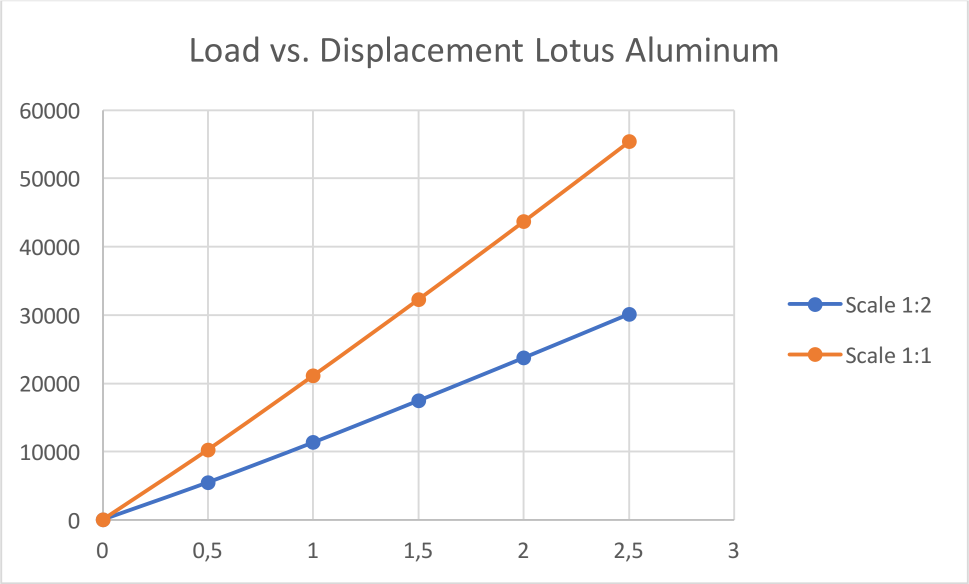

Figure C.2 - Plots comparing both scale 1:1 and 1:2 Load vs Displacement.